Reconstruction of 3D models of the femur from planar x-rays for surgical planning

by
Jodri Oosthuizen

Thesis presented in partial fulfilment of the requirements for the degree of Master of Engineering (Mechatronic) in the Faculty of Engineering at Stellenbosch University

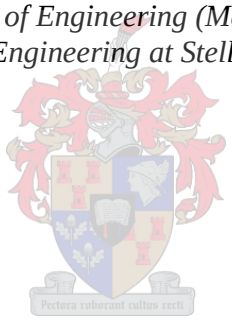

Supervisor: Dr Johan van der Merwe

March 2023

Declaration

By submitting this thesis electronically, I declare that the entirety of the work contained therein is my own, original work, that I am the sole author thereof (save to the extent explicitly otherwise stated), that reproduction and publication thereof by Stellenbosch University will not infringe any third party rights and that I have not previously in its entirety or in part submitted it for obtaining any qualification.

Date: .....March 2023.....

Abstract

Slipped Capital Femoral Epiphysis (SCFE) is a common hip disorder of adolescents in which the femoral head is posteroinferiorly displaced from the neck of the femur. Several treatments have been described in the literature to treat the deformity, where an intertrochanteric osteotomy is usually performed to correct the slip of more severe cases. Pre-operative planning is a critical requirement for the success of any orthopaedic procedure. Traditionally the planning relies on 2D radiographs and although this method has proven to be sufficient for a subset of procedures, factors such as overlapping anatomical structures, lack of 3D information and variability of film quality could lead to inaccuracies of the preoperative estimations. Thus, to improve the accuracy and reliability in the treatment of SCFE, 3D models of bony structures have been used more extensively for pre-operative surgical planning. CT scans are the preferred 3D image modality but still have some limitations. These limitations include subjecting the patient to a high radiation dose, being expensive and time-consuming. 3D Reconstruction of a patient-specific model from 2D images has been considered to be a suitable alternative. Therefore this study aimed to develop a 2D/3D reconstruction algorithm that reconstructs a 3D patient-specific model of the proximal femur from a 2D x-ray image. The algorithm compensates for the lack of information provided by the x-ray images by using prior knowledge of the shape. The prior knowledge can be obtained through the use of a Statistical Shape Model (SSM) which aims to capture all possible variations within a population. Thus, as a part of the study, an SSM was constructed using a training dataset containing 27 proximal femurs. The constructed shape model along with a digitally reconstructed x-ray was used to reconstruct a 3D model from 2D images. The resulting patient-specific model was obtained by projecting the contour of the SSM to the corresponding x-ray and measuring the point-to-point distance between the projected contour and the contour extracted from the x-ray. The accuracy of the resulting model was determined by comparing the reconstructed model to a ground truth model segmented from image data. The models were generated with an average reconstruction error of 2.13 mm, a Hausdorff distance of 5.49 mm and a Dice coefficient of 0.88. An average difference of 3.05° was measured between the NSAs of the ground truth and reconstructed meshes. The average NSA difference indicated that the reconstruction algorithm could be adapted to include SCFE data. Although the results corresponded well with those of similar studies available in the literature, the accuracy of the model needs to be improved before being applied to clinical applications.

Uittreksel

Geglyde Proksimale Femorale Epifises (GPFE) is a algemene heupversteuring van adolessente waar die femorale kop in ‘n postero-inferior wyse van die femorale nek verplaas word. Verskeie metodes word in literatuur beskryf vir die behandeling van die versteuring, waar ‘n intertrokanteriese osteotomie gewoontlik gebruik word om die gly van die femorale kop in meer ernstige gevalle te herstel. Vir enige ortopediese prosedure om ‘n sukses te wees, is die chirurgiese beplanning voor die prosedure ‘n noodsaaklike vereiste. Beplanning deur middel van 2D radiografieë word gesien as die konvensionele metode vir chirurgiese beplanning. Alhoewel hierdie metode bewys is as voldoende vir ‘n versameling van prosedures, kan faktore soos anatomiese strukture wat oorvleuel, tekort aan 3D informasie en die wisselvalligheid van filmkwaliteit die akuraatheid van preoperatiewe benaderings beïnvloed. Dus, om die betroubaarheid en akkuraatheid in die behandeling van GPFE te verbeter word drie dimensionele been struktuur modelle meer gereeld gebruik vir die beplanning voor die prosedure. CT skandering is die 3D beeld modaliteit wat verkies word, maar dit het steeds beperkings. Die beperkings sluit ‘n hoë bestraling dosis, hoë kostes en tydrowendheid in. 3D rekonstruksie van ‘n patiënt-spesifieke model vanaf ‘n 2D beeld word as ‘n gepaste alternatief oorweeg. Daarom was die onwikkeling van ‘n 2D/3D rekonstruksie algoritme wat ‘n patient-spesifieke model van die proksimale femur vanaf ‘n 2D beeld rekonstrueer, ‘n mikpunt van die studie. So ‘n algoritme kompenseer vir die gebrek aan inligting wat deur die x-straal verskaf word deur vorige kennis van die vorm te gebruik. Die vorige kennis kan vekry word met die gebruik van ‘n Statistiese Vormmodel (SV) wat die moontlike variasies in ‘n populasie vas vang. Dus was daar, as deel van die studie, ‘n SV geskep vanuit ‘n opleidingsdatastel wat 27 proksimale femurs bevat. Die SV wat geskep is saam met ‘n digitale gerekonstrueerde x-straal was gebruik om ‘n 3D model van ‘n 2D beeld te rekonstrueer. Die resulterende patiënt-spesifieke model was verkry deur die kontoer van die SV te projekteer na die ooreenstemmende x-straal en die punt-tot-punt afstand tussen die geprojekteerde kontoer en die kontoer wat uit die x-straal onttrek is te meet. Die akkuraatheid van die resulterende model was bepaal deur die gerekonstrueerde model met die ware data, wat vanuit die CT data gesegmenteer is, te vergelyk. Die modelle was gegenereer met ‘n gemiddelde rekonstruksie fout van 2.13 mm, ‘n Hausdorff afstand van 5.49 mm en ‘n Dice se koëffisiënt van 0.88. ‘n Gemiddelde verskil van 3.05° was tussen die nek-skag hoek van die rekonstrueerde en die ware model gemeet. Hierdie verskil dui aan dat die algoritme angepas kan word om data van GPFE pasiente in te sluit. Alhoewel die resultate in die studie verkry ooreenstem met data wat in literatuur beskikbaar is, moet die akkuraatheid van die model verbeter word voordat dit oorweeg kan word vir kliniese toepassings.

Acknowledgements

First and foremost, I want to express my sincere gratitude to Dr. J van der Merwe for providing me with such an interesting topic and for the invaluable advice, continuous guidance, and patience during the project's duration. It has been gratefully appreciated.

To my parents, Daneël and Loamie, thank you for all the love and support over the years. Thank you for all the sacrifices you have made to provide me with every opportunity available. Without you, none of this would have been possible.

To my sister, Mercia, who has always been my biggest cheerleader in everything I do, thank you for all your support and encouragement through the years.

And finally, Jac-Villiers, thank you so much for all your understanding and unconditional love and support. You have been my rock and stood by me through all the ups and downs. Thank you very much for everything.

Dedications

To our Heavenly Father, with who all things are possible.

Table of contents

Page

List of figures

Page

List of tables

Page

Nomenclature

Abbreviations

2D	Two Dimensional
3D	Three Dimensional
AP	Antero Posterior
ARE	Average Reconstruction Error
BMI	Body Mass Index
COP	Center of Projection
CT	Computed Tomography
DC	Dice Coefficient
DLT	Direct Linear Transform
DP	Descriptive Parameters
DRR	Digitally Reconstructed Radiograph
GP	Gaussian Process
GPMM	Gaussian Process Morphable Model
IRB	Institutional Review Board
LAC	Linear Attenuation Coefficient
MCMC	Markov Chain Monte Carlo
MH	Metropolis-Hastings
MPPM	Morpho-realistic Personalized Parametric Model
MRI	Magnetic Resonance Imaging
NIH	National Institute of Health
NRRD	Newly Raw Raster Data
NSA	Neck-shaft Angle
NSCP	Non-Stereo-Corresponding Point
PA	Procrustes Analysis
PCA	Principal Component Analysis
PDM	Point Distribution Model
RMSE	Root Mean Squared Error
SCFE	Slipped Capital Femoral Epiphysis

SCP	Stereo-Corresponding Point
SSM	Statistical Shape Model
SPPM	Simplified Personalized Parametric Model
STL	Stereolithography

Symbols

A	Mesh A
a	Point a
a_t	Acceptance threshold
B	Mesh B
b	Point b
b_i	Contribution of variance
$C(M)$	Compactness
C_s	Synthesized contour
C_t	Target Contour
c_i	Mixture coefficient
D	Observed data
d	Radiological path
d_{out}	Output dimension
d_x	Equal distances between slices in the x-direction
d_y	Equal distances between slices in the y-direction
d_z	Equal distances between slices in the z-direction
E	Energy spectrum of x-ray
$G(M)$	Generality
G_σ	Gaussian kernel for noise removal
G_M	Magnitude of gradient
G_x	Gradient in x-direction
G_y	Gradient in y-direction
$\mathcal{GP}$	Gaussian Process
H	Hausdorff distance
h_a	Hounsfield unit

I	X-ray signal intensity
I_0	Initial intensity
I_{3x3}	Identity matrix
k	Kernel
k_b	Augmented kernel
k_{GP}	Covariance matrix
k_g	Gaussian kernel
k_{sum}	Multiscale kernel
k_{PDM}	Kernel sampled from the model
L	Path from the x-ray source to the detector plane
ℓ	Likelihood
l	intersection length
M	Number of modes
$\mathcal{N}$	Normal distribution
N	Number of points
N_{lms}	Number of landmarks
N_x	Number of planes in the x-direction
N_y	Number of planes in the y-direction
N_z	Number of planes in the z-direction
n_s	Number of specificity iterations
n_g	Number of shapes in the training dataset
p_{12}	Parametrical representation of ray between two points
p	point
$P(\theta)$	Prior distribution
$P(D)$	Normalizing factor
$P(\theta\|D)$	Posterior distribution
$P(D\|\theta)$	Data likelihood
Q	Proposal
$\mathbb{R}$	Set of real numbers
R_i	Randomly sampled shape
r	Position of ray

r_p	Rotation parameters
s	Normal distribution of shape variations
$\boldsymbol{s}$	Shape instance
s_v	Scale of variance
S_i	Shape estimated by model
$S(M)$	Specificity
t_p	Translation parameters
t_{Ri}	The training shape that best resembles the sampled shape
t_{Ei}	Excluded shape
u	Deformation vectors
$\tilde{u}$	Low-rank gaussian process
$\boldsymbol{u}$	Set of deformation vectors
V	Volume
X_p	X-plane
x	Point x
Y_p	Y-plane
y	Point y
Z_p	Z-plane

Greek Symbols

α	Parametric value
α_i	Random coefficient
α_p	Model coefficients
α_{min}	Parametric value of ray entry point
α_{max}	Parametric value of ray exit point
γ	Variance ratio
Γ	Shape representation of discrete points
θ	Set of parameters
θ'	New sample set of parameters
θ_g	Slope of image gradient
θ_v	Proposed valgus correction angle

θ_f	Proposed flexion correction angle
λ	Eigenvalue
μ	Mean shape
μ_{GP}	Mean shape of a gaussian process
μ_{LAC}	Linear attenuation coefficient
μ_{LACa}	Linear attenuation coefficient of current voxel
μ_{LACw}	Linear attenuation coefficient of water
ρ	Voxel intensity value
σ	Bandwidth parameter
σ_{Ct}	Noise model
$\sigma_{G(M)}$	Generality error
$\sigma_{S(M)}$	Specificity error
σ_{sg}	Sample standard deviation of generality
σ_{ss}	Sample standard deviation of specificity
Σ	Covariance matrix
ϕ	Eigenvector

Subscripts

a	Current voxel
avg	Average
b	Ray beam
g	Gaussian
i	Sample
max	maximum
min	minimum
n	Number of iterating samples
Ref	Reference
s	Mode of shape model

Chapter 1

Introduction

1.1 Background

Slipped Capital Femoral Epiphysis (SCFE) is a common hip disorder affecting adolescents between the ages of nine and sixteen (Loder and Skopelja, 2011). The condition is defined by the posteroinferior displacement of the femoral head, also known as the epiphysis, from the neck of the femur at the level of the growth plate (Gholve *et al.,* 2009). Loder *et al.* (2000) stated that the prevalence of SCFE is not fully determined as it varies depending on the population being studied. The prevalence of SCFE in the South African population is unknown, but Nortje (2009) estimated the prevalence to be approximately 2.3 to 4.1 per 100,000 based on the number of patients treated between 1999 and 2004.

Various suggestions have been made regarding the aetiology of SCFE, but none have been proven in all instances, thus the cause has been assumed to be multifactorial and most likely a result of biochemical and biomechanical factors (Weiner, 1996). A diagnosis of SCFE is made based on the information obtained during a physical examination and confirmed through radiographic imaging. The severity of the slip is determined through the acquired radiographs which are used to determine the treatment needed to manage the condition (Aronsson *et al.*, 2006).

The aim of treating SCFE is to avoid additional displacement of the epiphysis while avoiding possible complications such as avascular necrosis and chondrolysis (Loder *et al.*, 2000). A variety of treatments have been described in the literature to treat the disorder. The most common approach used to increase the range of motion and contain the femoral head and acetabulum is the intertrochanteric osteotomy (Richolt *et al.*, 1998). Irrespective of the treatment used, the correction could be difficult due to the 3D deformity present (Cherkasskiy *et al.*, 2017).

1.2 Motivation

According to Hak and Rose (2010), for any orthopaedic surgery to be a success, pre-operative surgical planning is essential. The pre-operative planning of an intertrochanteric osteotomy is traditionally performed on the anteroposterior and frog-lateral radiographs. Although the conventional way of pre-operative planning based on 2D radiographs has proven to be adequate for a large number of procedures, the approach does have certain drawbacks. These drawbacks include

poor reproducibility of positioning for radiographs, being time-consuming and cumbersome, and being subject to low film quality that affects the accuracy of the provided information (Atesok *et al.*, 2015). Since the x-ray images provide 2D projections of 3D anatomical structures, the accuracy of the pre-operative estimations relies on the experience and knowledge of the surgeon planning and performing the surgery (Drapikowski *et al.*, 2008). Thus, in order to increase the precision and reliability of the diagnosis and treatment of SCFE, 3D patient-specific models of bony structures are being used extensively for pre-operative planning (Hosseinian and Arefi, 2015).

CT scanning is the conventional medical imaging technique for obtaining 3D data as it generates an accurate and detailed set of cross-sectional images (Hosseinian and Arefi, 2015). These images can then be used to provide 3D models for pre-operative surgical planning. Various methods in literature have applied these 3D images in pre-operative planning using CT images rather than x-rays or by segmenting the region of interest from the data and using it as a 3D printed model or in computer-aided reconstruction (Cherkasskiy *et al.*, 2017; Drapikowski *et al.*, 2008; Kamegaya *et al.*, 2005). Although these methods presented improved results, there are certain restrictions with the CT imaging modalities for SCFE. These limitations include exposing patients to a high radiation dose, where patients diagnosed with SCFE are typically younger individuals who, according to Brenner (2010), are more sensitive to radiation. Furthermore, in a resource-limited setting, the cost of CT scans can become prohibitive (Hesper et al., 2017). Therefore, further research has been done to introduce alternative methods which still provide detailed and accurate 3D information but reduce the limitations associated with a CT scan.

Currently, a reliable alternative is considered to be the reconstruction of a patient's 3D anatomy from a set of 2D images. This technique includes prior information about the shape to compensate for the shortage of information on the 2D radiograph (Dakhakhni, 2013). Several techniques used for reconstructing a 3D model from 2D data have been described in the literature. These methods include those based on points, contours, statistical models, and parametric models (Hosseinian and Arefi, 2015).

According to Sarkalkan *et al*. (2014), statistical shape modelling is a commonly used technique in the orthopaedic field. A shape model aims to capture all possible variations within a population and can thus be used as the prior knowledge during the reconstruction algorithm. This method has been applied to various studies throughout the literature. Fleute *et al.* (1999) proposed a method where a 3D model of the distal femur is constructed by deforming the shape model to match the 2D contours segmented from x-ray images. Benameur *et al.* (2003) used a shape model-based method to reconstruct vertebrae whereas other researchers

such as Zheng *et al.* (2009) proposed using the reconstruction method to reconstruct the proximal femur.

There are currently no studies, to the author's knowledge, that use 2D/3D reconstruction for pre-operative surgical planning for the correction osteotomy of SCFE. Based on the promising results of shape-model-based 2D/3D reconstruction shown in the available literature, similar methods will be used to reconstruct a proximal femur from an x-ray image to eventually be used in pre-operative surgical planning.

1.3 Objectives

This study aims to develop a method that reconstructs a 3D patient-specific model from a 2D x-ray image. The goal of the model is to provide the level of accuracy usually obtained through 3D imaging without the limitations associated with it. To fulfil the aim of the study, the study objectives are defined as:

1. Construct a Statistical Shape Model (SSM) of the study population's proximal femur based on a CT dataset.

2. Develop a 2D/3D reconstruction algorithm that reconstructs a 3D patient-specific model of the proximal femur from a 2D x-ray image.

3. Validate the statistical shape model and resulting patient-specific 3D model.

1.4 Scope

Since the traditional imaging modality used for SCFE diagnosis is 2D radiographs, CT scans of these patients were not available. However, to construct a statistical shape model, a dataset of CT scans is required. Unfortunately, we were unable to compile an SCFE dataset due to the limited number of cases available retrospectivey. Therefore, the scope of this study was limited to using a publicly available dataset, containing CT images of healthy femurs from an adult USA-based population as a proxy. If the findings of this study are encouraging, it may serve as motivation for future prospective studies to collect CT scans of adolescent patients diagnosed with SCFE from a specific population.

1.5 Overview

Chapter 2 provides a detailed literature review regarding the femur, SCFE and pre-operative planning techniques used for an SCFE corrective surgery, whereas Chapter 3 describes how the variations within the study population have been

captured by an SSM and how the model has been validated. Then the methods used to generate a digitally reconstructed radiograph (DRR) and to reconstruct a 3D patient-specific model from the 2D DRR are described in Chapter 4 and Chapter 5, respectively. Lastly, the final remarks are discussed in Chapter 6.

Chapter 2

Literature review

This chapter offers a comprehensive summary of the literature reviewed to provide a better understanding of the study objectives stated in Section 1.3. The chapter starts with a description of the femur's anatomy followed by the literature regarding Slipped Capital Femoral Epiphysis. Thereafter information regarding the traditional methods of pre-operative surgical planning is provided and lastly, the current methods for 2D/3D reconstruction of patient-specific models, along with their limitations, are discussed.

2.1 Anatomy of the femur

According to Moore *et al.* (2013), the femur, also known as the thigh bone, is the longest, heaviest, and strongest bone in the human body as it accounts for approximately one-quarter of a person's total height. When standing, the upper body weight rests on the two femoral heads, therefore the main functions of the femur are weight bearing and gait stability. The robust shape of the femur provides many origin or attachment points for ligaments or muscles which contribute to walking and other movements (Moore *et al.*, 2013). The femur consists of three main parts namely a shaft, a proximal end, and a distal end. Figure 2.1 illustrates these three regions along with the anatomy of the femur.

The proximal end of the femur consists of a head, neck, and two trochanters, the lesser and greater trochanter. The femoral head, forming about two-thirds of a sphere, articulates with the acetabulum of the pelvis to form the hip joint (Snell, 2011). The femoral head is held within the acetabulum by the capsular ligament, consisting of thick, strong, distinct bands that are wrapped around the proximal femur and the acetabulum periosteum (Wagner *et al.* 2012). The femoral head is covered with articular cartilage, which is a thin layer of cartilage that serves as a shock absorber and reduces friction, except for a small depression called the fovea capitis (Snell, 2011). The fovea acts as a site of attachment for the ligament of the femoral head and although providing the hip joint with little support, it does convey the obturator artery which supplies the femoral head with blood (Betts *et al.* 2013).

The region below the femoral head is identified as the neck of the femur. The neck has the shape of a trapezium with the narrow apex attached to the spherical head and the wider base being continuous with the femur shaft (Betts *et al.*, 2013). The long axis of the head and neck creates an angle of approximately 125° with the long axis of the shaft (Snell, 2011). According to Fetto *et al.* (2002), this angle of

the neck shaft is greater than 160° at birth and gradually decreases until a steady angle is reached. This angle allows for an increased range of motion of the femur at the hip joint as it places the femoral head and neck at a more perpendicular angle to the acetabulum (Moore *et al.*, 2013).

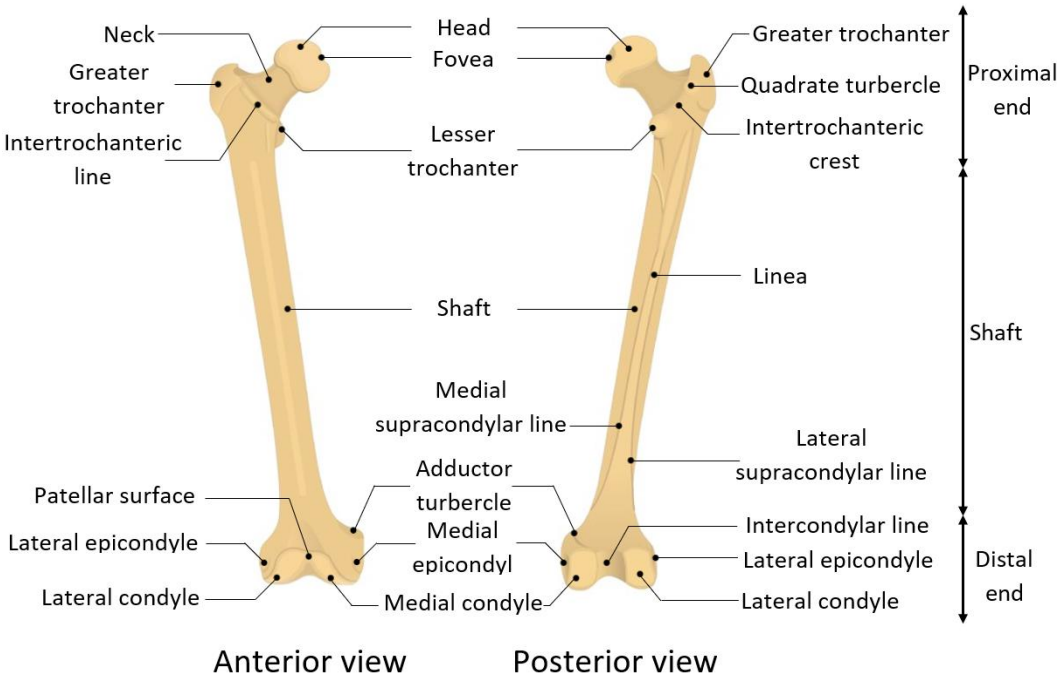

Figure 2.1: Anatomy of the femur from the anterior and posterior view

Located at the junction of the neck and the shaft are two prominent bony protrusions called trochanters. The greater trochanter, also known as the major trochanter, is identified as the large, laterally placed bone mass projecting superiorly and posteriorly at the point where the neck meets the shaft (Moore *et al.*, 2013). The greater trochanter acts as an attachment site for multiple muscles acting across the hip joint. The lesser trochanter is a smaller, abrupt bony protrusion, which projects medially from the posteromedial part of the femur, just below the neck (Betts *et al.*, 2013). A powerful muscle called the iliopsoas, which can create forceful contractions attaches to the lesser trochanter.

A roughened ridge of bone which spans between the lesser and greater trochanter and runs in the inferomedial direction on the anterior side of the femur is called the intertrochanteric line (Snell, 2011). This line acts as a site of attachment for the iliofemoral ligament which is the strongest ligament of the hip. As the intertrochanteric line runs past the lesser trochanter on the posterior side it is referred to as the pectineal line (Moore *et al.*, 2013). On the posterior side of the femur, the two trochanters are connected by a similar but smoother bony ridge called the intertrochanteric crest. The rounded elevation present on the crest is

called the quadrate tubercle and is the attachment site for the quadratus femoris (Moore *et al.*, 2013).

On the anterior surface of the elongated femoral shaft, the femur is smooth and rounded, but on the posterior side, the femur has a ridge, called the linea aspera (Snell, 2011). Various hip and thigh muscles use the linea aspera to make long, thin attachments to the femur. Moore *et al.* (2013) stated that the linea aspera has lateral and medial margins which continue below the lateral and medial supracondylar ridge. Superiorly, the lateral margin becomes continuous with the rough gluteal tuberosity which extends inferiorly from the greater trochanter, whereas the medial margin becomes the pectineal line. The shaft is anteriorly slightly convexed and becomes broader towards the distal end of the shaft where it forms a triangular area on the posterior surface called the popliteal surface (Moore *et al.*, 2013).

The distal end of the femur consists of the medial and lateral femoral condyle which is posteriorly separated by the intercondylar notch. Anteriorly the condyles merge to form a longitudinal depression called the patellar surface (Moore *et al.*, 2013). The condyles are the smooth, rounded areas of the distal femur where the inferior and posterior surfaces articulate with the tibia and menisci of the knee to form the knee joint. Above the condyles, bony evaluations referred to as the medial and lateral epicondyles are located where the medial and lateral collateral ligaments originate from (Betts *et al.*, 2013).

2.2 Anatomical landmarks of the proximal femur

Depending on the location and function of bones, surface features vary considerably (Betts *et al.*, 2013). The prominent surface features can then be used as landmarks. The anatomical landmarks used throughout this study are listed in Table 1 and indicated in Figure 2.2. Since the landmarks provided in the table are descriptive of the surrounding region, the most prominent feature in the area was chosen as the landmark.

2.3 Slipped capital femoral epiphysis

SCFE is a disorder affecting the hip of adolescents. The disorder is characterized by the posteroinferior slippage of the capital femoral epiphysis, also known as the femoral head, from the neck of the femur through the growth plate (Loder *et al.* 2000). The term SCFE is a misnomer since the epiphysis remains in the acetabulum while it is actually the femoral neck metaphysis that moves anterosuperior as indicated in Figure 2.3 (Aronsson *et al.* 2006). In the majority of the patients, the femoral head is located in a more varus position in relation to the neck, meaning the head displaces downward and inward on the femoral neck. Occasionally the head moves superiorly, putting the slip into a valgus position and creating valgus

Table 1: Description of anatomical landmarks used throughout this study

Landmark	Description
Fovea	Minor indentation on the medial side of the femoral head
Lesser Trochanter	An abrupt, conical eminence just below the neck, shaft junction
Top point of the greater trochanter	The proximal point of the greater trochanter when viewed from the anterior/posterior view
Trochanteric fossa	Depression at the base of the internal surface on the proximal femur
Lateral point of the greater trochanter	The most lateral point located on the greater trochanter when viewed from the anterior/posterior view

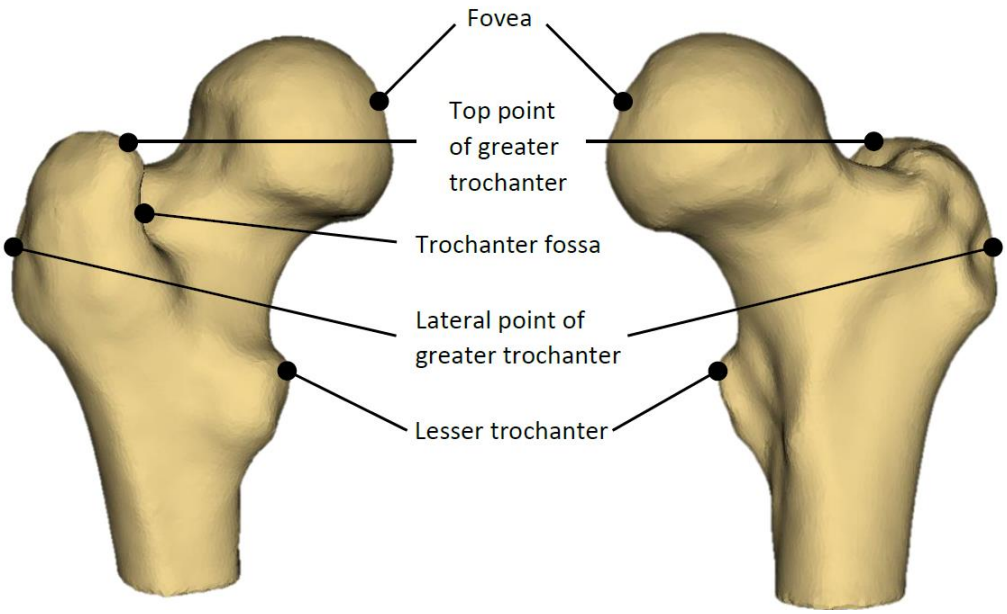

Figure 2.2: Landmarks of the proximal femur

SCFE (Aronsson *et al.*, 2006). The aetiology is unknown for a vast majority of the cases as it can be caused by a variety of factors, but when left untreated the disorder can lead to pain and restriction to movement in the short term or hip joint arthritis in the long term (Peck *et al.* 2017). The different aspects of SCFE are described in the following sections.

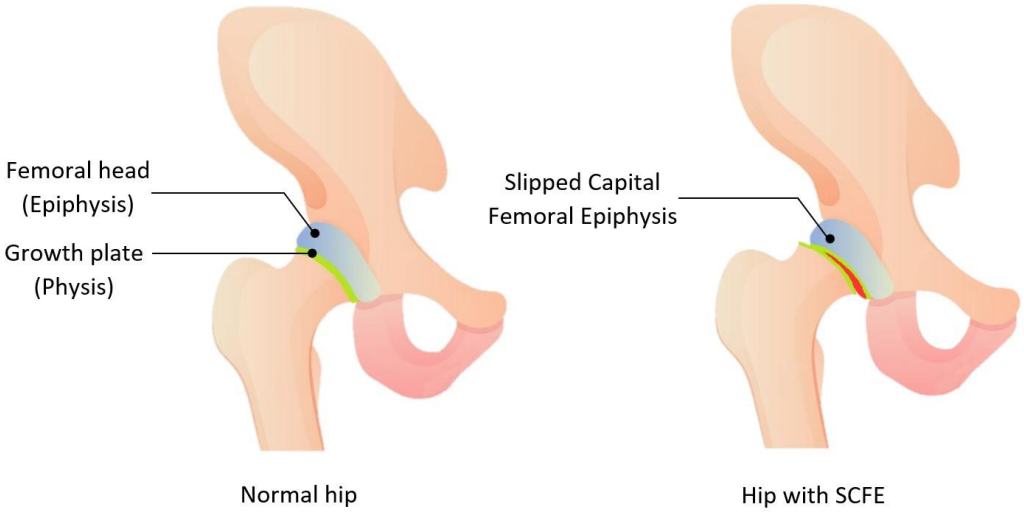

Figure 2.3: Illustration of a normal hip (left) versus an SCFE-affected hip (right).

2.3.1 Epidemiology

SCFE is the most common hip disorder diagnosed in adolescents (Peck *et al*., 2017; Gholve *et al*., 2009). According to Loder *et al.* (2000), the prevalence of SCFE is not completely known as it depends on the population being examined. It has been reported that the prevalence can range from 0.2 per 100,000 in eastern Japan to as high as 10.08 per 100,000 in the northeastern United States (Aronsson *et al.*, 2006). The prevalence of SCFE in South Africa is not known, but Nortje (2009) estimated the prevalence to be 2.3 – 4.1 per 100,000 based on the number of patients treated from 1999 to 2004. Although there is no conclusive explanation for the differential in the SCFE prevalence, Aronsson *et al*. (2006) and Lehmann *et al*. (2006) speculate that it may be due to differences in genetic background, and cultural traditions and behaviours.

SCFE typically occurs between the ages of nine and sixteen with the mean age of onset being 12 years in girls and 13.5 years in boys (Loder and Skopelja, 2011). The SCFE cases that occur outside of the common age range are assumed to be atypical due to endocrine or systemic abnormalities or disorders (Lehmann *et al.* 2006). According to Loder *et al.* (2000), approximately 60% of the patients diagnosed with SCFE were boys. This assumption is based on a general population. This conclusion was reached during a worldwide seasonal variation study in which a dataset that included patients from various populations was used (Loder, 1996).

The bilateral prevalence reports vary considerably and depend on many factors such as the study, type of treatment and method of radiographic measurement (Aronsson *et al.*, 2006). The prevalence of bilateral involvement has been reported as approximately 63% of patients (Jerre *et al.*, 1996). Of these patients presenting with bilateral SCFE, 50% – 60% of patients initially present with bilateral

involvement. Those who first present with unilateral involvement which later developed into bilateral SCFE, develop a second slip within the first 18 months of the first slip (Loder *et al.*, 2000).

2.3.2 Aetiology

The cause of SCFE is mostly idiopathic. Many suggestions have been made regarding the aetiology of SCFE, but none have been present in all cases. It has been assumed that the aetiology is most likely multifactorial and is the result of biomechanical and biochemical factors. The combination of these factors could lead to a weakened physis and ultimately cause a slip (Weiner, 1996). A slip occurs when the femoral head slips off the neck of the proximal femur at the growth plate and stays within the acetabulum while the femoral neck moves upwards and outwards (Kandzierski *et al*. 2012). Some of the mechanical factors associated with SCFE are an increased Body Mass Index (BMI), the increased slope of the physis and increased femoral retroversion (Gholve *et al.* 2009).

An increased BMI is a factor strongly associated with SCFE and is also associated with an increased femoral retroversion, which is a condition in which the neck of the femur is rotated backwards relative to the shaft. Adolescents with normal body weight have an average anteversion of approximately 10.6° whereas adolescents with increased body weight have an anteversion of approximately 0.4° (Loder *et al.*, 2000). Since the forces transmitted to the physis are proportional to a person's body weight, an increased BMI and an increased retroversion lead to increased shear stress across the physis (Balasubramanian 2019). Patients presenting with SCFE have an increased slope, 11°, of the femoral physis compared to a normal slope of 8°. The increased slope along with the mechanical forces resulting from the body weight and femoral retroversion is enough to cause a slip of the physis (Aronsson *et al.* 2006).

SCFE occurs during puberty which leads to many hormonal changes. Therefore it is likely that biochemical factors are associated with SCFE. Although most SCFE patients do not have an apparent endocrine disorder, a subtle, but not yet diagnosable endocrinopathy may be present (Aronsson *et al.*, 2006). The surge in hormonal changes and the increased prevalence of SCFE in patients who receive growth hormone supplements for hypothyroidism or hypogonadism suggest the association between SCFE and endocrine dysfunction (Weiner, 1996). During puberty, the physeal strength decreases and although a clear cause has not been identified, Loder *et al.* (2000) suggest that it might be due to provisional calcification and the increase of cartilage width of hypertrophy zones. The male predominance in the prevalence of SCFE can be explained by the effects of gonadotropins on the physis. Testosterone reduces physeal strength, whereas estrogen increases physeal strength and decreases physeal width (Gholve *et al.*, 2009).

Any combination of the factors mentioned above could lead to an abnormal increase in shear stress enforced on the physis and thus resulting in a slip.

2.3.3 Classification

Many methods to classify SCFE have been used over the years. Traditionally the classification of SCFE is based on the duration of the presented symptoms. According to Balasubramanian *et al.* (2019), this method classifies SCFE into four categories namely:

1. Pre-slip SCFE: These patients might present with a slight limp or complain about groin or knee pain on exertion or weakness in the affected leg, but has no evident displacement of the physis on examination.

2. Acute SCFE: When there is an abrupt displacement of the physis and presents with a deformity of external rotation and limited motion secondary to pain on physical examination. The duration of these symptoms and signs are less than three weeks.

3. Chronic SCFE: The most common type, accounting for approximately 85% of all cases. These patients present with pain in the thigh, groin and knee and a physical examination would demonstrate discrepancy in the limb length and loss of internal rotation, flexion and abduction of the hip. The SCFE is classified as chronic when these symptoms gradually developed over a longer period, more than 3 weeks.

4. Acute-on-chronic SCFE: When a patient with initial chronic SCFE symptoms, subsequently develops acute symptoms as well as a sudden increase in the degree of the slip.

The problem however with this traditional method of classification is that it depends on the memory of the patient, which can be inaccurate. The method also does not provide a prognosis regarding the potential for avascular necrosis (Loder *et al.*, 2000). Therefore, more recently clinical classification is based on the physeal stability and can be classified with a clinical and/or radiographic method.

The preferred clinical classification, proposed by Loder *et al.* (1993), is based on the patient's ability to bear weight on the affected leg. This method classifies the SCFE as being stable or unstable. The SCFE is considered stable when the patient is able to walk, with or without support whereas the SCFE is unstable when the patient can not walk on the affected leg, with or without support (Gholve *et al.*, 2009).

Two radiographic methods are used for the classification of SCFE (Kallio *et al.,* 1995; Sinha *et al*., 2021). These methods are the Wilson classification system,

which measures the percentage of the slip and the classification described by Southwick (1967) which measures the epiphyseal shaft angle. The method described by Southwick's classification is a more accurate representation of the true magnitude of the slip and is thus used more in practice (Gholve *et al.*, 2009). Southwick (1967) classifies the slip as mild (<30°), moderate (30° - 60°) or severe (>60°). Southwick's classification is illustrated in Figure 2.4

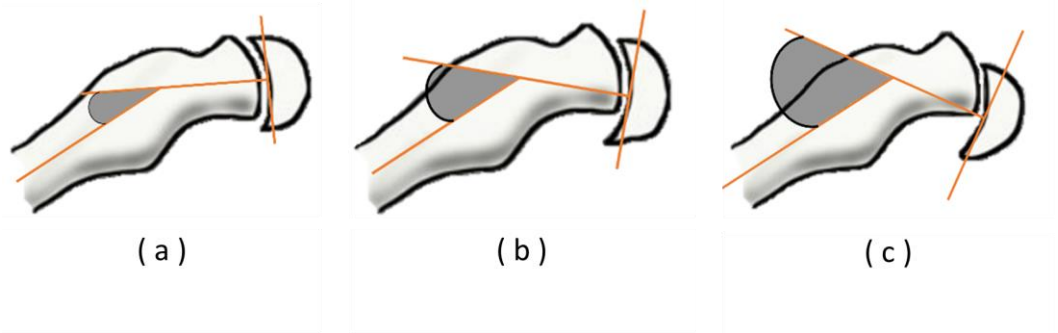

Figure 2.4: Severity of the slip. (a) Mild slip with an epiphysis displacement of <30° (b) Moderate displacement of 30 - 60° (c) Displacement is severe when > 60° (Illustration adapted with permission from Lasanianos and Giannoudis (2014))

2.3.4 Diagnosis

The presentation of SCFE may vary as it depends on the severity and the stability of the slip. However, the most common symptoms presented with SCFE are limping and pain in the hip, thigh, groin or knee (Peck *et al.*, 2017). Due to the pain being poorly localized, it could lead to a delay in diagnosis or even a missed diagnosis. History of trauma to the area is rarely presented. A severe slip would present with more dramatic symptoms such as sudden severe pain and/or inability to bear weight (Balasubramanian *et al.*, 2019).

During a physical examination, the gait of the patient is observed and the range of motion of the affected hip is examined. When a patient has SCFE, they might present with a slight limp, abnormal gait or might not be able to bear weight with a severe slip. Lying on their back, the patient's affected leg could appear shorter and externally rotated and obligatory external rotation of the affected leg would be visible when the hip is passively flexed to 90° (Gholve *et al.*, 2009). The patient may also present with limited internal rotation of the hip, which is usually the most telling sign of SCFE (Peck *et al.*, 2017). When the patient does not have bilateral SCFE, the affected hip's range of motion is compared to the uninvolved hip.

To confirm a diagnosis, imaging of the patient is ordered to visualise the position of the femoral head relative to the neck of the femur. For the diagnosis of SCFE, plain radiographs are usually sufficient. Since approximately 63% of the patients may have bilateral SCFE, both hips should be visualized on the x-ray (Gholve *et al.*,

2009). Antero-posterior (AP) and frog-leg lateral radiographs are the standard x-rays taken, although the frog-leg lateral is not recommended in patients with an unstable slip as it may further displace the slip (Balasubramanian *et al.*, 2019).

The radiographs are obtained to display the posteroinferior slip of the femoral epiphysis relative to the metaphysis. In early slip SCFE, the slip is often only seen on the frog-leg lateral view as the slip is usually posterior (Aronsson *et al.*, 2006). In stable SCFE, radiographic signs of anterior and superior remodelling of the femoral neck are seen with periosteal new bone formation developing at the junction between the neck and head which creates a retroversion deformity of the femoral neck (Loder *et al.*, 2000).

Other signs that aid in the diagnosis of SCFE is Klein's line and Steel's blanch sign. Klein's line is a technique where a line is drawn along the superior aspect of the femoral neck in the AP radiograph. Normally the line would intersect the femoral head but in patients with SCFE, the line passes over the head (Balasubramanian *et al.*, 2019). Steel's metaphyseal blanch sign is a crescent-shaped double density observed on the AP radiograph which is caused by the posteriorly displaced femoral head overlapping the medial femoral neck (Aronsson *et al.*, 2006).

The severity of SCFE can be assessed on the AP and frog-leg radiographs, but more typically it is evaluated on the lateral view as proposed by Southwick (1967). This method determines the degree of the slip by measuring the epiphyseal-shaft angle of both legs and subtracting the uninvolved shaft angle from the SCFE shaft angle (Aronsson *et al.*, 2006). If the patient has bilateral SCFE, 12° can be used as the control value.

2.4 Treatment

Once SCFE has been diagnosed, the top priority in treating patients with SCFE is to prevent further progression of the slip while avoiding complications (Loder *et al.*, 2000). Since the severity of the slip relates directly to the duration of the symptoms, early treatment is suggested (Aronsson *et al.*, 2006). Many treatment methods for SCFE are available, each with its advantages and disadvantages Aronsson *et al.* (2006) and Loder *et al.* (2000) described some of the treatment methods available in the literature and are listed below.

2.4.1 Hip-spica cast

Hip-spica cast is a cast that immobilizes the hip and aims to improve the displacement of the metaphysis. Immobilization in a bilateral cast avoids the complications related to operational procedures (Loder *et al.*, 2000). Betz *et al.* (1990) treated 32 patients, 37 hips, with acute or chronic SCFE. The patients were treated with traction for symptom relief and immobilized using a hip-spica cast.

The cast was worn until the metaphyseal juxtaphyseal radiolucency disappeared from the radiographs (Betz *et al.*, 1990). The patients were immobilized for an average duration of approximately 12 weeks. Unfortunately, this method has a high rate of complications. In addition to the complications, the cast is uncomfortable and cumbersome for both the patient and the family (Loder *et al.*, 2000).

2.4.2 Single-screw fixation

This technique is seen as the gold standard treatment method when treating patients with acute SCFE (Balasubramanian *et al.*, 2019). In situ single-screw fixation involves placing a screw in the centre of the epiphysis to maintain the position of the femoral head and prevent further slippage. The screw is placed perpendicular to the physis to stabilize the slip without forceful reduction and eventually the growth plate will close or fuse (Loder, 1998). Since the method is highly image-dependent, clear visualizations of the femoral head and neck are essential before the procedure starts. This method is the most commonly preferred treatment due to its high success rate and the low prevalence of additional slippage and complications (Loder *et al.*, 2000). This method is illustrated in Figure 2.5.

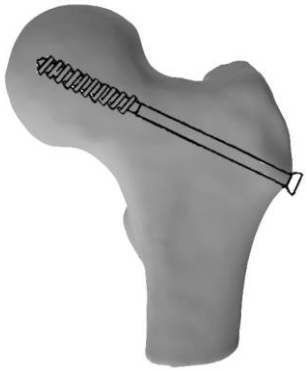

Figure 2.5: Illustration of the single-screw fixation method

2.4.3 Bone graft epiphysiodesis

By using bone graft epiphysiodesis to treat SCFE, complications associated with internal fixations such as damage to the lateral epiphyseal vessel and unrecognized pin protrusion are avoided (Aronsson *et al.*, 2006). This surgical technique involves harvesting bone grafts from the iliac crest and placing it in the femoral neck. The procedure is approached with anterior iliofemoral exposure of the hip joint where a rectangular window of bone is removed from the anterior neck of the femur as shown in Figure 2.6 (Ferguson and Howorth, 1931). A cylindrical tunnel across the physis is created using a hollow mill. Corticocancellous

strips of iliac crest bone graft used as bone pegs are then driven across the physis into the epiphysis (Aronsson *et al.*, 2006). According to Loder *et al.* (2000), the advantage of this technique is that it reduces the risk of damage to the blood supply of the femoral head as the graft is inserted at the correct angle at the centre of the femoral head. However, the fixation is not as stable as the fixation achieved through in situ fixation and the procedure leads to a longer duration of anaesthesia, increased blood loss and a larger scar (Loder *et al.*, 2000).

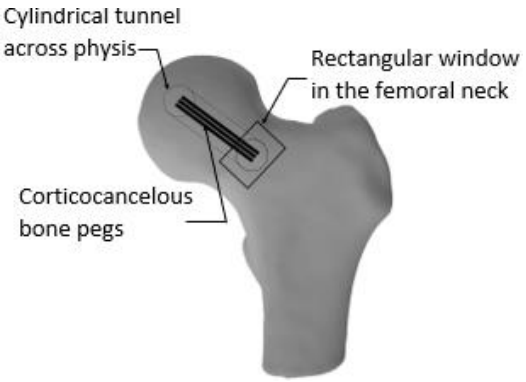

Figure 2.6: Illustration of the bone graft epiphysiodesis method

2.4.4 Compensating base-of-neck osteotomy

An anterosuperior-based wedge osteotomy, described by Kramer *et al.* (1976), is a surgical technique where multiple pins are used to stabilize the osteotomy site and SCFE, however, some of the patients in this study did develop some complications. Barmada *et al.* (1978) described a technique, the extracapsular basilar neck osteotomy, which is used to repair the SCFE while avoiding avascular necrosis. The occurrence of avascular necrosis is lower than that of cuneiform osteotomy, but the technique has a correction limited to 35-55 degrees of the slip angle. An advantage of the basilar neck osteotomy is that it improves hip motion, but it shortens the neck of the femur. During hip abduction, this could lead to impingement of the greater trochanter against the lateral of the acetabulum (Loder *et al.*, 2000).

2.4.5 Cuneiform osteotomy

Cuneiform osteotomy is a surgical technique that involves an anterolateral or anterior Smith-Peterson view of the hip (De Rosa *et al.,* 1996). A bone wedge is removed from the femoral neck metaphysis which allows anatomical repositioning of the epiphysis on the metaphysis without adding tension to the epiphyseal vasculature. Once the femoral neck is adequately shortened, the epiphysis is reduced, and three pins are used to fixate the head internally (Fish,

1984). This technique, however, has shown subsequently poor results and has a high risk of avascular necrosis (Loder *et al.*, 2000).

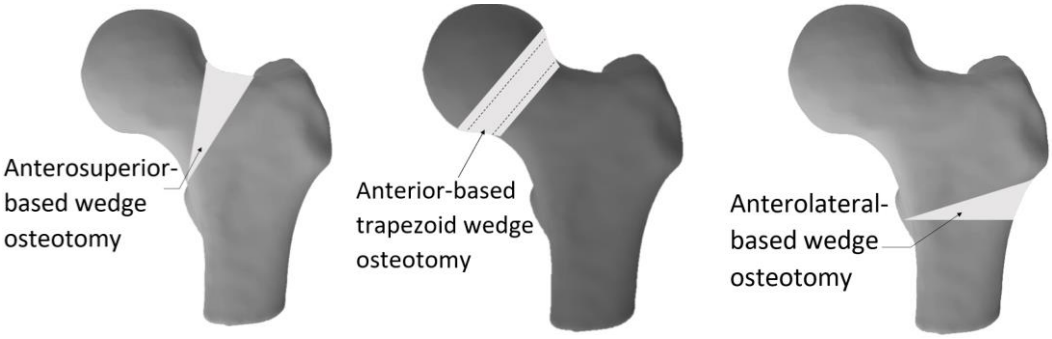

(a) Base-of-neck (b) Cuneiform (c) Intertrochanteric

Figure 2.7: Different osteotomies used for the correction of SCFE

2.4.6 Intertrochanteric osteotomy

An intertrochanteric osteotomy through the lesser trochanter as described by Southwick (1967), improves hip motion without being associated with avascular necrosis. It involves an intertrochanteric osteotomy with abduction, flexion and internal rotation of the distal fragment where the osteotomy site and the SCFE are fixed with a compression hip screw (Loder *et al.*, 2000). However, if the slip is unstable it is fixed with a percutaneous cannulated screw. Similar to the base-of-neck osteotomy, the intertrochanteric osteotomy is also compensating with a correction limit of 45 degrees on the anteroposterior view and 60 degrees on the lateral view as measured by the Southwick method (Southwick, 1973). A correction larger than 60° could result in excessive femoral shortening. Although this technique has the advantage of being safe since it has a very low risk of avascular necrosis, according to Aronsson *et al.* (2006), this technique is technically demanding and therefore should only be considered for patients with an SCFE slip larger than 40 degrees.

2.4.7 Unstable SCFE

Compared to stable SCFE, unstable SCFE is a more severe disorder. The risk of complications, especially osteonecrosis, in patients with unstable SCFE is considerably higher (Peck *et al.*, 2017). The treatment options for unstable SCFE are similar to the options described for stable SCFE but there are controversies regarding some of the factors regarding the treatment such as the timing of the surgery, reductions of the SCFE, aspiration of the hip joint and single- vs double-screw fixation (Aronsson *et al.*, 2006). A technique currently recommended is the Dunn procedure which restores the alignment of the proximal femur through a

surgical hip dislocation and reduces the prevalence of femoroacetabular impingement (Abu Amara *et al.* 2014). Postoperatively the patients are non-weight-bearing for approximately 6-8 weeks (Gholve *et al.*, 2009).

2.5 Pre-operative planning

In most cases, the single-screw fixation technique is a sufficient method for stabilizing the SCFE, but to improve the hip joint's range of motion or to eliminate impingement in more severe SCFE cases a correction osteotomy is considered (Richolt *et al.* 1999). From the possible osteotomies implemented at various positions on the proximal femur, an intertrochanteric osteotomy is a preferred technique as it is safer due to its low risk of avascular necrosis (Kamegaya *et al.* 2005). The pre-operative planning methods for this technique are described below.

2.5.1 Traditional method

Pre-operative surgical planning is an indispensable requirement for the success of any orthopaedic surgery (Hak and Rose, 2010). Traditionally pre-operative planning for intertrochanteric osteotomy relies on two radiographs namely the anteroposterior and frog-lateral radiographs (Merchán *et al.* 1992). These radiographs allow for the extraction and evaluation of the femur geometry. The extracted geometry, such as the neck-shaft angle (NSA), is used to determine the severity of the SCFE and therefore the amount of correction applied in the osteotomy (Kordelle *et al.* 2000). According to Graham *et al.* (2018), the procedure consists of the following steps:

1. Using the method described by Southwick (1967), the head-shaft angle is measured on both the AP and the frog-leg lateral radiographs. The obtained measurements of the affected hip are compared to the contralateral hip when unilateral pathology is present. If the patient is diagnosed with bilateral SCFE, measurements of 145° on the AP view and 10° on the lateral view are used. The difference between the two hip measurements is used to determine the varus and extension deformity as shown in Figure 2.8. The severity of the deformities determines the amount of surgical correction used in the osteotomy.

2. The proposed osteotomy line is marked on the two radiographs. The line is indicated just above the lesser trochanter.

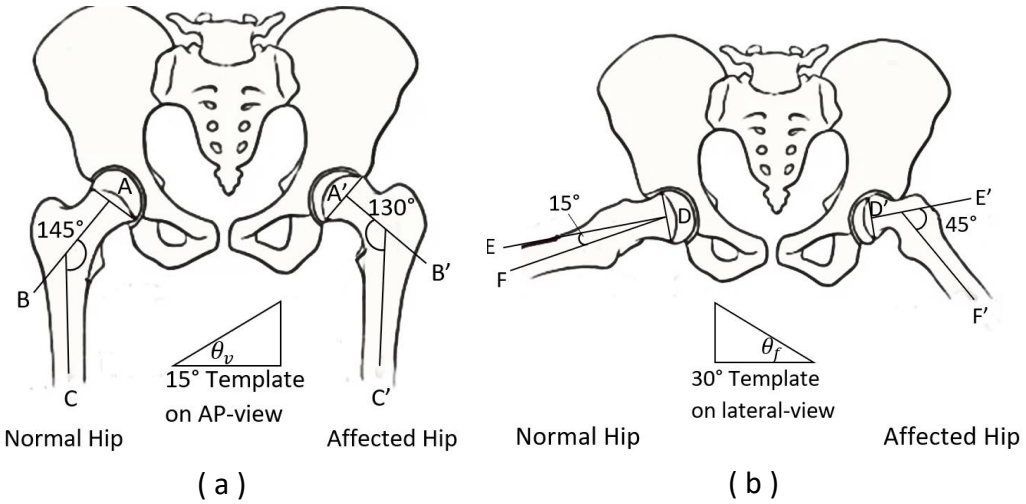

Figure 2.8: Measurement of the head-shaft angle on the (a) AP view and the (b) frog-leg lateral view

3. On the AP radiograph, a line is drawn from the medial extent of the proposed osteotomy at an angle "θ_v" which equates to the proposed valgus correction. A guidewire and thereafter a seating chisel will be inserted superior and parallel to this line. This can be seen in Figure 2.9.

4. On the lateral radiograph, a line is drawn from the posterior extent of the proposed osteotomy at an angle "θ_f" which equates to the proposed flexion correction. The seating chisel's blade will be superior and parallel to this line and aimed at the midpoint of the femoral neck.

5. To determine the length of the blade and the size of the implant required a template of the blade plate can be traced onto the radiographs.

6. A mock trial can be performed on tracing paper to confirm the preoperative measurements.

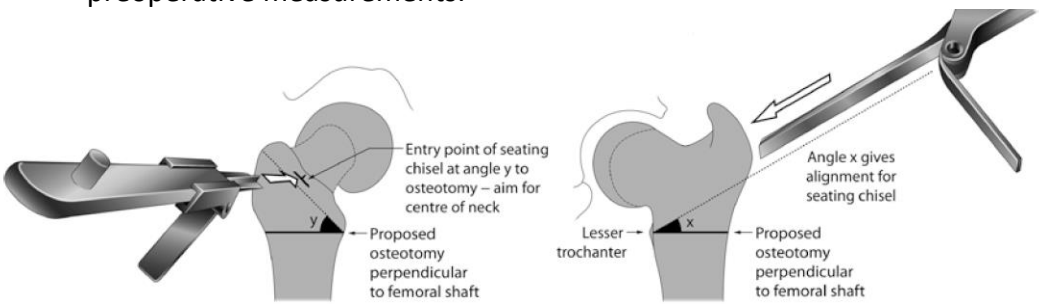

Figure 2.9: The proposed osteotomy line, along with the flexion and valgus correction angles indicated on the radiographs during preoperative planning (Illustration obtained with permission from Graham et al. (2018)) *Angles x and y in the figure represent θ_v and θ_f respectively.

2.5.2 Other methods

Although the traditional method of pre-operative planning based on 2D radiographs has proven sufficient for a subset of procedures, the method does have some disadvantages such as it being cumbersome and time-consuming. Another problem of x-ray imaging is trying to establish the proper positioning of the examined body part, especially in children (Drapikowski *et al.*, 2008). Incorrect positioning, overlapping anatomical structures, lack of information, and quality of radiographs can cause errors in measurements made which decreases the accuracy of the correction surgery (Kordelle *et al.*, 2000). Since the 3D anatomy can not be completely viewed from the 2D radiographs, the accuracy, efficiency, and duration of the surgery depend on the knowledge and experience of the surgeon planning and performing the surgery (Drapikowski *et al.*, 2008).

The deformity correction of the SCFE can be complicated, regardless of the osteotomy chosen, due to the complicated 3D pathological structure and the inability to visualize the femoral head-neck junction using the standard approach (Cherkasskiy *et al.* 2017). Various studies have proposed using a 3D patient-specific model for pre-operative planning which would provide exceptional information on the bone shape and accurate measurements that could not be achieved with traditional x-ray imaging (Yu *et al.* 2016).

In a study done by Kamegaya *et al.* (2005), the degree of correction to perform the osteotomy was measured using traditional radiographs, but the direction of the correction was determined using computed tomography. CT scans provide more three-dimensional information which is used to determine the plane of the osteotomy. Different CT slices in the axial plane were used to determine an axis along the lateral aspect of the femur and the provisional axis. The alpha angle was determined by measuring the angle between these two axes on a superimposed image.

Cherkasskiy *et al.* (2017), proposed a study that used 3D-printed patient-specific models to perform pre-operative planning. To construct a 3D model, the patient underwent a pelvic CT scan to obtain a 3D image consisting of several image slices of the patient's anatomy. The CT scan was then used to segment the proximal femur from the image and convert the segmented femur to a 3D printable format. These models were then 3D printed and used for pre-operative planning and mock surgeries to allow the surgeon to visualize the femoral head-neck junction and optimize the correction surgery.

Drapikowski *et al.* (2008) described how a simulation-based approach could be used for surgical planning. CT scans were used to obtain the 3D images of the patients whereafter 3D reconstruction was performed on the CT images to obtain surface models of the bony structures. The surface model was then calibrated to

define a standardized, repeatable position of the model. The software developed by Drapikowski *et al.* (2008), SCFE analyzer, allows for spatial analysis and could be used to calculate the range of motion of the hip joint as well as be used for surgical planning. The computer can determine the severity of the slip and simulate the osteotomy.

Unfortunately, these methods have limitations which are largely due to the use of a 3D volumetric imaging technique such as a CT scan or MRI to obtain the 3D models. The use of these modalities is expensive and time-consuming and the method subjects the patient to a high radiation dose (Hosseinian and Arefi, 2015).

2.6 2D/3D reconstruction

Extensive research had been done to introduce alternative methods in creating 3D patient-specific bony models which eliminate the limitations of the CT imaging modality, but would still provide detailed and accurate 3D information. Currently, computer-aided reconstruction of a patient's 3D anatomy from 2D radiographic images has been considered a reliable alternative (Hosseinian and Arefi, 2015). When using the 3D reconstruction technique, prior information about the shape is included to compensate for the lack of image information provided by the 2D image radiographs (Dakhakhni, 2013). By using the information obtained from the 2D images along with the provided prior information, 3D patient anatomy can be constructed. Hosseinian and Arefi (2015) classifies and describe some of the existing 3D reconstruction methods available in the literature. Different measures are used to classify 3D reconstruction methods. These measures include the level of automation, applications, primitives and models used etc. The existing methods have been classified as methods based on points, contours, statistical models, and parametric models (Hosseinian and Arefi, 2015).

2.6.1 Point-based methods

This reconstruction method is one of the first presented methods for reconstructing 3D models from x-ray images. This method relies on identifying points and matching them on multi-view x-ray images. This method can further be classified as stereo-corresponding point (SCP) and non-stereo corresponding point techniques (NSCP) (Hosseinian and Arefi, 2015).

The stereo-corresponding point-based technique is based on an expert operator manually identifying corresponding points on multi-view radiographs. For this technique to work at least 6 corresponding landmarks needs to be identified (Hosseinian and Arefi, 2015). Prior knowledge is taken into consideration by constructing a generic model from a 3D scanner (Aubin *et al.*, 1997). The patient-specific model is obtained by Kriging the generic model by using the identified SCPs and using a reconstruction algorithm such as Direct Linear Transform (DLT). Kriging

involves the deformation of a generic object through interpolation and extrapolation algorithms to approximate a 3D personalized model consistent with the desired shape (Mitulescu *et al*, 2002). Aubin *et al.* (1997) later suggested using additional points to generate more accurate models in a study where 21 SCP were used to reconstruct the 3D model. The problem with this method is that an anatomical structure has a limited number of corresponding landmarks and when increasing the number of identified SCPs, the method becomes time-consuming.

To improve the limitations of the previous technique, a non stereo-corresponding point based technique was proposed. Unlike the SCP technique where corresponding points on multi-view radiographs are needed to perform reconstruction, the NSCP technique can perform reconstruction by using points that are only visible on one radiograph. The principle of this technique is to deform an elastic object while taking the stereo corresponding and nonstereo corresponding observations available in the various projections into account (Mitton *et al.*, 2000). These methods are based on the idea that any non stereo-corresponding point (NSCP) belongs to a line that extends from the x-ray source to the point's projection in one view (Hosseinian and Arefi, 2015). Using these NSCPs along with other SCPs allows for a more detailed and refined reconstruction by using epipolar geometry to deform generic models.

Mitton *et al.* (2000) and Mitulescu *et al.*, (2001) used this technique in the reconstruction of cervical and lumbar vertebrae respectively. The reconstruction of the SCPs was done by using the DLT algorithm. The NSCPs on the other hand were reconstructed by defining a generic object and the projection line from the x-ray source to the projected point on the radiograph. The points' positions were initialized on the projection lines whereafter an optimization strategy is used to determine the point's position on the line by taking the generic object's shape into account. Lastly, the generic object was Kriged using the reconstructed points as control points.

These NSCP-based techniques are extremely dependent on the ability of the expert operator to identify the anatomical landmarks on the radiographs. Therefore, the method is not very reproducible and can be time-consuming during the landmark identification process (Hosseinian and Arefi, 2015).

2.6.2 Contour-based methods

Another disadvantage to point-based methods is that they cannot be applied to bony structures that have a continuous shape due to the scarcity of specific anatomical landmarks points (Laporte *et al.*, 2003). An improvement to the point-based reconstruction method was proposed by Laporte *et al.* (2003), which can be applied to continuous shapes by applying non-stereo corresponding contours instead of points. This technique aims to manually identify 2D contours from the

x-ray images and associate them with the 3D lines established on the reference shape while deforming a 3D elastic model onto the radiographs with regard to the 2D contours (Hosseinian and Arefi, 2015). The 2D contours are associated to the 3D lines by using contour deviation and point-to-point distances. The projected contours of the initial 3D object surface are optimized and then deformed using the Kriging algorithm. This step is repeated until the distance between the two contours reached a precision value (Laporte *et al.*, 2003). Figure 2.10 shows how Mitton *et al.* (2006) implemented a contour-based reconstruction algorithm to reconstruct the pelvis from 2D images.

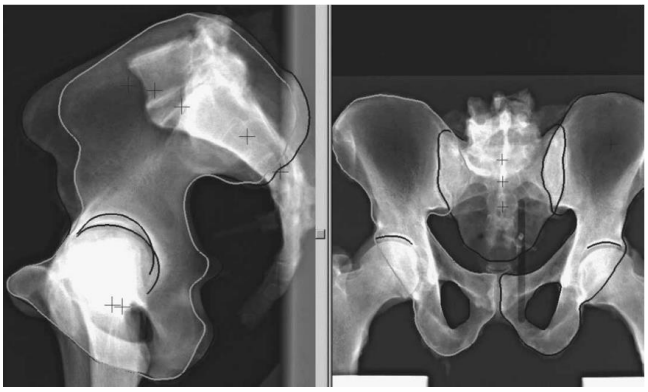

Figure 2.10: Identified 2D contours on the lateral and frontal radiographs (Figure obtained with permission from Mitton *et al*. 2006)

2.6.3 Statistical shape model based methods

This technique is seen as a more automated reconstruction algorithm as it reduces user interaction by considering more information regarding pathological structures and utilising statistical knowledge of possible deformations of the shapes (Hosseinian and Arefi, 2015). A shape model aims to capture all possible variations within a population and thus requires a large training dataset which includes normal and pathological shapes. The model containing the prior information is projected to the radiographs and compared using a similarity measure. The similarity measure uses a set of features or a statistic to compare the projected shape to the radiograph and produces a numerical value which quantifies the similarity of shared information (Reyneke *et al.*, 2018). The shape model is deformed until the projection of the model is consistent with the information on the corresponding radiograph.

2.6.4 Parametric methods

This method uses parametric modelling and takes clinical and anatomical features into account. Rather than using the entire collection of points as suggested by Statistical Shape Modelling, the statistics are conducted on anatomical descriptive parameters (DP) which are extracted from the surface of interest (Quijano *et al.*,

2013). A simplified parametric model is specified to depict the target objects. This simplified model is constructed according to the observed bony structure by using different geometric primitives such as circles, lines, points and spheres (Lebailly *et al.*, 2012).

A database of parameters is established from the training 3D models for statistical inference through the use of simplified parametric models. Based on the digitized anatomical landmarks on the calibrated radiographic images, the main descriptors are determined and used to estimate a full set of DPs according to the statistical model. The full set of DPs is used to obtain a simplified personalized parametric model (SPPM) and according to Quijano *et al.* (2013) deforming a morpho-realistic generic mesh into the SPPM results in a morpho-realistic personalized parametric model (MPPM). The resulting model is then projected onto the corresponding radiographs to compare the information of the images to the model and to make possible adjustments. Humbert *et al.* (2009), used a parametric model for vertebrae of the spine, as indicated in Figure 2.11.

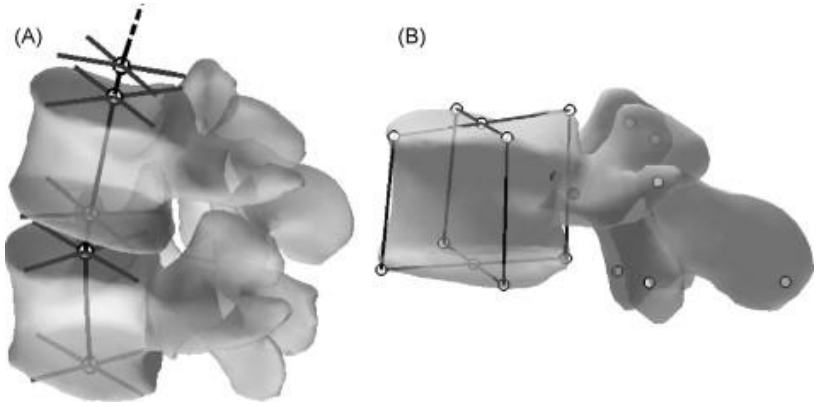

Figure 2.11: Parametric model of the spine (a) consisting of L4 and L5 and the (b) L4 vertebra (Figure obtained with permission from Humbert *et al*. 2009)

2.6.5 Discussion

According to Hosseinian and Arefi (2015), none of these methods described above can be chosen as the superior method as all of these methods have their advantages and disadvantages that should be taken into account when considered for usage. Due to the simplicity of point-based processes, the method is still implemented for 3D reconstruction and is usually used as an initial estimation for other methods. However, the drawbacks of point-based reconstruction include low reproducibility, limited accuracy, being time-consuming and being highly dependent on the skill and experience of the operator. This is due to the difficulty associated with accurately identifying and matching points on multiview radiographs and the limited number of corresponding landmarks visible on the radiographs. Point-based reconstruction cannot be implemented on bony

structures with a continuous shape due to the limited number of anatomical landmarks present (Hosseinian and Arefi, 2015).

In contour-based methods, the user intervention required is less than in point-based methods since the method uses contours instead of points for 3D reconstruction. The accuracy of this method is acceptable and closely resembles the result of CT scans, but this is still seen as a time-consuming method when applied to clinical applications according to Hosseinian and Arefi (2015). Reconstruction based on statistical shape models is more automated than the previous methods as it reduces user intervention by including prior information about pathologic objects. The reconstruction time of this method varies, but the method is limited by the large training dataset required to construct a statistical shape model. Lastly, the parametric-based reconstruction approach has improved convergence and robustness and is suitable for providing a quick and reliable initial 3D reconstruction. This method is also known to have acceptable reproducibility.

According to Sarkalkan *et al*. (2014), statistical shape modelling is used extensively throughout the orthopaedic field. Chan *et al.* (2013) stated that an SSM could offer useful metrics regarding the characteristic macroscopic shape patterns that are present in a case of SCFE. Since a shape model aims to capture all possible variations within a population it can be used as prior knowledge during the reconstruction algorithm. Various studies throughout the literature have applied this method to the reconstruction method. Fleute *et al.* (1999) proposed a method where a 3D model of the distal femur is constructed by deforming the shape model to match the 2D contours segmented from x-ray images. This proposed method resulted in a reconstruction with an average error of 0.99 mm. Benameur *et al.* (2003) used a shape model-based method to reconstruct vertebrae where the mean error of the reconstructed models was 0.71 mm for the lumbar and 1.48 mm for the thoracic vertebra. Other researchers such as Zheng *et al.* (2009), proposed using the reconstruction method to reconstruct the proximal femur and achieved an average reconstruction error of 1.2 mm. Based on the information provided in the literature review, a shape model based reconstruction technique will be implemented within this study.

Chapter 3

Statistical shape models

This chapter will focus on explaining what Statistical Shape Models are and how they are constructed. Section 3.1 explains how the data, used to build the shape model, have been acquired and how it has been processed to be used in shape modelling. Section 3.2 gives an overview of shape models followed by Section 3.3 which details how the SSM has been constructed. Lastly, Sections 3.4 to Section 3.6 explains how the model has been validated and the results are discussed.

3.1 Processing and segmentation

The SSM was constructed using CT data of the proximal femur that were analysed retrospectively, but in order to do so, an ethical exemption was required. Since this study was executed retrospectively with a dataset that is publically available and the study required no patient contact it was considered that the study poses a minimum risk and that ethical exemption could be obtained. After ethical exemption was received (Reference: X21/03/007) the existing collection of CT images was retrieved from the Shapeworks Data Portal, which is available for public access at https://girder.shapeworks-cloud.org/.

This specific dataset was the femur-v0 dataset under the use-case-data-v2 collection on the portal. The collection and processing of the data were originally supported by the National Institutes of Health (NIH), grant numbers U24-EB029011, R01-AR076120, R01-EB016701, R01-GM083925, R21-AR063844, and completed within the Orthopaedic Research Laboratory of the University of Utah. The dataset is composed of CT scans of the hip obtained from 33 study volunteer participants, with an average age of 29 years old, ranging from 15 to 55 years old, who had no history of hip pain and no signs of osteoarthritis or bony abnormalities. The study participants had been imaged as part of previous unrelated studies with approval from an institutional review board (University of Utah IRB numbers 11755 and 56086; Intermountain Healthcare IRB number 1024270) and were originally collected for research purposes, specifically for the evaluation of hip biomechanics (Atkins *et al.*, 2019).

The raw data was in a nearly raw raster data (.nrrd) file format and the slices had a resolution of 512 x 512 pixels with a thickness of 1 mm in the axial plane with pixel sizes ranging from 0.61 to 0.85 mm with an average spacing of 0.7 mm. The software program used for the segmentation process was 3D Slicer, Version 4.11, which can be obtained from https://www.slicer.org/. 3D Slicer is a free, open-source software application that is used for the visualization and analysis of

medical image computing datasets. The proximal femur was segmented from each CT scan in the dataset by following the protocol below.

1. Use the Crop Volume module to reduce the image volume to the region of interest, which is the left proximal femur.

2. The proximal femur was isolated by manually adjusting the threshold. This resulted in a mask that describes all the geometries within the thresholding range.

3. By stepping through all the slices, the mask was cleaned and edited manually by using the tools available in the Segment Editor module of 3D Slicer. The cleaning process consisted of closing irregular gaps and areas of poor contrast, erasing unwanted artefacts, removing islands whose anatomy does not represent those of the proximal femur, and smoothing the mask.

4. Once the editing phase has been completed the mask was used to generate a surface mesh of the femur.

5. By using the decimation tool in the 3D Slicer Surface Toolbox module, the mesh was simplified by reducing the number of surface points to about 10 000 points.

6. A mask was generated from the reduced mesh and compared to the CT scans for visual inspection. Figure 3.1 shows an instance of this step, where a mask of the proximal femur is visible in the different planes of a CT scan.

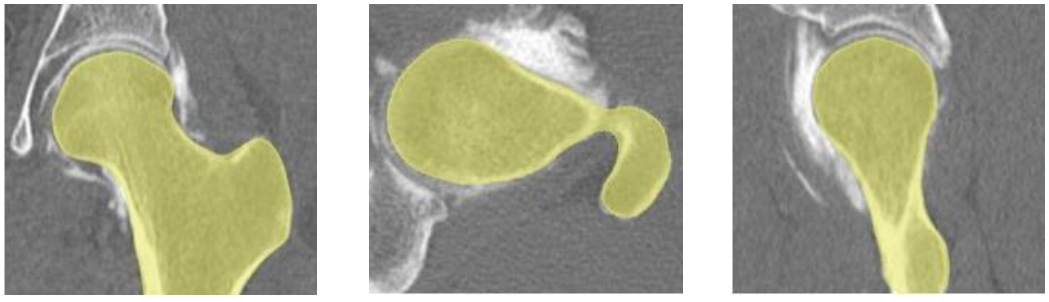

(a) Coronal plane (b) Axial plane (c) Sagittal plane

Figure 3.1: Mask of the proximal femur (yellow) visible in the different planes of the CT scan.

7. Once the mask was validated, the final mesh was exported to a stereolithography (.stl) file as face-vertex data.

3.2 Overview of a shape model

Statistical shape models are the result of a combination of the analysis of training data and the understanding of a population and aim to capture possible variations within a population (Bryan *et al.* 2009). Sarkalkan *et al.* (2014) stated that these models are usually based on the analysis of a set of training data which provides the model with prior knowledge about the expected shape distribution of the object. Based on the definition, a shape model can be used to explain the anatomical variation within a population of bony shapes, where the population can vary from patients with a skeletal disease to a group of healthy individuals with a shared ethnic background (Sarkalkan *et al.*, 2014).

Being able to fit these models to new unseen data within the same population, creates the opportunity to construct a three-dimensional patient-specific bone model of the shape. These 3D patient-specific models can then be used in a variety of medical applications such as bone motion tracking, or, in the case of this study, for pre-operative surgical planning for SCFE (Sarkalkan *et al.*, 2014).

According to Heimann and Meinzer (2009), the methods employed to construct an SSM strongly depend on the chosen shape representation. Among the various shape features available, the most common descriptor for bone are landmarks which are manually placed on bone shape features, with the number of points usually in the tens. However, most modern attempts rather use a dense set of landmark points, which number in the order of thousands (Reyneke *et al.*, 2018). Figure 3.2 illustrates how a dense set of landmarks along with the connectivity information could be used to represent the femur as a face-vertex surface mesh. Lüthi *et al.* (2017) stated that Point Distribution Models (PDMs) are an important class of statistical shape models. PDMs are linear, parametric models that use the point positions of an object's boundary to represent the shape as a set of labelled points. A PDM is typically trained using a set of example shapes $\{\Gamma_1, \dots, \Gamma_n\}$, where each shape is represented by a set of discrete points: i.e $\Gamma_i = \{x^i{}_j | x_j \, \epsilon \, \mathbb{R}^3, \; j = 1, \dots, N\}$ with N denoting the number of points (Lüthi *et al.*, 2017).

When constructing a PDM there are three main steps to consider, namely correspondence, data alignment and variance extraction. Correspondence is one of the largest factors that can influence model quality (Heimann and Meinzer, 2009). A shape model requires that the points from the shapes in the training dataset are all in correspondence to ensure that the anatomical variance of a set of data is correctly interpreted.

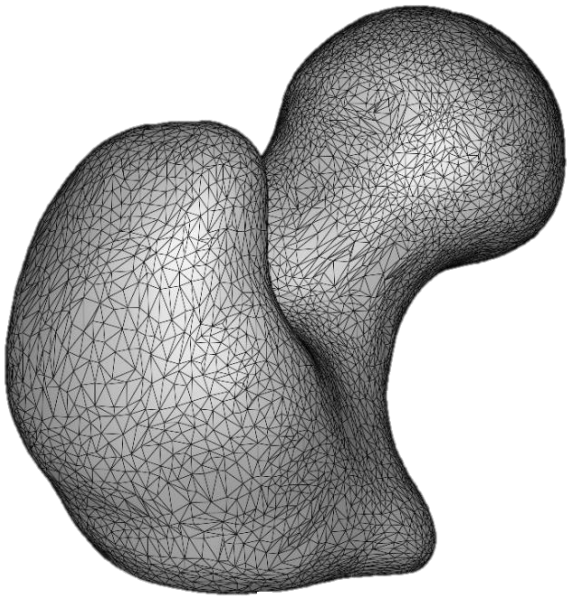

Figure 3.2: A dense surface mesh

Correspondence means that the landmarks should be defined in such a way that the jth landmark point would represent the same anatomical location on all of the shape instances in the dataset (Lüthi *et al.*, 2017; Sarkalkan *et al*., 2014). This is usually achieved through manual identification of the landmarks or by using algorithms that automatically compute correspondence by performing registration between all involved shapes (Heimann and Meinzer, 2009).

Commonly, an anatomical shape is described as the geometrical information that remains when the effects of rotation and location are filtered out from an object, but not the size. This is due to shape and size often being correlated in biology (Stegmann *et al.*, 2000). Thus, once correspondence has been established between the shapes in a set of training data the next step would be to align all the training shapes to the same coordinate frame to reduce variations between shapes resulting from factors other than variation in shape. Shape alignment can be achieved through the alignment of manually placed landmarks or through algorithms that automatically align the shapes like the General Procrustes Analysis (GPA) (Heimann and Meinzer, 2009; Sarkalkan *et al.*, 2014).

Lastly, a set of modes that best describe the observed shape variations is extracted by using statistical analysis. According to Lüthi *et al.* (2017), the usual assumption is that shape variations can be modelled using a normal distribution $s \sim \mathcal{N}(\mu, \Sigma)$, where the mean, μ, and the covariance matrix, Σ, can be calculated as:

$$\mu = \bar{s} \coloneqq \frac{1}{n}\sum_{i=1}^{n}\overrightarrow{s_i} \quad (1)$$

$$\Sigma = S \coloneqq \frac{1}{n-1}\sum_{i=1}^{n}(\overrightarrow{s_i} - \bar{s})(\overrightarrow{s_i} - \bar{s})^T \quad (2)$$

The covariance matrix, Σ, measures the variance in the different training shapes from the mean shape $\bar{s}$ (Sarkalkan *et al.*, 2014). Once the covariance matrix is obtained, Principal Component Analysis (PCA) is performed on the matrix Σ to calculate the eigenvectors (main modes of variation) Φ_i along with the corresponding eigenvalue (variance) λ_i (Reyneke *et al.*, 2018). The resulting eigenvectors are then sorted in descending order with regard to the percentage shape variation explained by that eigenvector. This is done so that the modes of variation with the most variance would be able to describe most of the possible shape distributions within the population (Cootes and Taylor, 2004; Heimann and Meinzer, 2009). A shape instance in the population can therefore be described as:

$$\boldsymbol{s} = \bar{s} + \sum_{i=1}^{M} b_i \Phi_i \quad (3)$$

where b_i describes the contribution of the first *M* modes of variation. The number of modes retained affects the accuracy and the compactness of the model. A larger number of retained modes would mean that the model would describe the bone shape more accurately but the model would be less compact (Stegmann *et al.*, 2000). A common approach used for determining the number of modes required is to determine the ratio, γ, between the accumulated variance and the total variance of the model.

$$\gamma = \frac{\sum_{i=1}^{M}\lambda_i}{\sum_{i=1}^{n-1}\lambda_i} \quad (4)$$

The ratio is generally acceptable when $0.9 \leq \gamma \leq 0.98$, anything outside the ratio could lead to overfitting (Heimann and Meinzer, 2009; Sarkalkan *et al.*, 2014).

3.3 Constructing a shape model

The previous section mentioned that PDMs are the technique most frequently used for representing bone shapes. These models that make use of PCA to determine the shape variations can only represent shapes within the linear span

of the training shapes. This means that in order for the model to represent all possible target shapes in a population a lot of training data is needed (Thusini *et al.*, 2020). It could be difficult to obtain sufficient training data due to privacy issues, the lack of substantial benefit for recruiting volunteers to undergo CT scans or a lack of already available cases in a database (Muschelli, 2019).

To overcome this problem, a method described by Lüthi *et al*. (2017), which generalizes the PDMs to define Gaussian Process Morphable Models (GPMM), was employed in this study. These models do not restrict the covariance matrix to the covariance matrix obtained from the training shapes but instead, allows for any valid positive definite covariance matrix to be used (Reyneke *et al.*, 2018).

The approach to constructing a GPMM consists of two important steps. Firstly correspondence needs to be established between all the shapes in the training dataset and secondly, the deformations are modelled using a Gaussian Process $\mathcal{GP}(\mu_{GP}, k_{GP})$ where μ_{GP} is the mean function and k_{GP} the covariance function (Lüthi *et al.*, 2017). The process of constructing a GPMM is illustrated in Figure 3.3.

The shape model was constructed using Scalismo. Scalismo is an open-source library for statistical shape modelling and model-based image analysis in Scala and was developed by the University of Basel, Switzerland. A development environment namely, Intellij IDEA (https://www.jetbrains.com/idea/) was used to program in Scala.

3.3.1 Identify reference shape

In order to construct a GPMM, a reference shape, Γ_R, needs to be identified from the training data set $\{\Gamma_1, \dots, \Gamma_n\}$. As mentioned above, the deformations are modelled using a GP and consist of a mean and a covariance function. As deformation fields are being modelled, that means that the mean function also consists of a deformation field and when considering shape models, the mean function can be thought of as the field that deforms the reference into the mean shape (Lüthi and Bouabene, 2020). When the reference shape closely resembles the mean shape of the population and no further knowledge regarding the dataset is available, a zero mean deformation can be used in the GP. Thus, when selecting a reference shape, the reference should approximate the mean shape as closely as possible to justify the use of a zero-mean GP (Lüthi and Bouabene, 2020).

It was decided to determine the reference shape by analysing the volume of each of the training shapes. 3D Slicer offers a module called Models, which provides information regarding a surface model including the volume, in cubic millimetres.

Thus, when the shapes were extracted from the CT scans, the volume of each of the surface meshes could also be found. The average volume was determined and

the training shape with a volume closest to the average volume, $V_{avg} \approx V_{\Gamma_i}$ was selected as the reference mesh $\Gamma_R \approx \Gamma_i$.

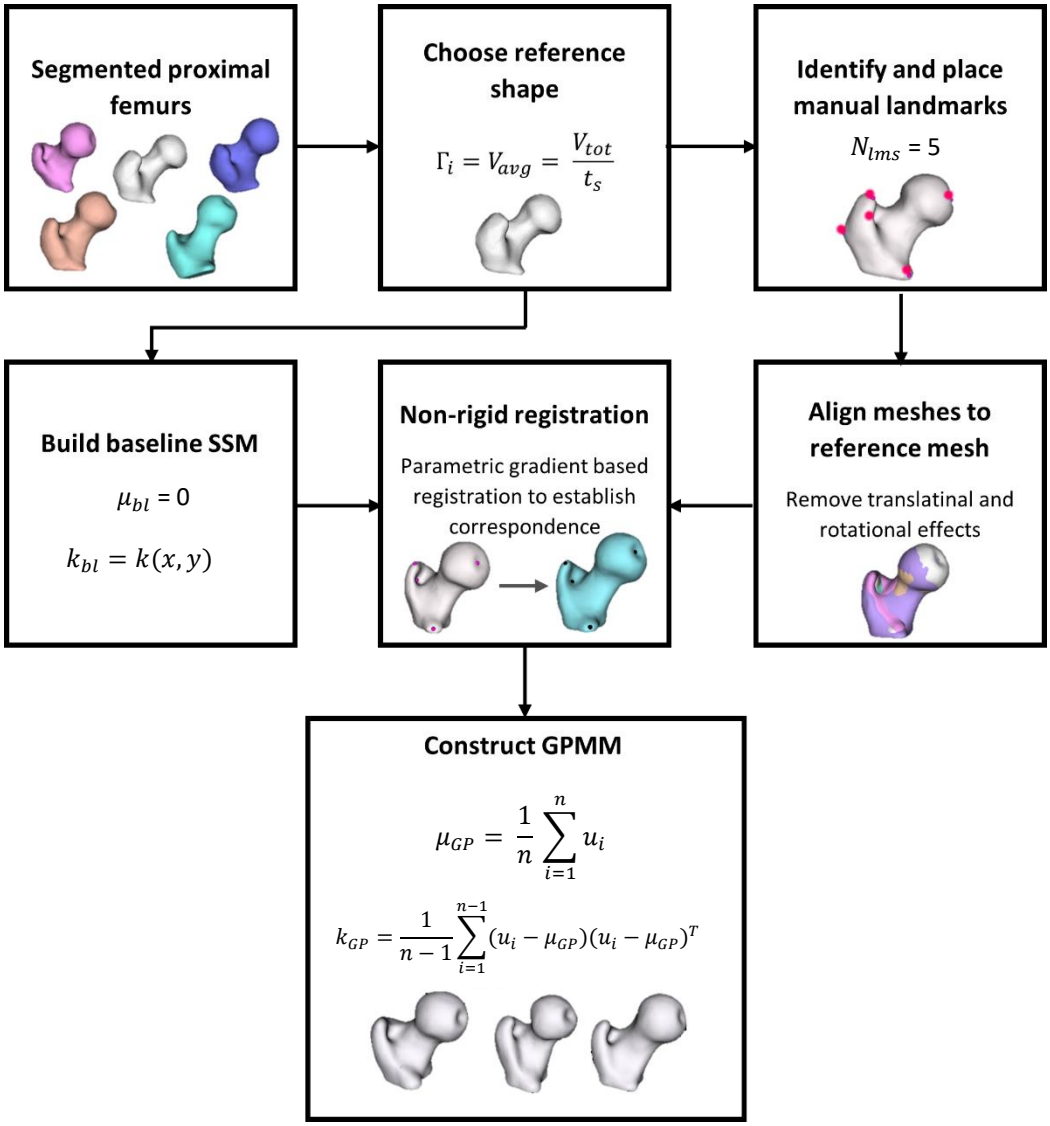

Figure 3.3: Flowchart of SSM construction

3.3.2 Landmark placement

One of the tasks that need to be performed is to rigidly align all the training meshes to the reference shape i.e. normalizing the pose of the shapes. To be able to align these shapes, anatomical landmarks were placed manually on each one of the face-vertex surface meshes. Anatomical landmarks are a set of points that are located at the salient features across the surface of a bony structure (Heimann and Meinzer, 2009). Five landmarks (N_{lms} = 5) were placed on each of the training

shapes. These landmarks are the landmarks discussed in Section 2.2. The identified landmarks can be seen in Figure 3.4.

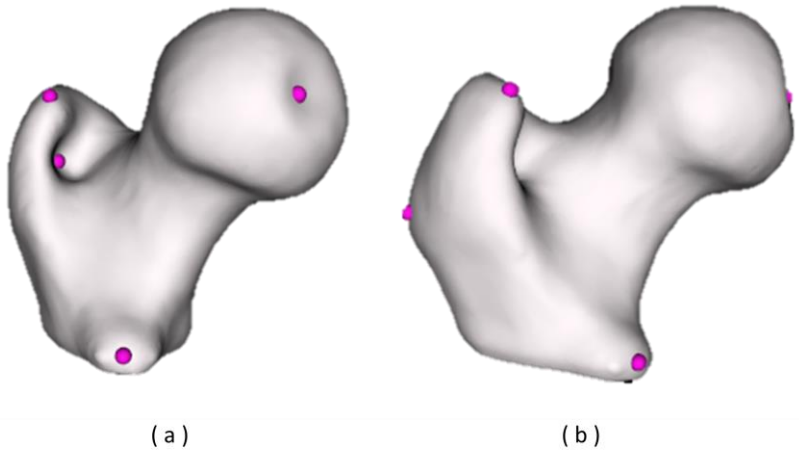

Figure 3.4: Manual landmarks of proximal femur

The landmarks were identified and placed on the mesh using the landmark tool in the Scalismo graphical user interface. The landmarks were placed consistently, in the same order and saved under corresponding labels, to establish some correspondence between the landmarks. It was assumed that the landmarks were placed with a radial uncertainty of 5 mm. This error was accommodated by introducing a noise variable into the fitting algorithm.

3.3.3 Align shapes to the reference shape

To establish correspondence it is necessary to align the training samples in such a way that variations resulting from rotational and translational effects are removed. This ensures that the deformation fields between the reference and training shapes are pure shape changes. The most popular alignment method is the Procrustes Analysis (PA) (Sarkalkan *et al.*, 2014). The main idea behind PA is to align the shapes in such a way that the mean squared distances are minimized.

The landmarks identified in Section 3.3.2 were used to align the training meshes to the reference mesh. Using the method `rigid3DLandmarkRegistraition` from the Scalismo library along with the list of landmarks, the rigid transformation matrix which best aligns the training mesh with the coordinate frame of the reference mesh is determined. The rigid transformation matrix uses translational and rotational functions to accomplish the alignment of the shapes (Lüthi and Bouabene, 2020). The alignment process was visually inspected to ensure all the meshes fall within the same coordinate frame as seen in Figure 3.6.

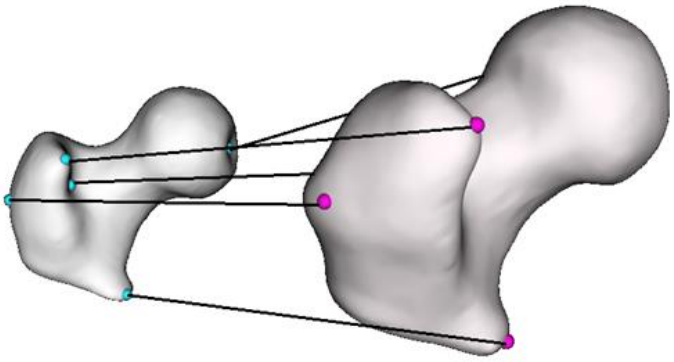

Figure 3.5: Rigid alignment of two surface meshes

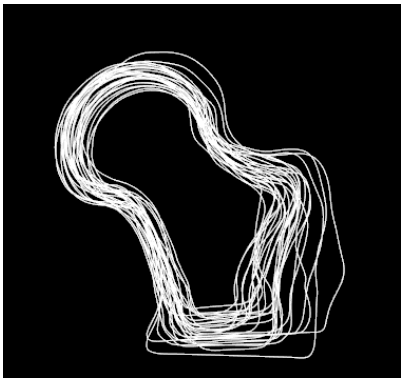

Figure 3.6: Training shapes aligned to the reference mesh

3.3.4 Establish correspondence

Once all the training meshes have been aligned with the reference shape, correspondence needed to be established among these shapes. The process of establishing correspondence is often referred to as registration. For registration, possible deformations are usually modelled using a GP, $u \in \mathcal{GP}(\mu_{GP}, k_{GP})$, with a mean function $\mu_{GP} : \Omega \rightarrow \mathbb{R}^3$ and a covariance function $k_{GP} : \Omega \times \Omega \rightarrow \mathbb{R}^{3x3}$. Sampling a deformation $\hat{u}$ from this GP, generates a new shape, Γ, by warping the reference shape Γ_R:

$$\Gamma = \{x + \hat{u}(x) | x \in \Gamma_R\} \qquad (5)$$

Because the reference shape closely approximates the mean shape, a simple GP can be constructed by using a zero mean function and a Gaussian kernel as a covariance matrix kernel. The scalar-valued Gaussian kernel that enforces covariance between the value of any pair of points x, y is defined by:

$$k_g(x, y) = \exp\left(-\|x - y\|^2/\sigma^2\right) \quad (6)$$

where σ^2 defines the smoothness of the deformation as it is the distance over which the deformations are correlated. This means that choosing a large σ, will lead to smooth deformations over the specified region, whereas a small σ will lead to more local deformations (Lüthi & Bouabene, 2020). To obtain the corresponding matrix-valued kernel that is used for the registration process, the scalar-valued kernel is multiplied with an identity matrix and defined as:

$$k(x, y) = s_v \cdot I_{3x3} k_g(x, y) \quad (7)$$

Where the identity matrix, I_{3x3}, implies that each space dimension component (x,y,z) of the vector field is treated independently and s_v indicates how much variance is being modelled as it is used to scale the variance.

An advantage of modelling with GPs is that simple kernels, like the kernel in Equation 7, can be combined to define a new kernel which allows the construction of models that combine deformations on multiple scales with varying smoothness (Lüthi *et al.*, 2017). In this study, deformations were modelled on multiple scale levels by summing kernels that model smooth deformations with a kernel that models more local deformations. This kernel is defined as:

$$k_{sum}(x, y) = k_1(x, y) + k_2(x, y) \quad (8)$$

where each kernel is modelled with a decreasing bandwidth and scale. This multiscale kernel increases the flexibility of the model. Once the mean and covariance function has been established the simple GP can be constructed. Now deformations can be sampled from any desired set of points, which in this case is the points of the reference shape, Γ_R.

Whenever deformations are sampled from the GP using the `sampleAtPoints` method, a matrix of dimensionality Nd_{out} x Nd_{out} is created internally, with N being the number of points and d_{out} being the output dimension. If it is needed to sample from a large number of points, the memory will run out quickly. To overcome this problem, a low-rank approximation of the GP is obtained resulting in a parametric representation of the GP. This is achieved using a Pivoted Cholesky approximation to compute a finite-rank approximation of the GP. The rank (number of basis functions) is automatically chosen in such a way that a given relative error is achieved. The relative error is approximated on the points on the reference mesh and measured in terms of the variance of the GP. This low-rank

GP is once again applied to the reference shape, Γ_R, which results in a smooth GPMM which is used as the baseline SSM for the registration process.

In the next step, registration to the training meshes is performed. During this study, non-rigid registration is used and the registration problem was formulated as an optimization problem as proposed by Lüthi & Bouabene (2020). To define the registration process four parameters need to be defined, namely:

1. A *transformation space* in which samples from the baseline SSM can be modelled.

2. A *metric* is used to measure the distance between the baseline SSM (reference mesh) and a training mesh (target mesh). The metric is evaluated at some uniformly sampled points on the reference mesh.

3. A *regularizer* which penalizes unlikely transformations.

4. An *optimizer* to perform the minimization of the cost function.

Once these parameters were obtained, the registration object can be defined. Registration is an iterative process which determines the transformation needed to warp the reference mesh into the target mesh (Lüthi & Bouabene, 2020). Thus, the registration is driven by an iterator initialized with a set of parameters, which in this case is a zero-vector the size of the number of basis functions. The parameters of the last iteration are then used to transform the reference mesh into a surface mesh which approximates the target shape. To ensure that the transformed mesh approximates an exact representation of the target mesh all the points on the transformed mesh were projected normally to the closest point on the target shape. This resulted in a fitted mesh which is in correspondence with the target mesh as each point on the fitted mesh closely corresponds with a point on the target mesh.

The regularization weight plays a significant role in the registration process as a large regularization weight leads to a smooth mesh, but fails to closely fit the mesh, whereas if you choose a small regularization weight it could lead to a folded mesh with poor correspondence (Lüthi & Bouabene, 2020). Thus, to ensure that the correct regularization weight is chosen, the registration process is iterated with decreasing regularization weights and with an increasing number of sampled points. This increasing number of sampled points is justified as a model with a larger regularization weight will not be able to fit finer details and thus it is not needed to have a very accurate sample of the mesh.

3.3.5 Build shape model

Now that correspondence has been established between the reference shape and the fitted target meshes, the shape variation of the population is extracted. The shape variations can be stored within a GP by constructing a GPMM using the reference shape and a dataset of fitted target meshes. The dataset of surface meshes is turned into a sequence of deformation vector fields, $\mathbf{u} = \{u_1, \ldots, u_N\}$, from which the model is built. The deformation fields are computed by taking the difference between a point on the reference mesh and a corresponding point on the target mesh. Note that the deformation is interpolated to ensure that the vector fields are defined on all points of the reference mesh.

The deformations can be stored by defining a GP $u \in \mathcal{GP}(\mu_{GP}, k_{GP})$ with a mean function $\mu_{GP} : \Omega \rightarrow \mathbb{R}^3$ and a covariance function $k_{GP} : \Omega \,\mathrm{x}\, \Omega \rightarrow \mathbb{R}^{3x3}$ where the mean and covariance function can be determined through:

$$\mu_{GP} = \frac{1}{n} \sum_{i=1}^{n} u_i \tag{9}$$

$$k_{GP} = \frac{1}{n-1} \sum_{i=1}^{n-1} (u_i - \mu_{GP})(u_i - \mu_{GP})^T \tag{10}$$

The resultant covariance matrix has a dimension of $N \,\mathrm{x}\, N$, where N is the number of points used to describe the boundary reference shape. Because this number of points is usually in the thousands, the resulting covariance matrices can become quite large. To solve this problem the PCA is used to represent the GP in terms of an orthogonal set of basis functions (Lüthi *et al.*, 2017). The low-rank approximation can then be used to represent the process as:

$$\tilde{u}(x) \sim \mu_{GP}(x) + \sum_{i=1}^{r} \alpha_i \sqrt{\lambda_i} \phi_i(x) \tag{11}$$

where α_i is a random coefficient which determines the contribution of the eigenvalue/eigenvector pair (λ_i, ϕ_i). Samples from the constructed GPMM can be seen in Figure 3.7, where variation has been learned from 27 training shapes.

3.3.6 Increasing the model flexibility

Due to the limited availability of training shapes, it is often not possible for the SSM to accurately describe the full transformation space which introduces a bias towards the training shapes in the model-based methods. One way of solving this

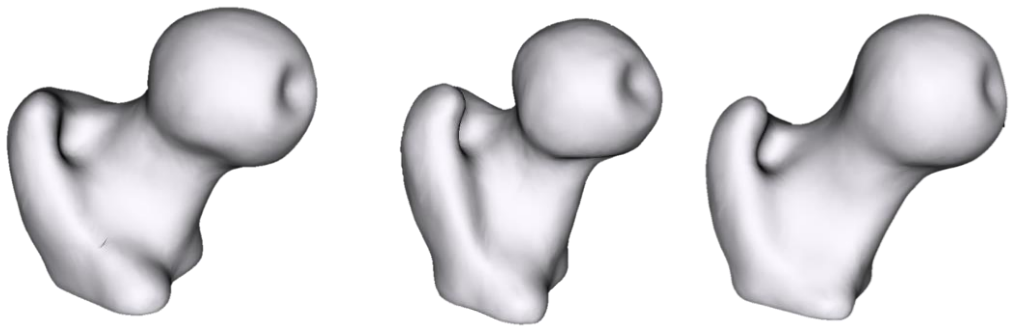

Figure 3.7: Samples from the SSM

problem is to introduce an explicit bias model which is added to the GPMM to slightly increase the flexibility of the model (Lüthi *et al.*, 2017).

The additional variance is modelled by adding a Gaussian kernel, with bandwidth parameter σ, denoted $k_g(x, y)$, to the covariance kernel sampled from the model, denoted as $k_{PDM}(x,\ y)$. A simple model used to reduce the bias of the model would make use of a Gaussian kernel with large bandwidth and define the new kernel as:

$$k_b(x, y) = k_{PDM}(x, y) + s_v \cdot I_{3x3} k_g(x, y) \quad (12)$$

A GP is built with the new augmented kernel, after which a low-rank approximation of the GP is calculated. A new GPMM is then constructed using this augmented low-rank GP.

3.4 Validation of SSM

Before the constructed SSM could be used for reconstruction purposes, the quality of the model was investigated. According to Davies (2002), three measures could be used to assess the quality of the model, namely compactness, specificity and generality.

Compactness measures the model's ability to capture variance within a shape population by using as few principal components as possible (Styner *et al.*, 2003). The compactness ability is determined by measuring the accumulative variance of the model and is defined by:

$$C(M) = \sum_{i=1}^{M} \lambda_i \quad (13)$$

where λ_i is the i^{th} eigenvalue and M are the number of principal components included in the model. The fewer principal components used to model a certain amount of variance, the more compact the model is.

Specificity describes the ability of the model to produce shape instances similar to the shapes within the training dataset. This characteristic is determined by randomly sampling uniformly distributed shape instances from the model and measuring the average distance or root-mean-square error between the sampled shapes and their closest match in the training dataset (Reyneke *et al.*, 2018). The distance between the generated shape and the best-matched training shape is then averaged over a large number of iterations. This measure is determined as a function of the number of principal components included in the model to produce random shapes and is denoted by:

$$S(M) = \frac{1}{n_s} \sum_{i=1}^{n_s} RMSE(R_i(M), t_{Ri}) \quad (14)$$

where R_i represents the randomly sampled shape, t_{Ri} describes the training shape that resembles the random sample the best and n_s is the number of iterations. The smaller the result of specificity the more specific the model (Davies, 2002). The standard error of $S(M)$ is defined as:

$$\sigma_{S(M)} = \frac{\sigma_{ss}}{\sqrt{n_s - 1}} \quad (15)$$

where σ_{ss} is the sample standard deviation of $S(M)$.

Generality quantifies the model's ability to produce new shape instances of the class of the object modelled (Heimann and Meinzer, 2009). This characteristic is estimated by using a leave-one-out cross-validation test where all but one of the training shapes is used to construct a model which is then fitted to the excluded shape. The distance between the model estimation and the excluded mesh is then used to determine the accuracy to which the reduced model can describe the excluded mesh. This process is repeated for each shape within the training dataset. Eventually, the average approximation error is obtained as a function of the number of principal components used to approximate the excluded mesh. The generality is defined as:

$$G(M) = \frac{1}{n_g} \sum_{i=1}^{n_g} RMSE(S_i(M), t_{Ei}) \quad (16)$$

where S_i represents the shape estimated by the model, t_{Ei} is the excluded shape and n_g is the number of shapes within the training dataset. As with specificity, the smaller the result of the generality measure the more general the model. The standard error of $G(M)$ is given by:

$$\sigma_{G(M)} = \frac{\sigma_{sg}}{\sqrt{n_g - 1}} \quad (17)$$

where σ_{sg} is the sample standard deviation of $G(M)$.

3.5 Results

Heimann and Meinzer (2009) suggested an 80:20 distribution between the training and the testing dataset. Thus, the SSM were constructed using 27 proximal femurs from the dataset, which leaves 6 proximal femurs to be used as the testing dataset. As mentioned in Section 3.4, three characteristic measures could be used to assess the quality of an SSM. The results of these measurements are shown in the following section.

3.5.1 Compactness

With compactness describing the cumulative variance of a model, Figure 3.8 describes the percentage of cumulative variance as a function of the number of modes (principal components) used. As seen in the figure, the first mode accounts for approximately 57.07% of the total shape variation and reaches a cumulative variance of just over 95% after 10 modes. Table 2 shows the variance captured by the first three principal components when the parameters have been set to $\pm 3\sqrt{\lambda_i}$ along with the percentage of variance these modes represent.

3.5.2 Specificity

Shapes sampled from the SMM should be similar to the shapes in the training dataset. The specificity measure along with the standard error was determined as a function of the model's number of modes and was computed over 100 iterations. Furthermore, the measure was determined by using the Root Mean Square (RMS) between the sampled shape and the model approximated shape. The results of the specificity measure can be seen in Figure 3.9. The specificity ranges from 1.38 to 2.02 mm.

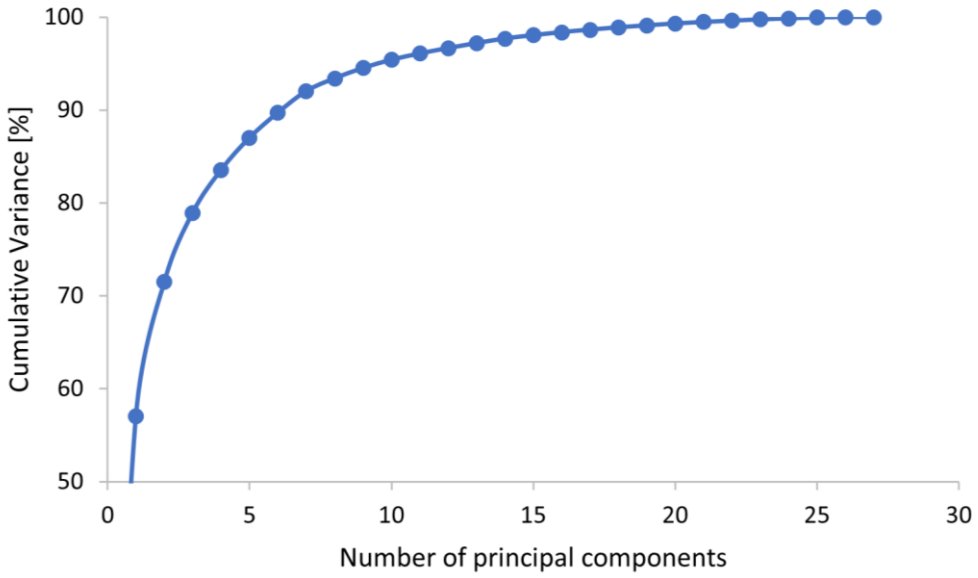

Figure 3.8: Compactness of the model

Table 2: First three modes of SMM

M	$-3\sqrt{\lambda_i}$	Mean	$+3\sqrt{\lambda_i}$	% Variance
1	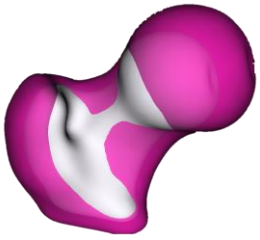	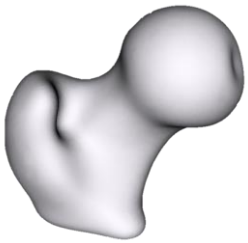	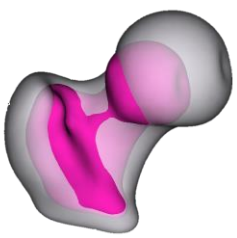	57.07
2	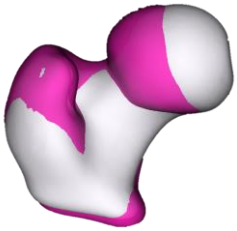	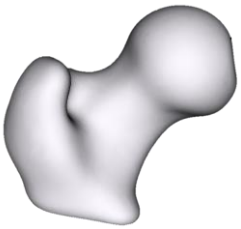	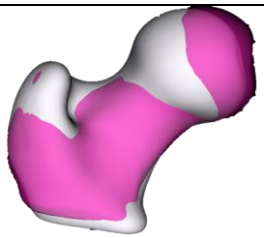	14.42
3	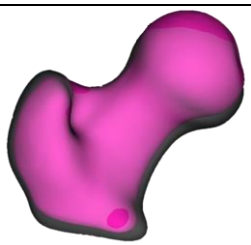	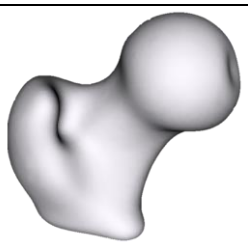	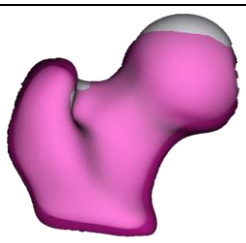	7.45

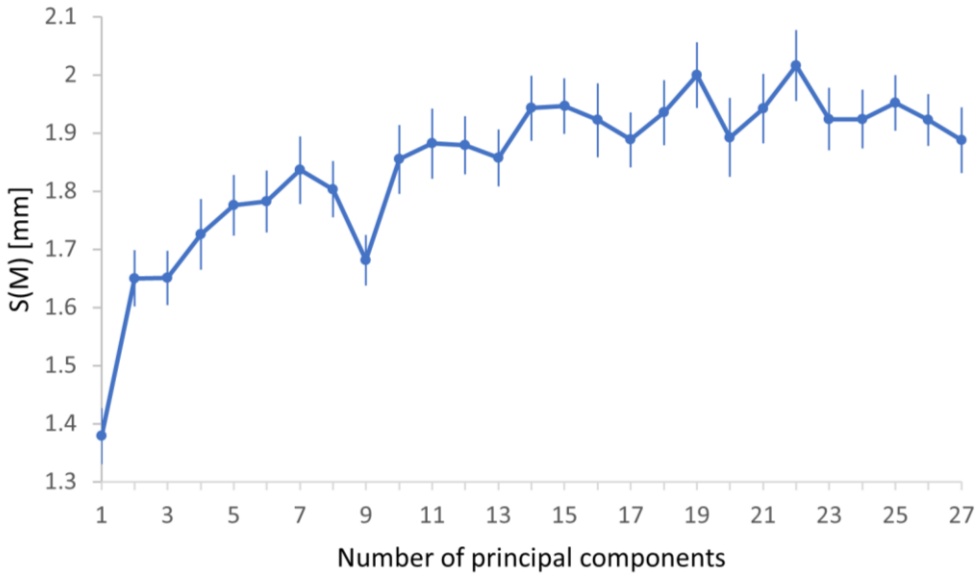

Figure 3.9: Specificity of the model

3.5.3 Generality

As mentioned in Section 3.4, the generality measure indicates how well an SSM can represent new instances of the same class. By using the leave-one-out cross-validation method the generalty was determined for each of the training shapes. The result displayed in Figure 3.10 is the generality and the standard error as a function of the number of modes in the model. The generality of this study ranges from 0.87 to 1.86 mm

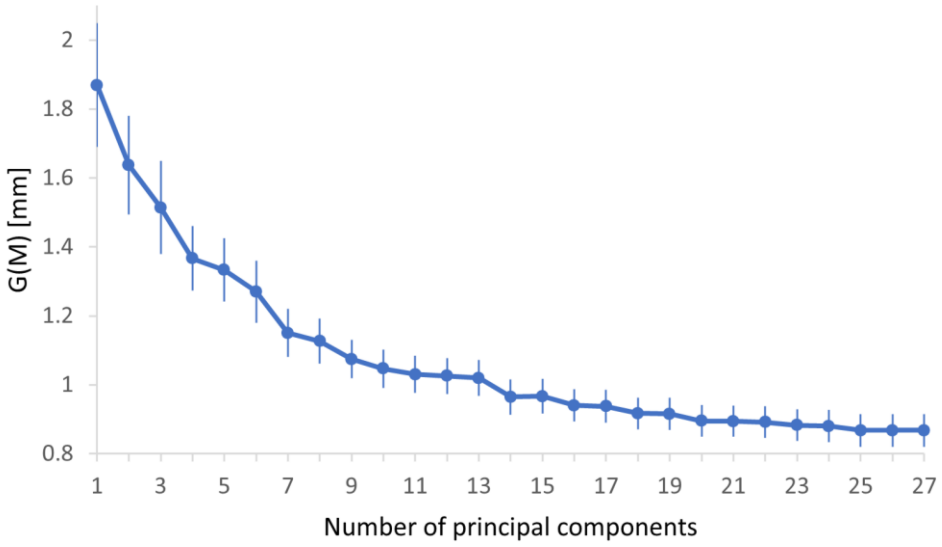

Figure 3.10: Generality of the model

3.6 Discussion

As seen in Table 2, a large amount of variation is captured by the first three modes of the model. Despite the large variation obtained in these modes, the shape instances obtained are still valid as the topology of the femur remains unchanged. Section 3.4 describes a model as being compact when it captures a large amount of variation with the minimum number of modes. Keeping this in mind, Figure 3.8 indicates that the model can describe approximately 90% of the shape variation with the first 6 modes which indicates that the models can be considered compact as relatively few modes were needed. Compared to the findings of other studies in the literature (Cerveri *et al.* (2019), Mutsvangwa *et al.* (2015), Salhi *et al.* (2020), etc), the compactness of this study seems coherent. Although approximately 95% of the variation could be explained by 10 modes, 15 modes will be utilised for the rest of the study which describes approximately 97% of the shape variations which is in the acceptable range and will still mitigate overfitting as described in (Heimann and Meinzer, 2009; Sarkalkan *et al.*, 2014).

Cerveri *et al.* (2019) constructed an SSM of the proximal femur from 30 training samples to compare registration methods. Similar to the current study, one of the methods that Cerveri *et al.* (2019) used to determine correspondence between training shapes was the non-rigid registration method. The specificity results from that study ranged from 1.38 to 2.36 mm. Table 3 shows the specificity obtained from other studies that used non-rigid registration methods to determine correspondence.

Table 3: Specificity measures of SSMs build from various structures

	Current Study	**Cerveri *et al.* (2019)**	**van der Merwe (2018)**		**Cerveri *et al.* (2019)**	**Mutsvangwa *et al.* (2015)**	**Salhi *et al.*, (2020)**
Bone Structure	Proximal Femur	Proximal femur	Distal Femur		Distal Femur	Scapula	Scapula
Gender	Neutral (n = 26)	Neutral (n = 30)	Male (n=32)	Female (n = 32)	Neutral (n = 28)	Neutral (n = 99)	Neutral
Specificity (mm)	1.38 to 2.02	1.38 to 2.36	0.92 to 1.75	0.71 to 1.38	1.20 to 2.43	1.40 to 1.60	1.22 to 1.74

As mentioned in Section 3.5.2, the specificity of the model in this study ranges from 1.38 to 2.02 mm with an average specificity of 1.85 mm. According to the studies listed in Table 3, the reported range for specificity is about 0.71 to 2.43 mm. Although it is difficult to compare the findings of the different studies in

the literature due to different sized datasets, anatomical structures and methods used, the specificity obtained from this study fall within the range of literature and the model produces instances that can be represented by the training data.

The generality obtained in this study ranges from 0.87 to 1.86 mm with an average generality of 1.08 mm, whereas the generality of Cerveri *et al.* (2019)'s model has a generality that ranges from 0.80 to 2.53 mm. Table 4 displays the generality of various other studies that used non-rigid registration to determine correspondence. Similar to the specificity, although difficult, the generability is compared to findings in the literature. These findings, as seen in Table 4, roughly range from 0.55 to 2.53 mm. Taking this into account, the generability of the model falls well within the range and can thus be considered a general model.

Table 4: Generality measures of SSMs build from various structures

	Current Study	**Cerveri *et al.* (2019)**	**van der Merwe (2018)**		**Cerveri *et al.* (2019)**	**Mutsvangwa *et al.* (2015)**	**Salhi *et al.*, (2020)**
Bone Structure	Proximal Femur	Proximal femur	Distal Femur		Distal Femur	Scapula	Scapula
Gender	Neutral (n = 26)	Neutral (n = 30)	Male (n=32)	Female (n = 32)	Neutral (n = 28)	Neutral (n = 99)	Neutral
Generality (mm)	0.87 to 1.86	0.80 to 2.53	0.67 to 1.09	0.55 to 0.87	1.16 to 1.75	1.10 to 1.90	0.79 to 1.64

As mentioned in Section 3.3.4, an advantage to modelling with Gaussian Processes is that kernels can be combined to define new kernels which allows for models to be constructed using deformations of multiple scales and varying smoothness. The constructed kernel, therefore, has an impact on the specificity and generality of the model. Thus by adjusting the kernels, the variation represented by the model could increase and will allow the shape model to be able to fit more unseen shapes. This means that the generality of the models would improve but it will decrease the specificity of the model proportionally. If the distance over which the deformations are correlated is chosen as too small or too large, it could lead to unrealistic deformations of the shape model and will lead to very high specificity.

Another factor that could have an impact on the specificity and generality of the model is the size of the training dataset. There is little literature available that indicates the amount of data needed to construct a shape model, but increasing the number of training shapes will increase the amount of variance that the model captures and ultimately improve the generality of the model (van der Merwe *et al*., 2018).

Unfortunately, there is little literature available that specifies the clinical performance requirements needed to perform 2D/3D registration with an SSM. The model's quality was thus based on the comparison of the validation results to other similar studies in the literature. Based on these results, the results seem promising and could be used for the reconstruction of 3D models from 2D images.

Chapter 4

Digitally reconstructed radiograph

To perform 2D/3D registration between a shape model and patient data, 2D radiographs of the patient are needed. However, from the dataset obtained, the only data available were the 3D CT scans of each patient. Therefore, a 2D x-ray needs to be generated to be used as the input image into the algorithm explained in Chapter 5. This section will explain how the 2D image is projected from 3D volumetric data.

4.1 Overview

According to Kim *et al.* (2015), Computed Tomography (CT) is an essential tool for directly visualizing human anatomy in medical imaging. In many research studies, such as the design of a scanner or in this case the development of a 2D/3D reconstruction algorithm, the ability to obtain simulated x-ray images that is realistic and accurate is highly desired. This provides a cost-effective way to obtain data without performing real experiments (Jia *et al.*, 2012).

The projection of Digitally Reconstructed Radiographs (DRR) is a rendering technique which produces a synthetic x-ray image created from a 3D volumetric model or CT volume by simulating the x-ray imaging process (Reyneke *et al.*, 2018). A DRR involves ray tracing through a 3D volume based on projection geometries as well as the numeric integration of the image data along the ray paths.

Generally, there are two types of volume projection used for DRR generation, namely ray casting and voxel projection (Mu, 2016). Ray casting is a technique that computes the line integral along a beam, which emerges from the centre-of-projection (COP), for each pixel. The line integral consists of the CT values on the path of the beam. The voxel projection method iterates over the voxel volume accumulating each voxel projection in such a way that the DRR can be considered as a sum of all the voxel projections (Birkfellner *et al.* 2005).

In voxel projection, the voxels are processed in storage order, which allows for faster traversal of the dataset and the resolution of the resulting DRR is better than that of the ray casting method since no interpolation is required (Wang *et al*. 2002). On the other hand, ray casting has two significant advantages. The first one is that the method is trivially parallelizable, meaning it is not necessary to manage concurrent write accesses to the detector plane. The second advantage is that the normalization of the line integrals with respect to the corresponding distance “travelled” of the ray through the volume is significantly simpler than that of the

voxel projection method (Graetz, 2016). A limitation of ray-casting is that this approach can lead to a high computational cost when a large sampling rate is used along the rays.

An essential component of simulating an x-ray imaging process is a sufficient sampling and accumulation strategy for integrating and evaluating the values from the CT voxels (Graetz, 2016). Therefore, ray casting will be the method used to produce a DRR. An example of the ray-casting method is illustrated in Figure 4.1

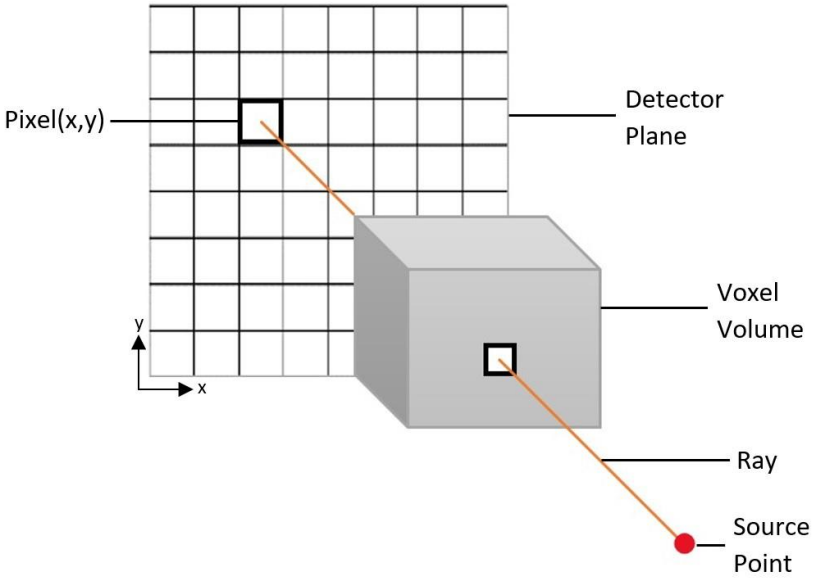

Figure 4.1: Illustration of the ray-casting process

4.2 Siddon-Jacobs algorithm

Ray casting, the method most commonly used to fulfil DRR generation, is derived from the Beer-Lambert Law. This law states that, given a monochromatic x-ray beam, the intensity of a ray drops exponentially as the ray travels through a volume (Baur *et al.*, 2019). To determine the intensity of a pixel on the detector plane, each CT voxel encountered on the ray path between the source and the detector pixel is evaluated. When evaluating a voxel, the "travelled" distance of the ray as well as the corresponding linear attenuation coefficient (LAC) is considered. Therefore, the x-ray signal intensity captured by the detector plane can be written as:

$$I = \int I_0(E) * \exp\left(-\int_L \mu_{LAC}(E,r)\, dl\right) dE \qquad (18)$$

where $I_0(E)$ is the incident x-ray intensity and energy spectrum, L is the path from the x-ray source to the detector plane pixel and $\mu_{LAC}(E,r)$ is the position and energy-dependent LAC of the volume the ray passed through (Folkerts, 2015). The main objective of a DRR algorithm is to evaluate the integral described in Equation 18 over the ray paths existing between the detector plane and the x-ray source.

4.2.1 Integration problem

The formulation in Equation 18 can be simplified by modelling the x-ray source as monoenergetic (Folkerts, 2015). This can be accomplished by using a spectrum with a constant intensity value $I_0(E) = I_0$ and by replacing the energy-dependant LAC with coefficients at effective energy $\mu_{LAC}(E,r) = \mu_{LAC}(E_{eff},r) = \mu_{LAC}(r)$. A simpler integral can be seen in Equation 19.

$$I = I_0 * \exp\left(-\int_L \mu_{LAC}(r)dl\right) \quad (19)$$

Lastly the integral is discretized along the ray paths between the source and the detector plane to produce a voxelized representation:

$$I = I_0 * \exp\left(-\sum_n \mu_{LACa} l_{a,b}\right) \quad (20)$$

where a represents a specific voxel, b represents a ray beam, l represents the intersection length and μ_{LAC} is the LAC. The corresponding attenuation coefficient for the Hounsfield unit relative to the attenuation coefficient of water at a specific CT energy of a voxel is determined by:

$$h_a = \frac{(\mu_{LACa} - \mu_{LACw}) \times 10^3}{\mu_{LACw}} \quad (21)$$

where h_a is the Hounsfield unit of the CT voxel, μ_{LACw} is the attenuation coefficient of water and μ_{LACa} is the current voxel's attenuation coefficient (LAC).

4.2.2 Sampling technique

A commonly used technique for generating DRRs in medical physics is the method proposed by Siddon (1985), known as the Siddon algorithm. This algorithm performs volume ray casting by describing the radiological path through a 3D volume as:

$$d = \sum_i \sum_j \sum_k l(i,j,k)\rho(i,j,k) \quad (22)$$

by denoting the voxel intensity value as $\rho(i,j,k)$ and the length contained by that voxel as $l(i,j,k)$. Prior to the reconstruction, the Siddon algorithm computes an array of parametric values which correspond to the intersections of the ray with the planes for each axis. Each element within the array represents an intersection of the ray with the corresponding plane (Siddon, 1985). These arrays are then merged into a combined array and arranged in ascending order of distances between the source and the intersected plane. Therefore, during dose calculation, the radiological path of a ray through a 3D volume can just be extracted from the merged array (Xiao *et al*. 2012).

The problem with this algorithm is that it requires a large amount of memory space to be able to store a merged array for each ray moving through the volume. Jacobs *et al.* (1998) proposed to improve the Siddon algorithm by significantly reducing the time spent computing the array of parametric values. This improved algorithm is known as the Siddon-Jacobs algorithm. This algorithm aims to calculate the intersections of the ray with the CT volume by using a set of geometrical relationships with the entry and exit points of the ray with the volume (Alvarez-Gomez *et al.* 2021).

In this algorithm, the CT data is modelled as voxels with equally spaced distances along each axis (Folkerts, 2015). According to Siddon (1985), rather than the voxels being considered independent elements, they are considered as intersections between the orthogonal sets of equally spaced planes. Figure 4.2 illustrated this concept in a two-dimensional case.

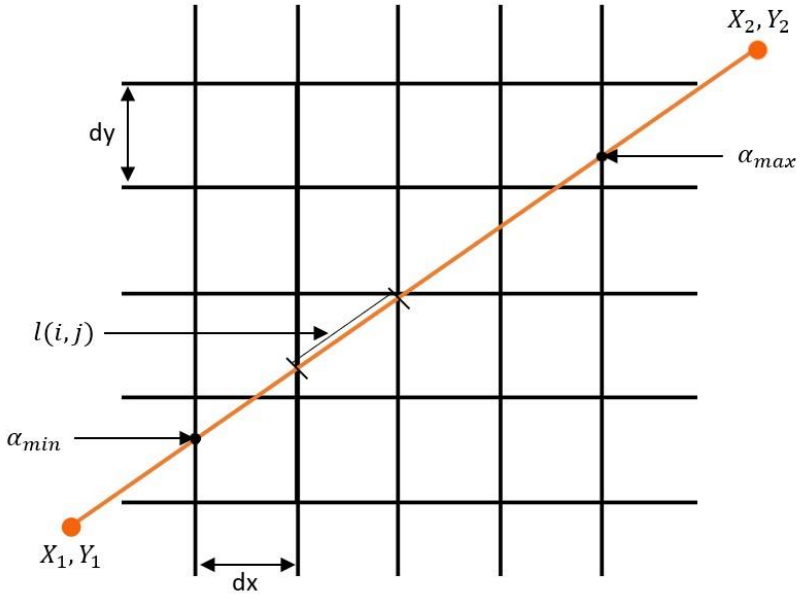

Figure 4.2: Pixels considered as intersections between orthogonal sets of equally spaced, parallel lines

The study implemented the Siddon-Jacobs algorithm to render a DRR from a CT voxel volume. Equation 22 is evaluated by following the ray through the voxel volume. Thus, the parametrical representation of the ray from point 1 to point 2 is written as:

$$p_{12} = \begin{cases} X(\alpha) = X_{pt1} + \alpha\left(X_{pt2} - X_{pt1}\right) \\ Y(\alpha) = Y_{pt1} + \alpha\left(Y_{pt2} - Y_{pt1}\right) \\ Z(\alpha) = Z_{pt1} + \alpha\left(Z_{pt2} - Z_{pt1}\right) \end{cases} \quad (23)$$

where α is the parametric value which ranges between 0 and 1, with point one being 0 and point two being 1 (Siddon, 1985). Throughout the rest of the section, it is assumed that $p_1 \neq p_2$. Considering a CT array of $(N_x - 1, N_y - 1, N_z - 1)$ voxels, the orthogonal sets of equally spaced, parallel planes displayed in Figure 4.2 can be written as:

$$X_p(i) = X_p(1) + (i-1)d_x \qquad (i = 1, \dots, N_x) \quad (24)$$

$$Y_p(j) = Y_p(1) + (j-1)d_y \qquad (j = 1, \dots, N_y) \quad (25)$$

$$Z_p(k) = Z_p(1) + (k-1)d_z \qquad (k = 1, \dots, N_z) \quad (26)$$

where d_x , d_y , d_z represents the distance between the planes in the x, y and z axis respectively. To determine the path of the ray, the entry, $\alpha = \alpha_{min}$, and exit point, $\alpha = \alpha_{max}$, of the ray with the volume needs to be determined (Jacobs *et al.*, 1998). The parametric values for each plane are determined by:

$$\alpha_x(i) = \frac{[X_p(i) - X_{pt1}]}{X_{pt2} - X_{pt1}} \quad (27)$$

$$\alpha_y(j) = \frac{[Y_p(j) - Y_{pt1}]}{Y_{pt2} - Y_{pt1}} \quad (28)$$

$$\alpha_z(k) = \frac{[Z_p(j) - Z_{pt1}]}{Z_{pt2} - Z_{pt1}} \quad (29)$$

The entry and exit points are determined when the ray intersects the sides of the volume. Equations 24 to 29 can now be used to determine the parametric values at the entry and exit points of the ray:

$$\alpha_{min} = max\{0, max[\alpha_x(1), \alpha_x(N_x)], min\left[\alpha_y(1), \alpha_y(N_y)\right], min[\alpha_z(1), \alpha_z(N_z)]\} \quad (30)$$

$$\alpha_{max} = min\{1, max[\alpha_x(1), \alpha_x(N_x)], min\left[\alpha_y(1), \alpha_y(N_y)\right], min[\alpha_z(1), \alpha_z(N_z)]\} \quad (31)$$

From all the planes the ray intersects, only certain planes have parametric values that fall within the range $(\alpha_{min}, \alpha_{max})$. The range of the indices which correspond to these certain planes is determined by:

$$\text{if } (X_{pt2} - X_{pt1}) \geq 0,$$

$$i_{min} = N_x - \frac{[X_p(N_x) - \alpha_{min}(X_{pt2} - X_{pt1}) - X_{pt1}]}{d_x} \quad (32)$$

$$i_{max} = 1 + \frac{[X_{pt1} + \alpha_{max}(X_{pt2} - X_{pt1}) - X_p(1)]}{d_x} \quad (33)$$

$$\text{if } (X_{pt2} - X_{pt1}) \leq 0,$$

$$i_{min} = N_x - \frac{[X_p(N_x) - \alpha_{max}(X_{pt2} - X_{pt1}) - X_{pt1}]}{d_x} \quad (34)$$

$$i_{max} = 1 + \frac{[X_{pt1} + \alpha_{min}(X_{pt2} - X_{pt1}) - X_p(1)]}{d_x} \quad (35)$$

Similar expressions are used to determine j_{min}, j_{max}, k_{min} and k_{max}. These indices can then be used to determine how many planes were intersected by the ray while moving through the voxel volume (Siddon, 1985). As the ray moves through the volume, the index incremental values need to be updated, this is achieved using Equations 36 to 38:

$$i_{step} = \begin{cases} 1 & \text{if } X_{pt1} < X_{pt2} \\ -1 & \text{else} \end{cases} \quad (36)$$

$$j_{step} = \begin{cases} 1 & \text{if } Y_{pt1} < Y_{pt2} \\ -1 & \text{else} \end{cases} \quad (37)$$

$$k_{step} = \begin{cases} 1 & \text{if } Z_{pt1} < Z_{pt2} \\ -1 & \text{else} \end{cases} \quad (38)$$

As the ray moves through the voxel volume, the parametric values along with the indices need to be updated according to which plane is crossed. After initializing d to 0, and the current parametric value α_{curr} to α_{min}, the radiological path can be calculated. The ray is iterated until $\alpha_{curr} = \alpha_{max}$. The pseudocode of the algorithm calculating the radiological path is shown in Figure 4.3.

```
/* Initialization                                                    */
    d = 0                                   /*Initialized radiological path*/
    α_curr = α_min                          /*Parametric value of the ray entry point*/
/* Radiological path                                                 */
    while α_curr < α_max do
        if (min(α_x, α_y, α_z) = α_x) then
            l(i,j,k) = (α_x − α_curr)       /*Determine ray length inside voxel*/
            i = i + i_step                  /*Increment index in x-direction*/
            α_curr = α_x                    /*Update the current parametric value*/
            α_x = α_x + d_x / |X_pt2 − X_pt1|   /*Update parametric value of x-direction*/
        else if (min(α_x, α_y, α_z) = α_y) then
            l(i,j,k) = (α_y − α_curr)       /*Determine ray length inside voxel*/
            j = j + j_step                  /*Increment index in y-direction*/
            α_curr = α_y                    /*Update the current parametric value*/
            α_y = α_y + d_y / |Y_pt2 − Y_pt1|   /*Update parametric value of y-direction*/
        else
            l(i,j,k) = (α_z − α_curr)       /*Determine ray length inside voxel*/
            k = k + k_step                  /*Increment index in z-direction*/
            α_curr = α_z                    /*Update the current parametric value*/
            α_z = α_z + d_z / |Z_pt2 − Z_pt1|   /*Update parametric value of z-direction*/
        end if
        d = d + l(i,j,k)ρ(i,j,k)            /*Calculate the radiological path*/
    end while
```

Figure 4.3: Radiological path calculation

Figure 4.4: Resulting DRR

4.3 Results

The resulting DRR images generated in this study consist of 512x512 pixels with a grayscale range of {0-255}. An example of a DRR generated in this study is shown in Figure 4.4, whereas Figure 4.5 shows an example of the CT scans used to generate the DRR.

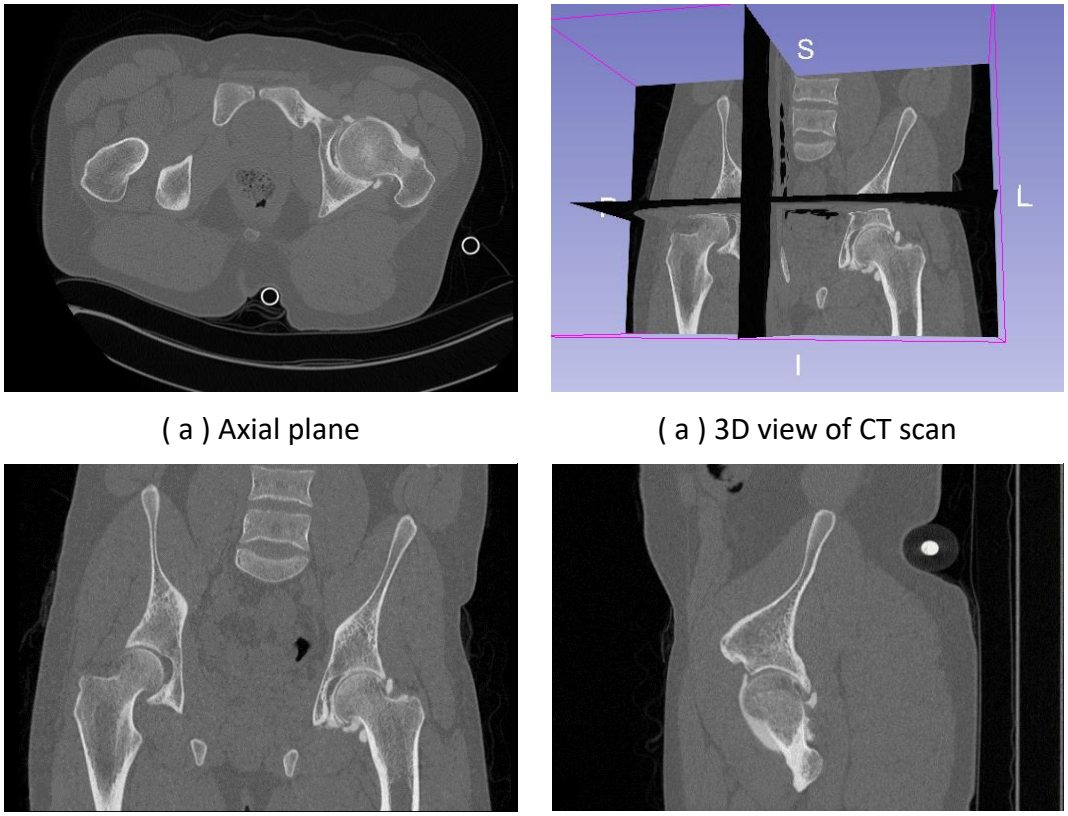

(a) Axial plane

(a) 3D view of CT scan

(c) Coronal plane

(d) Sagittal plane

Figure 4.5: Example of the CT image used for DRR rendering

4.4 Discussion

Usually, to verify a DRR it is compared to a ground truth x-ray image of a patient and the pixel-wise absolute difference between the two images is computed (Alvarez-Gomez *et al.*, 2021; Moore *et al.* 2011; Staub & Murphy, 2013). Unfortunately, no x-ray images were available in the obtained dataset, so the DRR could not be validated traditionally. Thus to validate the results, the resulting DRR were visually compared to a clinical x-ray image obtained from Valera *et al.* (2016) and a DRR generated by Bizdikian *et al.* (2018). These comparisons are displayed in Figure 4.6 and Figure 4.7 respectively.

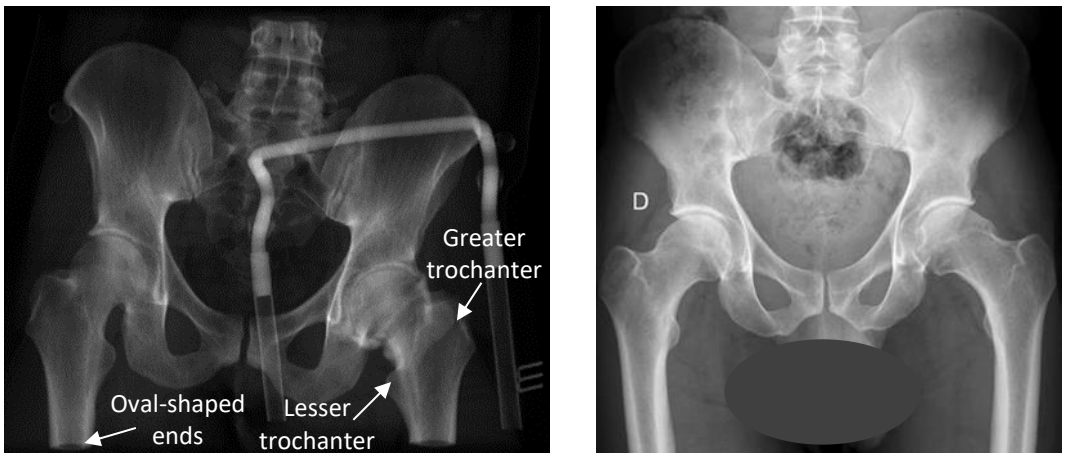

(a) Resulting DRR (b) AP pelvis x-ray

Figure 4.6: Resulting DRR compared to a clinical x-ray. X-ray image obtained with permission from Valera *et al*. (2016)

Upon visual inspection of the images in Figure 4.6, it can be seen that the generated DRR closely resembles the clinical AP x-ray, as the most apparent features have been reproduced clearly. Important anatomical landmarks such as the greater and lesser trochanter can easily be identified on both images, but the DRR has a lower contrast of bony structures which could lead to a loss of finer detail displayed in a clinical x-ray image. According to Killoran *et al.* (2001) this is due to CT acquisition and radiographic exposure using different amounts of x-ray energy which significantly affects the relationship between the observed contrast of various density structures. Another difference between the two images is that the oval-shaped ends on the femoral shaft make it appear to be cut off in the DRR. This is due to the clipping of the CT scan volume during the perspective projection which is why it does not appear on the x-ray.

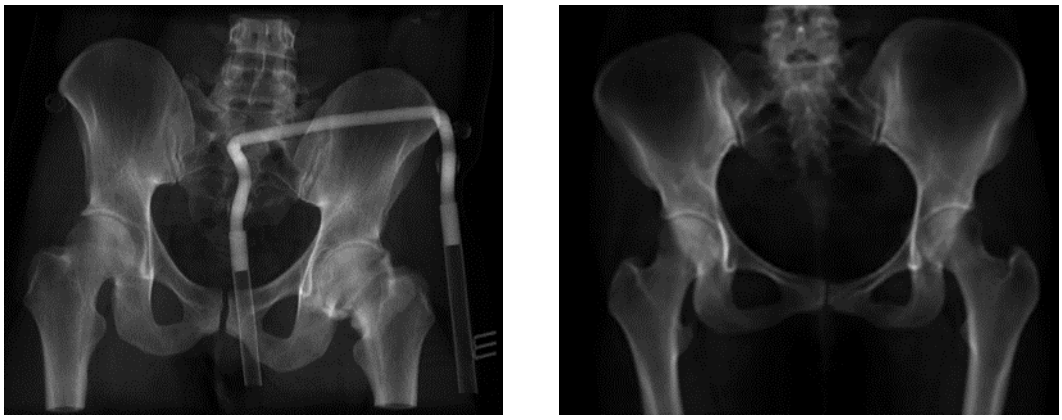

(a) DRR from current study (b) DRR generated by Bizdikian *et al*

Figure 4.7: Resulting DRR compared to a DRR from literature ((b) obtained with permission from Bizdikian *et al.* (2018))

In a study by Bizdikian *et al.* (2018) where digitally reconstructed radiographs were produced to determine a valid and reliable method for measuring the neck-shaft angle, the DRR in Figure 4.7(b) was generated. The only clear difference between the two generated DRR's are the femur shafts which do not appear cut off in the DRR generated by Bizdikian *et al.* (2018). This could be due to the different rendering techniques used since Bizdikian *et al.* (2018) used cylindrical projection and the current study used perspective projection. Another possibility would be that the authors cropped the reconstructed radiograph to remove the oval-shaped ends from the image. The generated DRR from the literature was deemed sufficient to be used for neck-shaft measurements and 3D reconstruction. Since the DRR generated obtained in the current study are similar to the DRR constructed in literature, the resulting DRR seems promising and sufficient to be used as an input image to the reconstruction algorithm.

Chapter 5

2D to 3D reconstruction using a statistical shape model

Considering the Statistical Shape Model obtained in Chapter 3, this chapter will describe how the model is fitted to unseen image data and investigate how accurately the model can reconstruct a patient-specific shape from 2D images through 2D/3D registration. In Section 5.1 an overview of the process is given and Section 5.2 explains how the contour from the patient x-ray and the synthesized image are extracted to be compared in the registration algorithm. The implementation of the registration process is discussed in Section 5.3 and lastly, Sections 5.4 to Section 5.6 will evaluate the reconstructed model and discuss the results.

5.1 Overview

Three-dimensional reconstructed patient-specific anatomical structures have become a valuable instrument within the orthopaedic field. These reconstructions can be used for many applications such as the detection of pathologies of the bone structure or using the measurements obtained from the bone geometry for implant design, post-operative evaluation or in surgical planning (Reyneke *et al.*, 2018).

As mentioned in Section 1.2, 3D patient-specific shape models can be obtained from two-dimensional images by using two-dimensional-to-three-dimensional (2D/3D) registration. Through the use of deformable models, the registration process can be accomplished, as the models contain assumptions and prior knowledge regarding the anatomical structure. The registration algorithm is an iterative process where the parameters of the models are adjusted with each observation according to information gathered from the 2D images. The updated parameters are then used to manipulate the model to match the target structure (Thusini *et al.*, 2020).

In this study, the reconstruction problem is framed as model fitting based on Bayesian Inference, which is an approach to parameter estimation and data analysis based on Bayes' theorem. According to Van de Schoot *et al.* (2021), the Bayesian inference typically consists of three main steps, namely:

1. Use a *prior distribution* to capture the available information about given parameters in an SSM.

2. Determine a *likelihood function* which measures the compatibility of a shape model instance with the observed data.

3. Combine the likelihood function and prior distribution using Bayes' theorem in the form of the *posterior distribution.*

The posterior distribution displays the updated knowledge regarding the model parameters which balances the observed data with prior knowledge (Schönborn *et al.* 2020). Applying Bayesian inference to the posterior distribution is quite difficult to do in practice as the algorithm requires a normalization step that renders most problems intractable. The normalization process requires that the prior and the likelihood be integrated over the model space. This results in a marginal likelihood that provides valuable information regarding the suitability of the model but is very expensive to calculate and only a few models result in a closed-form solution (Schönborn *et al.*, 2020).

A strategy to deal with the missing closed-form solution is to use a Markov Chain Monte Carlo (MCMC) based approach where an approximation to the posterior distribution is calculated rather than solving the posterior distribution. All MCMC-type algorithms draw samples from the Markov Chain, where the target distribution is the equilibrium distribution (Schönborn *et al.*, 2020). This study makes use of a Metropolis-Hastings algorithm where samples are drawn from a proposal distribution. These samples are then accepted or rejected based on their probability under the posterior distribution to build its Markov Chain.

By using the Metropolis-Hastings algorithm along with a shape prior model obtained in Chapter 3, the reconstruction problem is approached through analysis by synthesis similar to Schönborn *et al.* (2017). The reconstruction is accomplished by synthesizing contours from the model and comparing the synthesized contours to the annotated contours from the input x-ray image. Figure 5.1 gives an overview of the 2D/3D reconstruction algorithm used throughout the study.

5.2 Contour extraction

As previously mentioned, the 2D/3D registration is accomplished by comparing the x-ray contours with the synthesized contours of the shape model. Therefore, the registration algorithm requires two things, namely

1. An extracted contour from the input x-ray image obtained in Section 4

2. A synthetic contour generated by projecting the SSM obtained in Section 3

According to Tariq and Burney (2012), contour extraction generally follows the process of edge detection, where the pixels in an image that experience a sharp

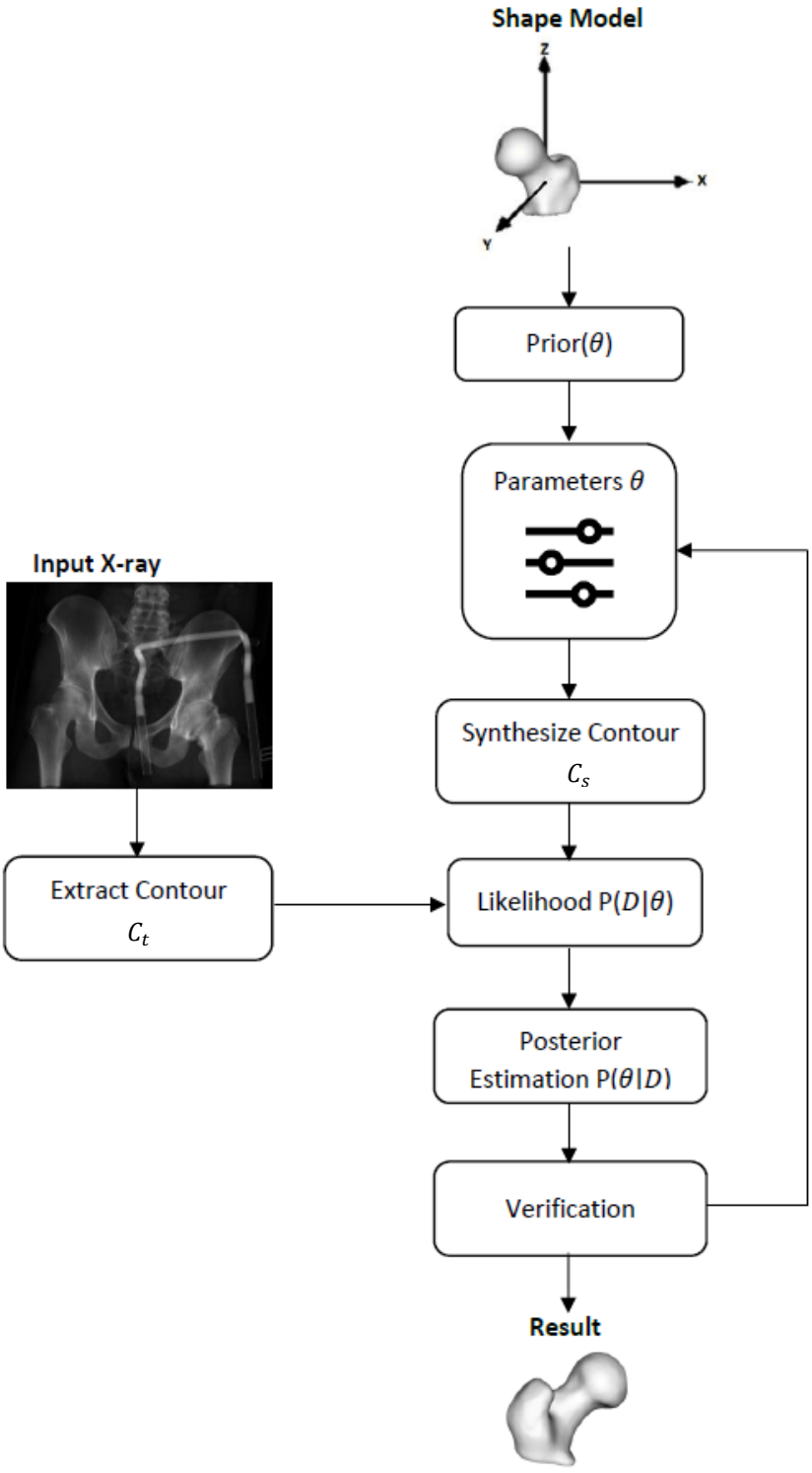

Figure 5.1: Analysis by synthesis approach for 2D/3D Reconstruction

change in intensity are identified. A popular edge detection technique is the Canny Edge Detection algorithm developed by Canny (1986). Compared to other edge

detection algorithms like the Sobel and Prewitt algorithms, the Canny edge detection produces finer and smoother edges even though the computational complexity is a bit higher (Katiyar and Arun, 2014). Thus, the Canny edge algorithm will be used to identify the contours in the x-ray image and the projected shape image.

5.2.1 Canny-edge detection algorithm

According to Xu *et al.* (2017), the Canny Edge Detection Algorithm consists of 4 steps:

1. Noise reduction – The edge detection algorithm is highly sensitive to noise, thus an image convolution technique using a Gaussian kernel is used to remove the noise from an image. The Gaussian kernel is given by:

$$G_\sigma = \frac{1}{2\pi\sigma^2} \times e^{-\frac{(x^2+y^2)}{2\sigma^2}} \quad (39)$$

2. Gradient calculation – This step detects the image gradient and direction across the smoothened image by applying a Sobel operator in the horizontal and vertical directions to determine the first derivatives in each direction. The magnitude, G_M, and the slope, θ_G, of the gradient, can then be calculated using:

$$G_M = \sqrt{{G_x}^2 + {G_y}^2} \quad (40)$$

$$\theta_G = \tan^{-1}\left(\frac{G_y}{G_x}\right) \quad (41)$$

3. Non-maximum suppression – After the gradient magnitude and slope have been calculated, the image is examined to remove any pixels that do not constitute the edge. This is accomplished by finding the pixels with a maximum value in the edge directions.

4. Hysteresis thresholding – This step determines which of the edges obtained in the non-maximum suppression stage are indeed edges and which is considered noise. Two threshold values, namely an upper and a lower threshold, are needed to determine this. The edges with a gradient above the upper threshold are immediately considered as edges, while the edges with gradients lower than the lower threshold are disregarded. The edges which lie between the upper and the lower threshold are classified based on their connectivity. The edges connected to the “strong-edged” pixels are kept as edges, otherwise, the edges are disregarded.

Due to the popularity of the Canny-Edge-Detection algorithm, OpenCV has already implemented the algorithm in the `cv2.Canny` function. OpenCV (Open Source Computer Vision Library) is an open-source library that includes a variety of computer vision algorithms.

5.2.2 X-ray contour identification and extraction

The algorithm that extracts the femur contour from the input x-ray image is executed in the Python environment and uses algorithms from the OpenCV library to process, identify and extract the contour. The input image is a synthetic anteroposterior hip radiograph, but this study only focuses on the left proximal femur. Thus, the image can be resized to the region of interest. Next, the image needs to be processed to enhance the contour of the femur. A combination of adaptive threshold and morphological transformation techniques was used for image preprocessing.

Adaptive thresholding is a segmentation technique that determines the threshold of a pixel based on a small set of neighbouring pixels. Once the threshold of the image pixels has been determined the segmentation is performed. The output of the adaptive thresholding method is a binary image where the foreground is represented by white pixels. The morphological transformations are simple operations applied to binary or grayscale images. More precisely, these operations are applied to the shapes and structures within the image. These operations are used to close gaps between objects and remove the noise from the image.

The Canny Edge Detection function described in Section 5.2.1 can now be applied to the processed image. This function, which takes the processed image, upper threshold and lower threshold as inputs, is used to identify all possible contours within the image. In this case, the upper and lower threshold were chosen as 30 and 180, respectively. Once the contours are identified, the function returns a binary image where the contours are indicated with white pixels. These identified contours are extracted by using the `cv2.findContours` function with input parameters `cv2.RETR_EXTERNAL` and `CHAIN_APPROX_NONE` from the OpenCV library. The extracted contour points are stored according to the contour approximation methods. In this case, all the boundary points detected are stored to ensure that the contour of the femur remains accurate.

Because the proximal femur is specified as the region of interest, the contour of the femur will be the largest contour extracted from the image. Thus, to isolate the contour points of the femur, the contour with the largest area is extracted. Lastly, these contour points are imported into scalismo to be compared to the synthetic contour points. The output of the `cv2.Canny` and the `cv2.findContours` functions can be seen in Figure 5.2

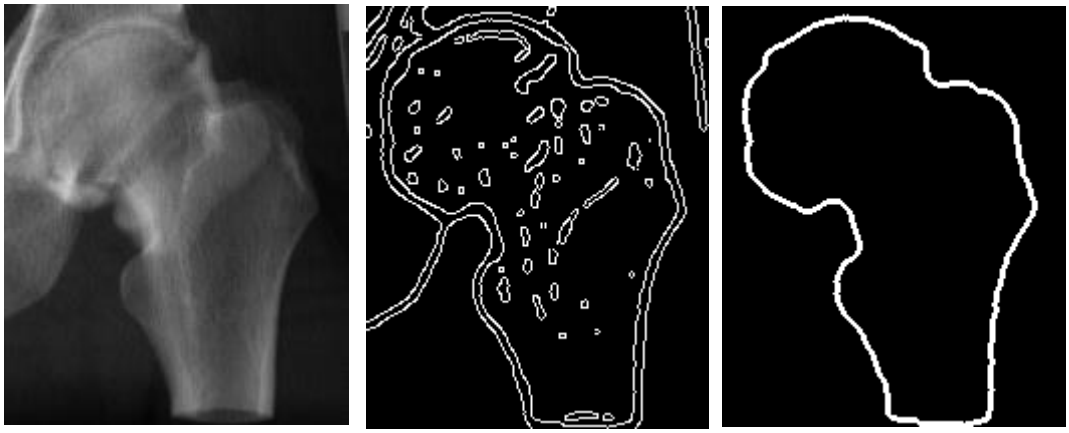

(a) Region of interest (b) Result of Canny Edge (c) Extracted contour

Figure 5.2: Canny-edge detection

5.2.3 Synthetic contour generation and extraction

Since 2D and 3D images cannot be registered directly, a synthetic 2D image of the SSM contour needs to be generated (Mu, 2016). These synthetic 2D images will then be registered to the x-ray images. The algorithm for extracting synthetic contours consists of three steps, where the first two steps are executed in a scalismo environment and the last step in python. First, the current 3D shape instance of the femur is converted to a binary image. This binary image is a continuous 3D scalar image defined on 3D real space. Since the mesh is a closed surface, the points inside the mesh surface will have a value of one and points outside the surface will have a value of zero.

The second step consists of rendering a 2D image from the 3D mesh. A technique similar to the one described in Chapter 4 is used in the rendering process. During this process, a ray is cast from a source point to each pixel on the 2D detector plane. Following the ray through the 3D space, a value of 1 is assigned to the pixel if the object is visible at that point, otherwise, a value of zero is assigned. The resultant rendered image will be a silhouette of the current femur shape. An example of the rendering process is displayed in Figure 5.3.

Lastly, the contour of the silhouette needs to be extracted. Since the image is a binary image with a silhouette of the shape, a Sobel operator is applied to the image to identify the contour and then the `cv2.findContours` function is used to extract the contour points. The points array is then imported to scalismo.

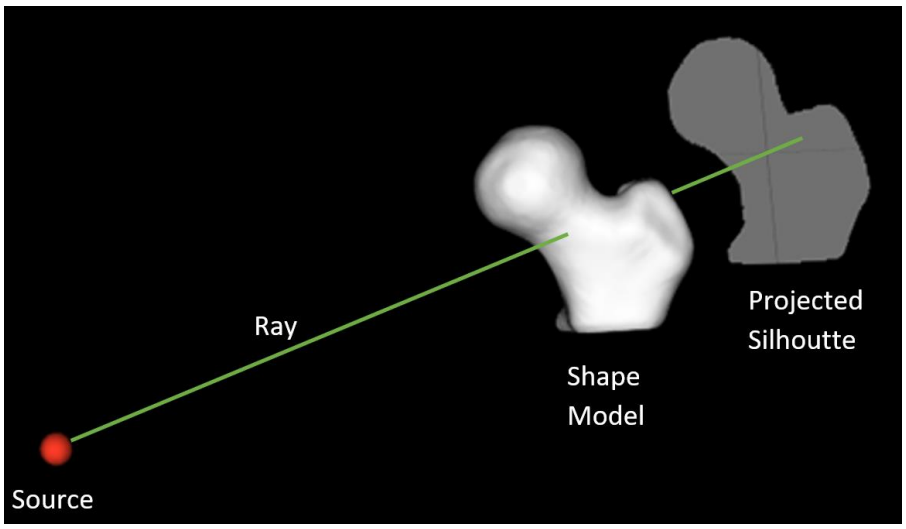

Figure 5.3: Synthetic DRR rendering

5.3 Implementation of the fitting algorithm

Section 5.2.3 explains how to generate a contour from a proximal femur shape model. This allows for model fitting by using sampling methods. The proposed algorithm is based on Bayesian inference. This is accomplished by using the SSM shape model as a prior and by using MCMC sampling methods for inference. Chapter 3 showed that low-rank decompositions allowed a GP to be treated as a parametric model, where an instance of the model is described by a set of parameters (θ). In the case of model fitting, the model instance is a deformation field.

In the Bayesian setting, the focus is on the posterior distribution which is denoted by:

$$P(\theta|D) = \frac{P(D|\theta)P(\theta)}{P(D)} \qquad (42)$$

where D is the data observed, $P(D|\theta)$ is the data likelihood and $P(\theta)$ is the prior distribution. This leads to a distribution that is defined over the model parameters, which is adapted according to the observed data as mentioned in Section 5.1.

The normalizing factor, $P(D)$, is the distribution over the observed data, which is not specified. Thus, the normalizing factor can be replaced with a factorized joint distribution and by marginalizing the parameters (Lüthi, 2020). The posterior distribution can then be written as:

$$P(\theta|D) = \frac{P(D|\theta)P(\theta)}{\int P(\theta|D)P(D)d\theta} \quad (43)$$

While likelihood and prior are relatively easy to handle, the normalization constant requires integration over the entire model space for the shape parameters, which leads to a posterior distribution that is computationally expensive (Schönborn *et al.*, 2020). MCMC is a popular technique used to perform approximate inference on posterior models that are deemed intractable (Schönborn *et al.,* 2017). The MCMC approach draws samples from the Markov Chain and uses an acceptance probability to determine whether to continue with a new proposed sample or rather use the current sample. The acceptance probability provides a solution to the integration problem. This is illustrated by computing the acceptance ratio over the normalized posterior:

$$Acceptance\ ratio = \frac{P(\theta'|D)}{P(\theta|D)} = \frac{\frac{P(D|\theta')P(\theta')}{P(D)}}{\frac{P(D|\theta)P(\theta)}{P(D)}} = \frac{P(D|\theta')P(\theta')}{P(D|\theta)P(\theta)} \quad (44)$$

As seen in Equation 44, the normalizing factor gets eliminated. This means that the acceptance ratio of the normalized posterior is equivalent to that of the unnormalized posterior. Since the normalizing factor is eliminated, the inference can be limited to evaluations of the unnormalized posterior distribution:

$$P(\theta|D) \propto P(D|\theta)P(\theta) \quad (45)$$

The inference problem is approached by using the Metropolis-Hatings algorithm. The MH algorithm aims to draw samples from a proposal distribution $Q(\theta'|\theta)$, to ultimately be able to draw samples from the posterior distribution.

Considering the information given above, a proposal generator, likelihood function and a prior distribution need to be determined in order to build the Markov chain. The following sections will explain how these functions are defined.

5.3.1 Metropolis-Hastings algorithm

Given that unnormalized distributions can be evaluated in a point-wise manner, this algorithm allows sampling from any distribution. It follows a propose-and-verify architecture, where each iteration is divided into proposal and verification stages (Thusini *et al.*, 2020). Given the current state, the proposal stage uses a proposal generator to update the parameters of the current sample, θ, to obtain a new sample θ'. The newly obtained proposal is then passed through the verification stage to evaluate the likelihood of the proposal. The verification stage will then accept the newly proposed sample as the new state with a probability of:

$$a_t = min\left\{\frac{P(\theta'|D)}{P(\theta|D)}\,\frac{Q(\theta|\theta')}{Q(\theta'|\theta)}, 1\right\} \quad (46)$$

If the sample θ' is rejected, the iteration will continue with the current sample θ (Schönborn *et al.*, 2020). The pseudocode of the Metropolis-Hastings algorithm can be found in Figure 5.4

Function θ_{new} = MetropolisHastings($Q(\theta'|\theta), P(\theta|D)$)
  Input:
  $Q(\theta'|\theta)$ Proposal Generator
  $P(\theta|D)$ Posterior Distribution
  Output:
  θ' Updated sample
  /* Initialization */
  θ = current θ /*Sample from the current model instance*/
  /* Verification */
  $\theta' \leftarrow$ sample from $Q(\theta'|\theta)$ /*Sample from proposal distribution*/
  compute $P(\theta'|D)$ /*Posterior distribution with new proposal*/
  compute $P(\theta|D)$ /*Posterior distribution with current sample*/
  $a_t \leftarrow min\left\{\frac{P(\theta'|D)}{P(\theta|D)}\,\frac{Q(\theta|\theta')}{Q(\theta'|\theta)}, 1\right\}$ /*acceptance threshold*/
  If a_t = 1 **then**
    $\theta_{new} \leftarrow \theta'$ /*Proposal accepted*/
  else
    $\theta_{new} \leftarrow \theta$ /*Proposal rejected, keep current sample*/
  return θ_{new}
end

Figure 5.4: Metropolis-Hastings algorithm

5.3.2 Prior distribution

In the Bayesian setting, the Statistical Shape Model constructed in Chapter 3 is used as the prior distribution, $P(\theta)$. The entire set of parameters consists of the model coefficients, $\alpha_p = (\alpha_{p1}, \dots, \alpha_{pn})$, the translation parameters $t_p = (t_{px}, t_{py}, t_{pz})$ and the rotation angles $r_p = (\phi_p, \psi_p, \omega_p)$ which are represented as Euler angles (Schönborn *et al.*, 2020). Any assignment of the parameter set will lead to a surface denoted as $\Gamma(\theta)$ and to describe a contour of the proximal femur, a full set of θ is sufficient (Schönborn *et al.*, 2017). Thus, to produce a synthesized contour of the model, the SSM is set up in a 3D scene where a translation matrix has been used in Scalismo to align the model's centre of mass with the origin. The scene setup can be seen in Figure 5.5

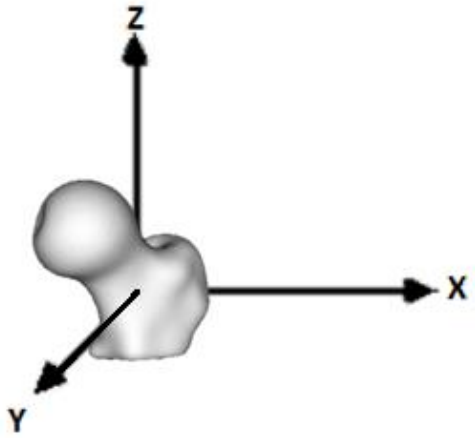

Figure 5.5: SSM scene setup

5.3.3 Proposal generator

For the proposed MH inference to be able to suggest updates for the parameter values in the current state, a proposal distribution is required. Random perturbations are the simplest method for updating parameters which can lead to a random walk in the parameter space when unbiased (Schönborn *et al.*, 2017). The random walk proposal provides the largest source of randomness in the MH algorithm. Two simple strategies have been employed in order to optimize the random walk proposal.

The first method is the block-wise mixture proposal where the main idea behind these proposals is that for a number of different proposals $Q_1(\theta'|\theta), \dots, Q_n(\theta'|\theta)$ where each one maps a state θ to a new state θ' the proposal can be defined by:

$$Q_M(\theta'|\theta) = \sum_{i=1}^{n} c_i \, Q_i(\theta'|\theta) \,, \qquad \sum_{i=1}^{n} c_i = 1 \tag{47}$$

where the mixture coefficient, c_i, represents the probability of drawing a proposal from Q_i. By using these different proposals, a mixture of different behaviours is achieved and thus variety is entered into the proposals. The mixture can lead to the exploration of the parameter space, which can not be achieved by a single proposal (Lüthi, 2020).

When working with shape model fitting algorithms, the parameter space can be high-dimensional and altering all the parameters at once could lead to the rejection of the proposed sample. Through block-wise proposals, only a part of the parameter space is updated at once (Schönborn *et al.*, 2017). Therefore the parameter updates were split into blocks and a separate proposal is defined for

rotation, translation and shape, namely Q_R, Q_T and Q_α. The final proposal would then be the mixture proposal:

$$Q_M(\theta'|\theta) = c_R Q_R(\theta'|\theta) + c_T Q_T(\theta'|\theta) + c_\alpha Q_\alpha(\theta'|\theta) \quad (48)$$

The second method used to optimize the random walk proposal is running several chains in sequence. As previously mentioned, when working with shape model fitting, the posterior distribution could be a complicated, multi-modal distribution. This could lead to the sampler getting stuck in a local mode when the sampler is initiated too far away from the real mode. To mitigate this problem, sampling chains could be run in sequence.

With this method, the first chain would only adjust a section of the parameter space. Once the chain has converged and the samples are concentrated in the mode containing the global maximum, the next chain could start. The initial parameters of the next chain would then be the best sample parameters from the previous chain. In this study the first sampling chain focuses on the rough pose, the second chain focuses on a model consisting of 7 modes of variation and the last chain focuses on the full model.

5.3.4 Likelihood

As seen in Equation 44, in order to perform Bayesian inference on the posterior distribution $P(\theta|D)$, given observed data D, a contour likelihood $P(D|\theta)$ is needed. Likelihoods are essential in the verification stage of the Metropolis-Hastings algorithm as it measures the compatibility of an explanation of the observed data (Thusini *et al.*, 2020). The explanation compatibility is determined by comparing the observed contour data with the synthesized contour from the current model instance θ. The likelihood is a function of the model parameters:

$$\ell(\theta; D) = P(D|\theta) \quad (49)$$

The synthesized contour of the current model instance is rendered into the image domain using the method described in Section 5.2.3. The synthesized contour is denoted as:

$$C_s = \{p_{s1}, p_{s2}, \dots, p_{sn}\} \quad (50)$$

where p_s represents the points of the synthesized contour. The likelihood in this study relies on soft correspondence, which means that for each point on the synthesized contour, the algorithm searches for the closest point on the

corresponding target contour (Thusini *et al.*, 2020). The target contour is extracted from the x-ray image using the method described in Section 5.2.2 and is denoted as:

$$C_t = \{p_{t1}, p_{t2}, \dots, p_{tn}\} \quad (51)$$

where p_t represents the points of the target contour. As the focus of this study is not to investigate the suitable likelihood function, the assumption is made that the points on the contours are independent and each point experiences Gaussian noise. Therefore, a Gaussian noise model is used to rate the distance between the synthesized points and the target points. The model likelihood is defined as:

$$\ell(\theta; C_t, \sigma_{C_t}) = \prod_i \mathcal{N}(C_s(p_{si}) - C_t(p_{ti})|0, \sigma_{C_t}) \quad (52)$$

5.4 Validation of reconstructed surface mesh

After the 3D patient-specific model instance has been reconstructed, the morphed mesh is compared to the corresponding ground-truth proximal femur mesh. The ground-truth mesh has been segmented from the CT scans in the testing dataset mentioned in Chapter 3. The quality of the reconstruction was evaluated by calculating the Hausdorff distance error, the average reconstruction error and the dice coefficient between the morphed surface and the ground-truth surface. Lastly, to determine if the algorithm could be applied to an SCFE dataset, the neck-shaft angle on the ground truth and reconstructed models is measured.

The Hausdorff distance measures the maximum distance between two meshes. Since anatomical landmarks are usually located at prominent surface features and are used for surgical measurements, the Hausdorff distance is a necessary metric to determine whether the worst-case scenario is located at a landmark feature. The Hausdorff distance error determines the similarity between two point sets by computing the one-sided distances (Bulbul *et al.* 2011). The one-sided differences between surface *A* and surface *B* can be calculated as follows:

$$Dist(A, B) = max(|a - b|) \quad (53)$$

$$Dist(B, A) = max(|b - a|) \quad (54)$$

where *a* and *b* refer to a point on mesh *A* and a point on mesh *B*. Because the distance is non-symmetric, the two-sided Hausdorff distances can then be

calculated as the maximum between the two one-sided distances determined in Equations 53 and 54. The Hausdorff distance is then denoted as:

$$H(A,B) = max(Dist(A,B), Dist(B,A)) \quad (55)$$

The average reconstruction error is a commonly used metric in literature used to measure the average error across the entire surface of the mesh. This metric defines the average distances between the vertices of the reconstructed surface and the ground-truth surface (Yu *et al.*, 2016). The average distance is determined by computing the shortest distance between each point of the first mesh and the surface of the second mesh and returning the average across all the points. The average reconstruction error is denoted as:

$$ARE = \frac{\sum_{i=1}^{n} |a_i - b_i|}{n} \quad (56)$$

where *n* is the total number of points located on the mesh. The dice coefficient is a metric that can be used to determine the pixel-wise agreement between the reconstructed mesh and the ground-truth mesh by computing a binary image for each of the meshes. This is accomplished using the `diceCoefficient` function in scalismo. The dice coefficient is determined as two times the number of voxels in which an overlap occurs divided by the sum of the number of voxels in mesh *A* and mesh *B* (Taha and Hanbury, 2015). The following equation is used to determine the dice coefficient:

$$DC = \frac{2 \times |A \cap B|}{|A| + |B|} \quad (57)$$

Lastly, the neck-shaft angle is known as the angle formed when a line through the femoral shaft intersects with a line through the femoral head and neck. Since the NSA measured during preoperative planning determines the amount of correction needed in the osteotomy, the measurement is used to determine if this algorithm could be applied to an SCFE dataset. The NSA is determined by identifying the neck axis and shaft axis on the model and measuring the angle between the axes as illustrated in Figure 5.6.

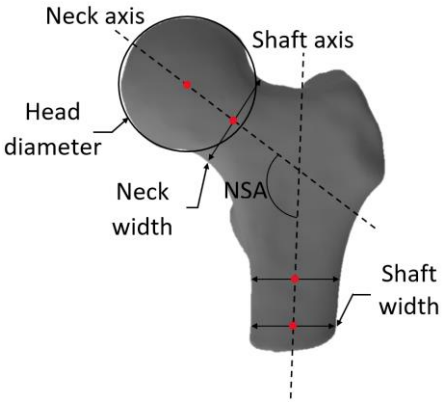

Figure 5.6: Neck-shaft angle measurement

5.5 Results

As mentioned in Section 3.5, 6 CT scans from the obtained dataset were set aside to be used for testing. These 6 CT scans were used to generate a DRR of the hip using the method described in Chapter 4. Once the DRR was generated, it was used as the target image in the reconstruction algorithm. Each of the reconstructed 3D models was compared against the ground truth using the measurements listed in Section 5.4. Table 5 contains the results of these measures whereas Tables 7 to 9 compare these results to other studies in the literature that reconstructed a 3D model from 2D images. Figure 5.7 and Figure 5.8 display the fit of some of the reconstructed models to the ground truth. The neck-shaft angle measurements are displayed in Table 6.

Table 5: Reconstruction results

Test Mesh	Average Reconstruction Error (mm)	Hausdorff Distance (mm)	Dice Coefficient
Mesh_01	1.95	4.83	0.90
Mesh_02	2.65	7.21	0.81
Mesh_03	1.98	5.06	0.91
Mesh_04	2.17	5.40	0.87
Mesh_05	2.00	5.14	0.88
Mesh_06	2.05	5.27	0.89
Average (mm, mm, -)	2.13	5.49	0.88
Standard Deviation (mm, mm, -)	0.26	0.87	0.04

Evaluating each reconstruction led to an average reconstruction error of 2.13 mm with an average Hausdorff Distance, which measures the maximum distance between two meshes, of 5.49 mm. The reconstructed along with the ground-truth meshes were converted to binary images and the overlap also known as the dice coefficient between the two meshes was measured. The average dice coefficient of the reconstructed meshes was measured to be 0.88. Lastly, the difference between the NSA measurements of the ground truth and reconstructed meshes ranges from 2.30° to 4.80° with an average difference of 3.05°.

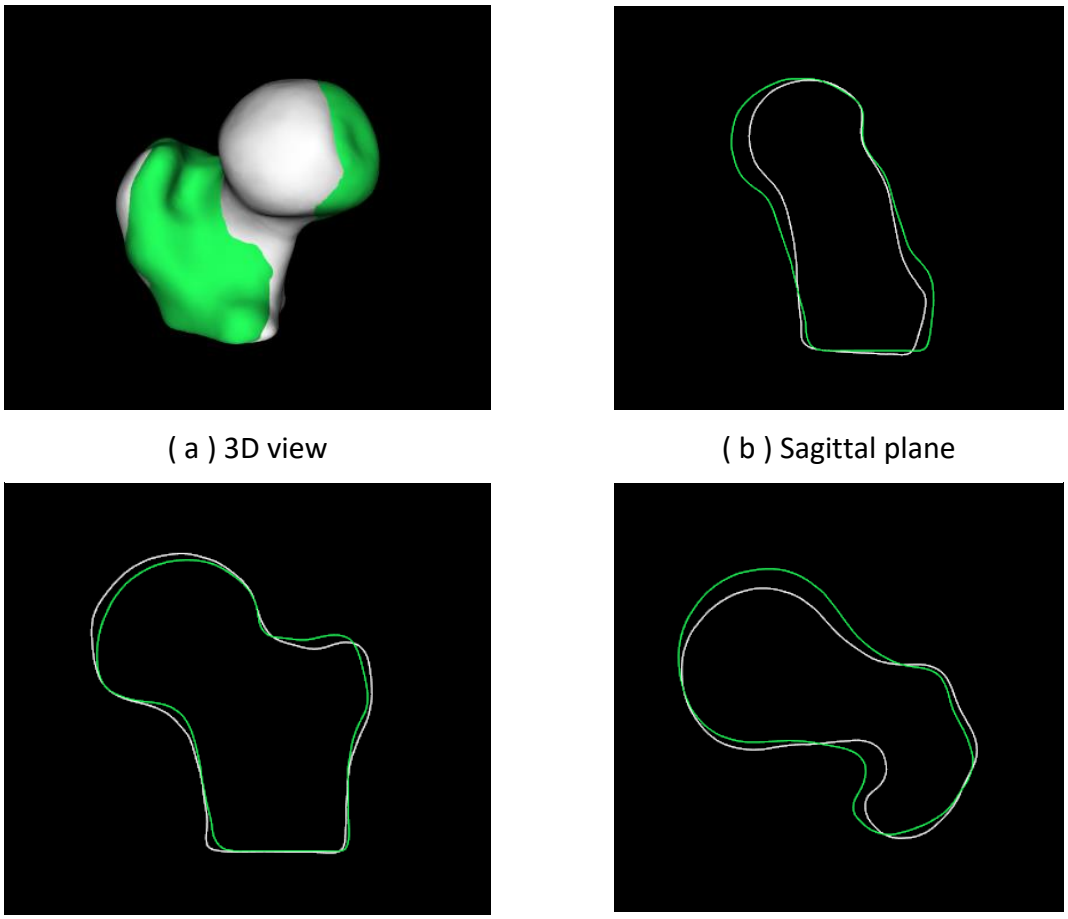

(a) 3D view (b) Sagittal plane

(c) Coronal plane (d) Axial plane

Figure 5.7: The reconstructed model (white) compared to the ground truth model (green) of Mesh_01

By interpreting the results in Tabel 5, it can be seen that Mesh_01 is the mesh with the least amount of error measured after validating the reconstructed mesh, whereas Mesh_02 has measured larger errors than the rest of the meshes in the testing dataset. The reconstructed model along with the ground truth surface mesh for the best and worst cases is displayed in Figure 5.7 and Figure 5.8 respectively.

Table 6: Neck-shaft angle measurements

Test Mesh	NSA of the reconstructed model (°)	NSA of the ground truth model (°)	Difference between the NSA angles (°)
Mesh_01	130.40	127.80	2.60
Mesh_02	131.50	126.70	4.80
Mesh_03	133.90	131.60	2.30
Mesh_04	126.40	123.40	3.00
Mesh_05	124.50	127.70	3.20
Mesh_06	123.50	121.10	2.40
Average (°)	128.37	126.38	3.05
Standard Deviation (°)	4.17	3.68	0.92

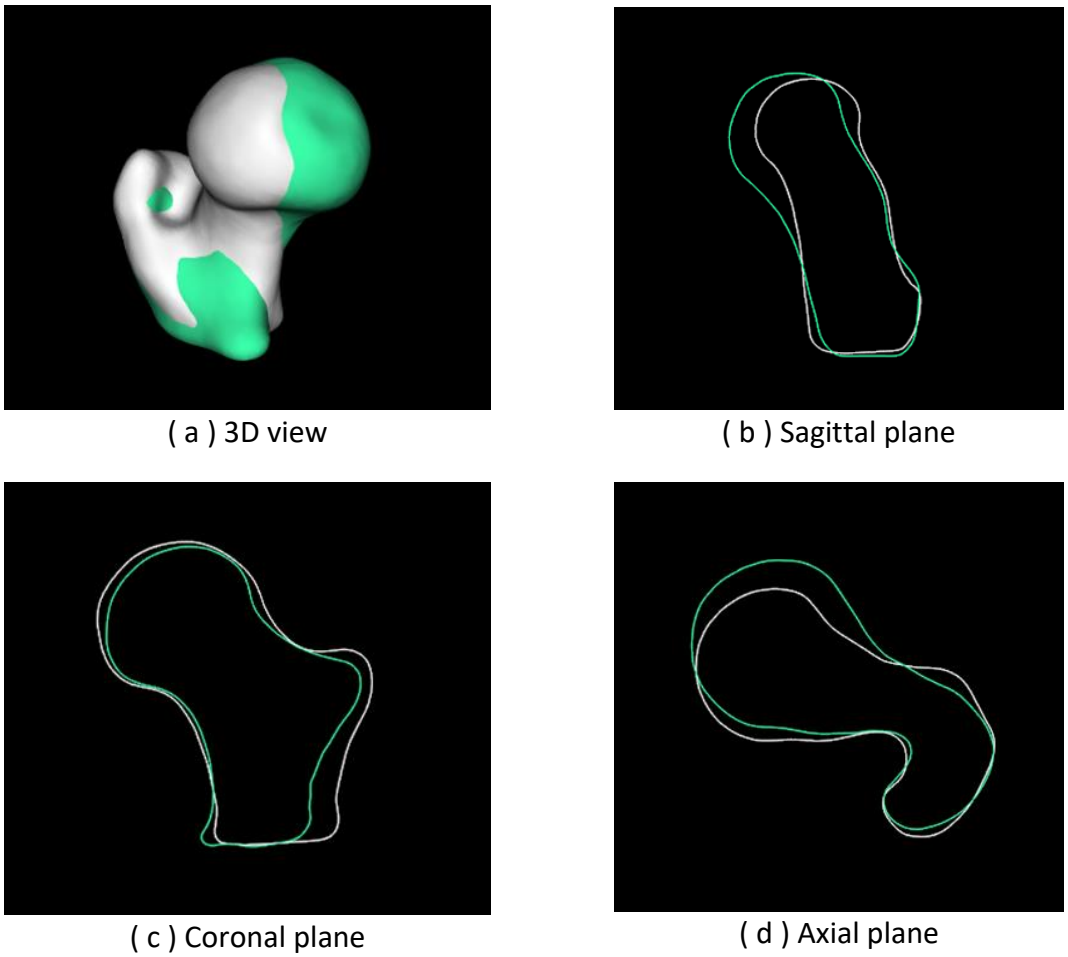

(a) 3D view (b) Sagittal plane

(c) Coronal plane (d) Axial plane

Figure 5.8: The reconstructed model (white) compared to the ground truth model (green) of Mesh_02

5.6 Discussion

Table 7: Average reconstruction error of studies in literature

	Current Study	Zheng (2011)	Steininger *et al.* (2008)	Ehlke *et al.* (2013)	Sadowsky *et al.* (2007)
Bone Structure	Proximal Femur	Proximal Femur	Proximal Femur	Pelvis	Pelvis
Number of x-ray views used	1	2	2	1	2
Average reconstruction error (mm)	2.13	1.40	2.78	2.00	2.00

The average reconstruction error, Equation 56, in this study ranges from 1.95 to 2.65 mm with an average of 2.13 mm as seen in Table 5. The reconstruction of 3D models from 2D images has been widely used in literature. The average reconstruction error obtained through a reconstruction algorithm by other studies in the literature can be seen in Table 7. Compared to the reconstruction errors found in Table 7 (Ehlke *et al.*, 2013; Steininger *et al.*, 2008; Zheng, 2011) which range from 1.40 to 2.78 mm it seems that the findings regarding the reconstruction error are coherent and that the average reconstruction error obtained fall within the ranges in the available literature.

Table 8: Hausdorff distance of studies in the literature

	Current Study	Thusini et al. (2020)		Steininger *et al.* (2008)
Bone Structure	Proximal Femur	Femur		Proximal Femur
Number of x-ray views used	1	1	2	2
Hausdorff distance (mm)	5.49	4.20 to 5.70	4.18 to 4.73	5.84

The Hausdorff distance is the measure that determines the maximum distance between two surface meshes. In this study an average Hausdorff distance of approximately 5.49 mm is obtained. Some of the Hausdorff distances obtained in

the literature are listed in Table 8. Thusini *et al.* (2020) performed a similar study where the femur was reconstructed from a single x-ray image and bi-planar x-rays. The average Hausdorff distance ranged from approximately 4.20 to 5.70 mm for a single x-ray image where the target shape was within reach of the model. For shapes that were out of the model's reach, the Hausdorff varied from approximately 22 to 25 mm. Steininger *et al.* (2008) reported a Hausdorff distance ranging from 4.24 to 10.06 mm, with an average Hausdorff distance of 5.84 mm for the reconstruction of a femur from radiographic images. Thus the average Hausdorff distance of this study falls within the range of available literature.

The dice coefficient is used to determine the overlap of the two meshes which indicates how well the reconstructed model resembles the target shape. The dice coefficient ranges from 0 which indicates no spatial overlap, to 1 which indicates a complete overlap between two shapes. The average dice coefficient obtained in this study was 0.88. Table 9 displays the dice coefficient of studies available in the literature. Steininger *et al.* (2008) reported an average dice coefficient of 0.90, ranging from 0.84 to 0.93, for using two or more x-rays for reconstruction. Whereas Yao and Taylor (2003), reported a dice coefficient of 0.64 and 0.86 for reconstructing a model from single and bi-planar x-rays respectively. The dice coefficient of this study ranges from 0.81 to 0.91 with an average dice coefficient of 0.88, which corresponds to the values obtained in the available literature.

Table 9: Dice coefficient of studies in literature

	Current Study	**Steininger *et al.* (2008)**	**Yao & Taylor (2003)**	
Bone Structure	Proximal Femur	Proximal Femur	Pelvis	
Number of x-ray views used	1	2	1	2
Dice coefficient	0.88	0.90	0.64	0.86

When observing the results in Tables 7 to 9, it can be seen that the findings of this study concur with the results available in the literature. However, the Hausdorff distances are mainly located at the femoral head in the sagittal plane. When using the reconstructed model for preoperative planning this could lead to inaccuracies in the measurements made since the neck-shaft angle is dependent on the axis passing through the femoral head and neck. Thus, the Hausdorff distance can be

improved to improve the accuracy of the model and thus reduce the differences between the ground truth and reconstructed NSAs.

Livyatan *et al.* (2003) recommended that an acceptable average 2D/3D reconstruction error should range from 1 to 1.50 mm, or 2 to 3 mm in the worst scenario, based on the analysis of common orthopaedic procedures. The average reconstruction error obtained in this study is 2.13 mm which meets the specification of Livyatan *et al.* (2003) but can be improved to fall within the 1 to 1.50 mm range. Yao and Taylor (2003) stated that there are a variety of factors that can influence the accuracy of the reconstruction algorithm. The factors can include the number of input images used, the sample size of the SSM and the quality of the target image.

The number of x-ray views used to reconstruct the model may have a large impact on the accuracy of the reconstructed model. According to Reyneke *et al*. (2018), adding a radiographic image to the reconstruction algorithm significantly improves the resulting reconstruction. By observing the reconstructions in Figures 5.7 and 5.8, it can be seen that the reconstruction is more precise in the coronal plane than in the sagittal plane. This is due to the target x-ray image being in the coronal plane and thus the reconstruction algorithm does not have enough information about the sagittal plane. Thus, the resulting model shows more inconsistencies in the area of the femoral head and shaft where the width is modelled. Therefore adding a radiograph of the sagittal plane could increase the accuracy of the model.

However, using this approach could lead to difficulties in automatically identifying the femur during edge detection as a sagittal radiograph would have an overlap of the target femur, the pelvis and the contralateral femur. Thus, when adding target images to the algorithm, the edge detection algorithm might require user interaction to ensure the correct contour has been identified.

The prior knowledge of the algorithm, which is the SSM in this case, could also have an impact on the accuracy. The generality of the model determines how well the model can represent shapes that are not within the training dataset. It is believed that increasing the size of the training dataset, will increase the model's ability to fit unseen data.

Since the target x-ray used within the reconstruction algorithm was a synthesized image and not the ground-truth image, it could affect the accuracy of the reconstructed model. Thus, the validation dataset should be enlarged to include the CT scans as well as the clinical x-rays of the patients in the population to increase the accuracy of the model.

Finally, to determine whether the algorithm can sufficiently reconstruct the 3D NSA from a 2D x-ray, the NSA of the reconstructed model was measured and compared to that of the ground truth model. As seen in Table 6, the difference

between the measurements range from 2.30° to 4.80° with an average difference of 3.05°. To the author's knowledge, there are currently no studies that apply 2D/3D reconstruction to SCFE cases. However, in a study by Cherkasskiy *et al.* (2017), 3D models were reconstructed from CT scans of patients diagnosed with SCFE and NSA measurements were performed. The NSAs of these reconstructed models were compared to the NSA measured on 2D radiographs and found that the average reconstructed NSA differs from the 2D NSA by approximately 5°. According to Schlégl *et al.* (2022), an acceptable normal range for neck-shaft angles in children is approximately 10°. All of the measured NSAs fall within this range with a maximum measured difference of 4.80° and the results correspond to the results of Cherkasskiy *et al.* (2017).

The difference between the measured angles could be due to the factors listed above which affect the accuracy of the reconstructed model. As previously mentioned, the Hausdorff distance is mainly located at the femoral head in the sagittal plane, which has an impact on the head-neck axis and ultimately affects the NSA measurement. Improving the Hausdorff distance of the model could reduce the differences between the reconstructed and ground truth NSAs. With the NSA differences all within the acceptable range and comparing well to the measurements made by Cherkasskiy *et al.* (2017), the results indicate that the reconstruction algorithm can adequately reconstruct the NSA from 2D radiographs and thus the dataset can be enlarged to include SCFE data.

Chapter 6

Conclusions

An indispensable requirement for the success of any orthopaedic procedure is pre-operative planning. The traditional method relies on 2D radiographs, but the lack of 3D information, overlapping anatomical structures and the quality of the radiograph could affect the accuracy of the measurements made (Kordelle *et al.*, 2000). The accuracy and reliability in the treatment of SCFE can be improved by utilizing 3D models more extensively in the preoperative planning process. Although CT scans are the preferred 3D imaging modality, it has certain limitations in the case of SCFE which include high radiation exposure to younger individuals and being expensive. Therefore a reconstruction of 3D models from 2D images is considered an attractive alternative to obtaining 3D models (Dakhakhni, 2013). These reconstruction algorithms produce detailed 3D patient data without the cost and radiation associated with CT scans. Thus, the focus of this study was then to develop an algorithm that could reconstruct a 3D patient-specific model from a 2D x-ray image. To achieve the aim of the study, the objectives involved developing an SSM along with a 2D/3D reconstruction algorithm, and validating the results. This chapter offers conclusions on the main findings and contributions, recommendations on possible improvements to the study and suggestions for future work are given.

6.1 Main findings and contribution

A dataset, containing 33 CT scans of the hip, which was available for public access was obtained to use throughout this study. Since the region of interest in this study is identified as the femur, the left proximal femur in each image was segmented and saved as a surface mesh. Out of the 33 proximal femurs available, 27 femurs were used to construct the SSM, which leaves 6 proximal femurs to be used as a testing dataset to achieve an 80:20 data distribution as proposed by Heimann and Meinzer (2009). The GPMM construction method described by Lüthi *et al.* (2017) was used to construct the SMM. The GPMM method models the variation within the population as deformations from the reference mesh. Once the dataset was aligned and correspondence was established, PCA was performed on the covariance matrix to obtain the main modes of variation. The modes of variation are ordered in descending order according to the amount of variance explained by the mode of variation.

The quality of the statistical shape model was assessed using three measures, namely compactness, specificity and generality. The model showed promising results in all of the evaluation measures. Although it is difficult to compare the

results to other studies available in the literature due to different sample sizes, different regions of interest and methods used, the results obtained from this study fall within the ranges of literature and thus the results were deemed acceptable.

The reconstruction algorithm was accomplished by using the constructed SSM as prior knowledge and MCMC sampling methods for inference. Using a Metropolis Hasting algorithm allowed for an analysis-by-synthesis approach where contours were synthesized from the SSM and compared to contours extracted from the x-ray image. The contours were compared by measuring the point-to-point distance between the synthesized and target contour. Since the dataset only contained CT images, an x-ray image was generated using a DRR rendering technique. The generated x-ray image was used as the target image in the reconstruction algorithm.

The Metropolis-Hastings algorithm was used to generate sample contours from a proposal distribution, which were then accepted or rejected based on their likelihood under the posterior distribution. The algorithm is an iterative process where the SSM parameters were adjusted with each observation based on the information obtained from the 2D image. The resulting model was the sampled contour with the best likelihood after the iterative process have been completed.

After the patient-specific model was reconstructed, the model was compared against the ground-truth model to determine the accuracy of the reconstruction. The measurements used to evaluate the model were the average reconstruction error, the Hausdorff distance and the dice coefficient. The results obtained were consistent with the results found in available literature, but the average error and Hausdorff distance could still be improved. Therefore, some alterations need to be made to the reconstruction algorithm to improve the accuracy of the model. The comparison of the neck-shaft angle of the reconstructed model to that of the ground truth model indicated that the reconstruction algorithm could be adapted to include an SCFE dataset.

6.2 Future work

The motivation behind this study was to reconstruct a 3D patient-specific model from 2D data with the intention to be used during the preoperative planning of SCFE correction osteotomies. However, one of the limitations of this study was that the dataset used to train the SSM included CT scans from an adult USA-based population instead of an SCFE dataset from an adolescent South African population. Due to the limited available cases and lack of time, this dataset was used as a proxy as it was already publically available and ready for use. The biggest difference between an adult and adolescent dataset is that the size and shape of the femur will differ since the femur of adolescents still develops until the growth

plate close. A femur from a USA population may also differ from a femur of a South African population due to Aronsson et al. (2006) and Lehmann et al. (2006) assumption that factors such as genetic background and cultural traditions affect the prevalence of SCFE. This study was used to develop the techniques which could eventually be applied to an SCFE dataset. Since this study was only proof-of-concept, future studies would first have to train an SSM on SCFE CT scans of a younger age group from a specific population after the shortcomings of the current approach have been addressed.

Since the accuracy of the model needs to be improved in order to apply the method to clinical applications, the following recommendations could be applied to improve the reconstruction algorithm:

1. **Increase the sample size:** There is limited literature available on the required sample size needed to construct a statistical shape model and according to Mei *et al.* (2008) this is because the issue of sufficiency is not considered. Mei et al. (2008) stated that the sample size requirement should depend on two factors, namely the level of noise and the number of structural modes since these are the characteristics that affect the sufficiency of the sample size. The process of shape model construction was limited by a training dataset containing only 27 proximal femurs. Although the shape model used in the study showed promising results, a larger training dataset would improve the generality of the model. Increasing the generality allows the model's ability to represent shape instances which are not included in the training data to improve and could lead to better results.

2. **Improve the contour generation technique:** The reconstruction algorithm is very time-consuming as it takes about 30 seconds just to run one iteration. The main reason for the long computation time is that, within the likelihood function, the shape sample is projected to the corresponding x-ray image through a rendering technique where the algorithm steps through each pixel of the projection plane. If this method is improved, the computation time could be reduced and the algorithm would be more cost-effective.

3. **Include more radiographic images:** Since only a single 2D image has been used to reconstruct a 3D model, some of the information needed to accurately reconstruct the model could not be provided. During this study, the contours from the coronal plane were used for the reconstruction algorithm, which means that the shape could not obtain information such as the shaft width from the sagittal plane. Thus the resulting shape showed inconsistencies in the shaft and femoral head area in the sagittal plane. Yao and Taylor (2003) stated that adding additional x-ray images to the

reconstruction algorithm has diminished returns regarding the accuracy of the model. However, it has been proven in the literature that using multiple radiographic images shows a significant improvement in the accuracy of the reconstructed model (Reyneke *et al.*, 2018; Thusini *et al.*, 2020). Therefore, by including more x-rays the reconstruction algorithm could show improved results. Although it could lead to an improvement in reconstruction accuracy, a lateral image would display an overlap of the target femur, the pelvis and the contralateral femur which could complicate the automatic identification of the target femur contour in the edge detection algorithm. Thus, when adding additional target images to the reconstruction algorithm, user interaction might be required to determine if the correct contour has been identified. Future studies might overcome this problem by using a 2D active shape model or a method developed by Peng (2002), where a modified Canny Edge detection algorithm in combination with an active contour algorithm is used to automatically detect contours.

4. **Use a ground-truth x-ray:** Since the DRR could not be verified, we could not be sure that the information provided to the reconstruction algorithm is correct. This could lead to inconsistencies between the ground truth mesh extracted from the CT data and the synthesized x-ray. Running the algorithm with ground-truth data might increase the accuracy of the reconstructed model. To validate whether the accuracy of the model improved a 3D model would be reconstructed from both a DRR and the ground-truth x-ray image and the results would be compared.

6.3 Final remarks

The objective of this study was to develop a reconstruction algorithm that reconstructs a 3D patient-specific model from a 2D radiographic image. An SSM was reconstructed and an x-ray was synthesized to be used as the prior knowledge and the observed data in the reconstruction algorithm respectively. The resulting reconstructed mesh was compared to the corresponding ground truth mesh segmented from CT data. Although the results obtained within this study correspond with the available literature on the reconstruction of 3D from 2D images, the Hausdorf distances and average reconstruction error could still be improved. Comparing the neck-shaft angle of the reconstructed model to that of the ground truth model indicated that the reconstruction algorithm can sufficiently reconstruct the NSA from 2D x-rays and thus can be adapted to include a dataset with SCFE-diagnosed patients. Thus although the algorithm is able to reconstruct a patient-specific model from a radiographic image, the accuracy of the model needs to be improved to be used in pre-operative planning.

References

Abu Amara, S., Leroux, J. and Lechevallier, J. 2014. Surgery for slipped capital femoral epiphysis in adolescents. *Orthopaedics and Traumatology: Surgery and Research*. 100(1), pp. S157–S167.

Alvarez-Gomez, J.C., Palavicini, G.J., Roth, H. and Wahrburg, J. 2021. An ultra-fast Digitally Reconstructed Radiograph (DRR) implementation of the Siddon-Jacobs algorithm using parallel computing: runtime improvement of an intensity-based 2D/3D registration. *Current Directions in Biomedical Engineering*. 7(2), pp. 25–28.

Aronsson, D.D., Loder, R.T., Breur, G.J. and Weinstein, S.L. 2006. Slipped capital femoral epiphysis: current concepts. *Journal of American Academy and Orthopaedic Surgeons*. 14(12), pp. 666–679.

Atesok, K., Galos, D., Jazrawi, L.M. and Egol, K.A. 2015. Preoperative planning in orthopaedic surgery. *Bulletin of the Hospital for Joint Disease,* 73(4).

Atkins, P.R., Shin, Y., Agrawal, P., Elhabian, S.Y., Whitaker, R.T., Weiss, J.A., Aoki, S.K., Peters, C.L., et al. 2019. Which two-dimensional radiographic measurements of cam femoroacetabular impingement best describe the three-dimensional shape of the proximal femur? *Clinical Orthopaedics and Related Research*. 477(1), pp. 242–253.

Aubin, C.E., Dansereau, J., Parent, F., Labelle, H. and de Guise, J.A. 1997. Morphometric evaluations of personalised 3D reconstructions and geometric models of the human spine. *Medical and Biological Engineering and Computing*. 35(6), pp. 611–618.

Balasubramanian, B., Alshryda, S. and Madan, S. 2019. Slipped capital femoral epiphysis. In *The Pediatric and Adolescent Hip*, (pp. 207–252). Springer, Cham

Barmada, R., Bruch, R.F., Gimbel, J.S. and Ray, R.D. 1978. Base of the neck extracapsular osteotomy for correction of deformity in slipped capital femoral epiphysis. *Clinical orthopaedics and related research*. (132), pp. 98–101.

Baur, M., Uhlmann, N., Pöschel, T. and Schröter, M. 2019. Correction of beam hardening in X-ray radiograms. *Review of Scientific Instruments*. 90(2), pp. 025108.

Benameur, S., Mignotte, M., Parent, S., Labelle, H., Skalli, W. and De Guise, J. 2003. 3D/2D registration and segmentation of scoliotic vertebrae using statistical models. *Computerized Medical Imaging and Graphics*. 27(5), pp. 321–337.

Betts, J.G., Wise, J.A., Young, K.A., Desaix, P., Johnson, E., Korol, O., Johnson, J.E., Kruse, D.H., et al. 2013. *Anatomy and Physiology*. OpenStax.

Betz, R.R., Steel, H.H., Emper, W.D., Huss, G.K. and Clancy, M. 1990. Treatment of

slipped capital femoral epiphysis. Spica-cast immobilization. *The Journal of Bone and Joint Surgery*. 72(4), pp. 587–600.

Birkfellner, W., Seemann, R., Figl, M., Hummel, J., Ede, C., Homolka, P., Yang, X., Niederer, P., et al. 2005. Fast DRR generation for 2D/3D registration. In *International Conference on Medical Image Computing and Computer-Assisted Intervention.* (pp. 960-967). Springer, Berlin, Heidelberg.

Bizdikian, A.J., Assi, A., Bakouny, Z., Yared, F., Saghbini, E., Bakhos, G.E., Esber, S., Khalil, N., et al., 2018. Validity and reliability of different techniques of neck–shaft angle measurement. *Clinical Radiology*. 73(11), pp. 984.e1-984.e9.

Bryan, R., Nair, P.B. and Taylor, M. 2009. Use of a statistical model of the whole femur in a large scale, multi-model study of femoral neck fracture risk. *Journal of Biomechanics*. 42(13), pp.2171–2176.

Bulbul, A., Capin, T., Lavoue, G. and Preda, M. 2011. Assessing visual quality of 3-D polygonal models. *IEEE Signal Processing Magazine*. 28(6), pp. 80–90.

Canny, J., 1986. A computational approach to edge detection. *IEEE Transactions on Pattern Analysis and Machine Intelligence*. (6), pp. 679–698.

Cerveri, P., Belfatto, A. and Manzotti, A. 2019. Pair-wise vs group-wise registration in statistical shape model construction: representation of physiological and pathological variability of bony surface morphology. *Computer Methods in Biomechanics and Biomedical Engineering*. 22(7), pp. 772–787.

Chan, E.F., Farnsworth, C.L., Koziol, J.A., Hosalkar, H.S. and Sah, R.L. 2013. Statistical shape modeling of proximal femoral shape deformities in Legg–Calvé–Perthes disease and slipped capital femoral epiphysis. *Osteoarthritis and Cartilage*. 21(3), pp. 443–449.

Cherkasskiy, L., Caffrey, J.P., Szewczyk, A.F., Cory, E., Bomar, J.D., Farnsworth, C.L., Jeffords, M., Wenger, D.R., et al. 2017. Patient-specific 3D models aid planning for triplane proximal femoral osteotomy in slipped capital femoral epiphysis. *Journal of Children's Orthopaedics*. 11(2), pp. 147–153.

Cootes, T.F. and C.J., 2004 *Statistical models of appearance for computer vision*. University of Manchester.

Dakhakhni, H.A.A.F., 2013. *Reconstruction of patient-specific bone models from x-ray radiography*. (Doctoral dissertation, Dissertation, University of Tennessee, Knoxville)

Davies, R.H., 2002. *Learning shape: optimal models for analysing natural variability*. The University of Manchester (United Kingdom).

De Rosa, G.P., Mullins, R.C. and Kling, Jr T.F., 1996. Cuneiform osteotomy of the femoral neck in severe slipped capital femoral epiphysis. *Clinical orthopaedics and related research*. (322), pp. 48–60.

Drapikowski, P., Tyrakowski, M., Czubak, J. and Czwojdzinski, A. 2008. Computer assisted SCFE osteotomy planning. *International Journal of Computer Assisted Radiology and Surgery*. 3(5), pp. 421–426.

Ehlke, M., Ramm, H., Lamecker, H., Hege, H.C. and Zachow, S. 2013. Fast generation of virtual X-ray images for reconstruction of 3D anatomy. *IEEE transactions on visualization and computer graphics*. 19(12), pp. 2673–2682.

Ferguson, A.B. and Howorth, M.B. 1931. Slipping of the upper femoral epiphysis: A study of seventy cases. *Journal of the American Medical Association*. 97(25), pp.1867.

Fetto, J., Leali, A. and Moroz, A. 2002. Evolution of the Koch model of the biomechanics of the hip: clinical perspective. *Journal of Orthopaedic Science*. 7(6), pp. 724–730.

Fish, J.B. 1984. Cuneiform osteotomy of the femoral neck in the treatment of slipped capital femoral epiphysis. *The Journal of Bone and Joint Surgery. American volume*, 66(8), pp. 1153–1168.

Fleute, M., Lavallée, S. and Julliard, R. 1999. Incorporating a statistically based shape model into a system for computer-assisted anterior cruciate ligament surgery. *Medical Image Analysis*. 3(3), pp. 209–222.

Folkerts, M.M., 2015. Digitally reconstructed radiograph. *Graphics Processing Unit-Based High Performance Computing in Radiation Therapy*, pp. 15–28.

Gholve, P.A., Cameron, D.B. and Millis, M.B., 2009. Slipped capital femoral epiphysis update. *Current Opinion in Pediatrics*. 21(1), pp. 39–45.

Graetz, J., 2016. High performance volume ray casting: A branchless generalized Joseph projector. (September, 4). *arXiv preprint arXiv: 1609.00958.*

Graham, H.K., Shore, B.J. and Kelley, S.P., 2018. Flexion-valgus intertrochanteric osteotomy for late-slipped capital femoral epiphysis deformity. In *Pediatric Pelvic and Proximal Femoral Osteotomies* (pp. 187-195), Springer, Cham.

Hak, D.J. and Rose, J. 2010. Preoperative planning in orthopedic trauma: benefits and contemporary uses. *Orthopedics*, 33(8), pp.581–584.

Heimann, T. and Meinzer, H.P. 2009. Statistical shape models for 3D medical image segmentation: A review. *Medical Image Analysis*. 13(4), pp. 543–563.

Hosseinian, S. and Arefi, H., 2015. 3D Reconstruction from multi-view medical x-ray images - review and evaluation of existing methods. *International Archives of the Photogrammetry, Remote Sensing and Spatial Information Sciences*., 40.

Humbert, L., De Guise, J.A., Aubert, B., Godbout, B. and Skalli, W., 2009. 3D reconstruction of the spine from biplanar X-rays using parametric models based on transversal and longitudinal inferences. *Medical Engineering and*

Physics. 31(6), pp. 681–687.

Jacobs, F., Sundermann, E., Christiaens, M., De Sutter, B. and Lemahieu, I. 1998. A Fast Algorithm to Calculate the Exact Radiological Path Through a Pixel Or Voxel Space. *Article in Journal of Computing and Information Technology*. 6(1), pp. 89–94.

Jerre, R., Billing, L., Hansson, G., Karlsson, J. and Wallin, J. 1996. Bilaterality in slipped capital femoral epiphysis: Importance of a reliable radiographic method. *Journal of Pediatric Orthopaedics Part B*. 5(2), pp. 80–84.

Jia, X., Yan, H., Cerviño, L., Folkerts, M. and Jiang, S.B., 2012. A GPU tool for efficient, accurate, and realistic simulation of cone beam CT projections. *Medical Physics*. 39(12), pp. 7368–7378.

Kallio, P.E., Mah, E., Foster, B.K., Paterson, D.C. and LeQuesne, G.W., 1995. Slipped capital femoral epiphysis. Incidence and clinical assessment of physeal instability. *The Journal of Bone and Joint Surgery. British volume*. 77(5), pp. 752–755.

Kamegaya, M., Saisu, T., Ochiai, N. and Moriya, H., 2005. Preoperative assessment for intertrochanteric femoral osteotomies in severe chronic slipped capital femoral epiphysis using computed tomography. *Journal of Pediatric Orthopaedics B*. 14(2), pp. 71–78.

Katiyar, S.K. and Arun, P.V., 2014. Comparative analysis of common edge detection techniques in context of object extraction. arXiv preprint arXiv:1405.6132.

Killoran, J.H., Baldini, E.H., Beard, C.J. and Chin, L. 2001., A technique for optimization of digitally reconstructed radiographs of the chest in virtual simulation. *International Journal of Radiation Oncology* Biology* Physics*. 49(1), pp. 231–239.

Kim, J., Glide-Hurst, C., Doemer, A., Wen, N., Movsas, B. and Chetty, I.J., 2015. Implementation of a novel algorithm for generating synthetic CT images from magnetic resonance imaging data sets for prostate cancer radiation therapy. *International Journal of Radiation Oncology* Biology* Physics*. 91(1), pp. 39–47.

Kordelle, J., Mamisch, C., Kikinis, R., Seibel, R. and Richolt, J.A., 2000. Anatomical analysis and preoperative planning of correctional osteotomies: slipped capital femoral epiphysis (SCFE). *Minimally Invasive Therapy and Allied Technologies*. 9(3–4), pp. 269–276.

Kramer, W.G, Craig, W.A. and Noel, S., 1976. Compensating osteotomy at the base of the femoral neck for slipped capital femoral epiphysis. *The Journal of Bone and Joint Surgery. American Volume*. 58(6), pp. 796–800.

Laporte, S., Skalli, W., De Guise, J.A., Lavaste, F. and Mitton, D. 2003. A biplanar reconstruction method based on 2D and 3D contours: application to the distal

femur. *Computer Methods in Biomechanics and Biomedical Engineering*. 6(1), pp. 1–6.

Lebailly, F., Lima, L.V.P.C., Clairemidi, A., Aubert, B., Guerard, S., Chaibi, Y., de Guise, J., Fontaine, C. and Skalli, W., 2012. Semi-automated stereoradiographic upper limb 3D reconstructions using a combined parametric and statistical model: a preliminary study. *Surgical and Radiologic Anatomy*. 34(8), pp. 757–765.

Lehmann, C.L., Arons, R.R., Loder, R.T. and Vitale, M.G. 2006. The epidemiology of slipped capital femoral epiphysis: an update. *Journal of Pediatric Orthopaedics*. 26(3), pp. 286–290.

Livyatan, H., Yaniv, Z. and Joskowicz, L. 2003. Gradient-based 2-D/3-D rigid registration of fluoroscopic X-ray to CT. *IEEE Transactions on Medical Imaging*. 22(11), pp. 1395–1406.

Loder, R.T., 1996. The demographics of slipped capital femoral epiphysis. An international multicenter study. Clinical orthopaedics and related research, (322), pp.8-27.

Loder, R.T., 1998. Slipped capital femoral epiphysis. *Americal Family Physician*. 57(9), pp. 2135–2142.

Loder, R.T. and Skopelja, E.N., 2011. The epidemiology and demographics of slipped capital femoral epiphysis. *International Scholarly Research Notices*. 2011.

Loder, R.T., Richards, B.S., Shapiro, P.S., Reznick, L.R. and Aronson, D.D. 1993. Acute slipped capital femoral epiphysis: the importance of physeal stability. *The Journal of Bone and Joint Surgery*. 75(8), pp. 1134–1140.

Loder, R.T., Aronsson, D.D., Dobbs, M.B. and Weinstein, S.L. 2000. Slipped capital femoral epiphysis. *Journal of Bone and Joint Surgery*. 82(8), pp. 1170–1188.

Lüthi, M., Gerig, T., Jud, C. and Vetter, T. 2017. Gaussian process morphable models. *IEEE Transactions on Pattern Analysis and Machine Intelligence*. 40(8), pp. 1860–1873.

Lüthi, M. 2020. *Probabilistic fitting*. [Online], Available: https://shapemodelling.cs.unibas.ch/probabilistic-fitting-course/.

Lüthi, M. and Bouabene, G. 2020. *Statistical shape modelling: Computing the Human Anatomy*. [Online], Available: https://www.futurelearns.com/courses/statistical-shape-modelling.

Mei, L., Figl, M., Darzi, A., Rueckert, D. and Edwards, P., 2008. Sample sufficiency and PCA dimension for statistical shape models. In *European Conference on Computer Vision*. (pp. 492–503) Springer, Berlin, Heidelberg.

Merchán, E.C.R., Na, C.M. and Munuera, L., 1992. Intertrochanteric osteotomy for

the treatment of chronic slipped capital femoral epiphysis. *International Orthopaedics*. 16(2), pp. 133–135.

Mitton, D., Landry, C., Véron, S., Skalli, W., Lavaste, F. and De Guise, J.A., 2000. 3D reconstruction method from biplanar radiography using non-stereocorresponding points and elastic deformable meshes. *Medical and Biological Engineering and Computing*. 38(2), p. 133–139.

Mitton, D., Deschênes, S., Laporte, S., Godbout, B., Bertrand, S., de Guise, J.A. and Skalli, W., 2006. 3D reconstruction of the pelvis from bi-planar radiography. *Computer Methods in Biomechanics and Biomedical Engineering*. 9(1), pp. 1–5.

Mitulescu, A., Semaan, I., De Guise, J.A., Leborgne, P., Adamsbaum, C. and Skalli, W. 2001. Validation of the non-stereo corresponding points stereoradiographic 3D reconstruction technique. *Medical and Biological Engineering and Computing*. 39(2):152–158.

Mitulescu, A., Skalli, W., Mitton, D. and De Guise, J., 2002. Three-dimensional surface rendering reconstruction of scoliotic vertebrae using a non stereo-corresponding points technique. European spine journal, 11(4), pp.344-352.

Moore, C.S., Liney, G.P., Beavis, A.W. and Saunderson, J.R., 2011. A method to produce and validate a digitally reconstructed radiograph-based computer simulation for optimisation of chest radiographs acquired with a computed radiography imaging system. *The British Journal of Radiology*. 84(1006), pp. 890–902.

Moore, K.L., Dalley, A.F. and Agur, A.M.R. 2013. *Clinically Oriented Anatomy*. Lippincott Williams and Wilkins.

Mu, Z., 2016. A fast DRR generation scheme for 3D-2D image registration based on the block projection method. *Proceedings of the IEEE Conference on Computer Vision and Pattern Recognition Workshops* (pp. 169–177).

Muschelli, J., 2019. Recommendations for processing head CT data. Frontiers in neuroinformatics, 13, p.61.

Mutsvangwa, T., Burdin, V., Schwartz, C. and Roux, C. 2014. An automated statistical shape model developmental pipeline: application to the human Scapula and Humerus. *IEEE Transactions on Biomedical Engineering*. 62(4), pp. 1098–1107.

Nortje, M.B., 2009. Single pin versus multiple pin fixation in the management of slipped upper femoral epiphysis (Master's thesis, University of Cape Town).

Peck, D.M., Voss, L.M. and Voss, T.T. 2017. Slipped capital femoral epiphysis: diagnosis and management. *American Family Physician*. 95(12), pp. 779–784.

Peng, T.T., 2002. Detection of Femur Fractures in X-ray images. Master of Science Thesis, National University of Singapore

Quijano, S., Serrurier, A., Aubert, B., Laporte, S., Thoreux, P. and Skalli, W., 2013. Three-dimensional reconstruction of the lower limb from biplanar calibrated radiographs. *Medical Engineering and Physics*. 35(12), pp. 1703–1712.

Reyneke, C.J.F., Lüthi, M., Burdin, V., Douglas, T.S., Vetter, T. and Mutsvangwa, T.E., 2018. Review of 2D/3D reconstruction using statistical shape and intensity models and x-ray image synthesis: toward a unified framework. *IEEE reviews in biomedical engineering*. 12, pp. 269–286.

Richolt, J.A., Teschner, M., Everett, P., Girod, B., Millis, M.B. and Kikinis, R., 1998. Planning and evaluation of reorienting osteotomies of the proximal femur in cases of SCFE using virtual three-dimensional models. In *International Conference on Medical Image Computing and Computer-Assisted Intervention* (pp. 1–8). Springer, Berlin, Heidelberg

Richolt, J.A., Teschner, M., Everett, P.C., Millis, M.B. and Kikinis, R., 1999. Impingement simulation of the hip in SCFE using 3D models. *Computer Aided Surgery Official Journal of the International Society for Computer Aided Surgery (ISCAS)*. 4(3), pp. 144–151.

Sadowsky, O., Chintalapani, G. and Taylor, R.H., 2007. Deformable 2D-3D registration of the pelvis with a limited field of view, using shape statistics. In *International Conference on Medical Image Computing and Computer-Assisted Intervention*. (pp. 519–526). Springer, Berlin, Heidelberg.

Salhi, A., Burdin, V., Boutillon, A., Brochard, S., Mutsvangwa, T. and Borotikar, B. 2020. Statistical shape modeling approach to predict missing scapular bone. *Annals of Biomedical Engineering*. 48(1), pp. 367–379.

Sarkalkan, N., Weinans, H. and Zadpoor, A.A., 2014. Statistical shape and appearance models of bones. *Bone*. 60, pp. 129–140.

Schlégl, Á.T., Nyakas, V., Kovács, D., Maróti, P., Józsa, G. and Than, P., 2022. Neck-shaft angle measurement in children: accuracy of the conventional radiography-based (2D) methods compared to 3D reconstructions. *Scientific Reports*. 12(1), pp. 1-8.

Schönborn, S., Egger, B., Morel-Forster, A. and Vetter, T. 2017. Markov chain monte carlo for automated face image analysis. *International Journal of Computer Vision*. 123(2), pp. 160–183.

Schönborn, S., Morel-Forster, A. and Egger, B. 2020. *Probabilistic Fitting and 2D Face Image Analysis*. [Online], Available: http://gravis.cs.unibas.ch.

Siddon, R.L., 1985. Fast calculation of the exact radiological path for a three-dimensional CT array. *Medical Physics*. 12(2), pp. 252–255.

Sinha, P., Khedr, A., McClincy, M.P., Kenkre, T.S., Novak, N.E. and Bosch, P., 2021. Epiphyseal translation as a predictor of avascular necrosis in unstable slipped capital femoral epiphysis. Journal of Pediatric Orthopaedics, 41(1), pp.40-45.

Snell, R.S., 2011. *Clinical Anatomy by Regions*. Lippincott Williams and Wilkins.

Southwick, W.O., 1967. Osteotomy through the lesser trochanter for slipped capital femoral epiphysis. *The Journal of Bone and Joint Surgery*. 49(5), pp. 807–835.

Southwick, W.O., 1973. Compression fixation after biplane intertrochanteric osteotomy for slipped capital femoral epiphysis. A technical improvement. *The Journal of bone and joint surgery. American volume*. 55(6), pp. 1218–1224.

Staub, D. and Murphy, M.J., 2013. A digitally reconstructed radiograph algorithm calculated from first principles. *Medical Physics*. 40(1), pp. 011902.

Stegmann, M.B., Fisker, R., ErsbØl, B.K., Thodberg, H.H. and Hyldstrup, L., 2000. Active appearance models: Theory and cases. *Proceedings of Danish Conference of Pattern Recognition and Image Analysis*. 49–57.

Steininger, P., Fritscher, K.D., Kofler, G., Schuler, B., Hänni, M., Schwieger, K. and Schubert, R. 2008. Comparison of different metrics for appearance-model-based 2D/3D-registration with x-ray images. In *Bildverarbeitung für die Medizin 2008*. (pp. 122–126). Springer, Berlin, Heidelberg

Styner, M.A., Rajamani, K.T., Nolte, L.P., Zsemlye, G., Székely, G., Taylor, C.J. and Davies, R.H., 2003. Evaluation of 3D correspondence methods for model building. *Information processing in medical imaging*. (pp. 63–75). Springer, Berlin, Heidelberg.

Taha, A.A. and Hanbury, A., 2015. Metrics for evaluating 3D medical image segmentation: analysis, selection, and tool. *BMC Medical Imaging*. 15(1), pp. 1-28.

Tariq, H. and Burney, S.A., 2012. Contour extraction of femur and tibia condyles on plain anteroposterior (AP) radiograph. *International Journal of Computer Applications*. 52(15), pp. 26–30.

Thusini, X.O., Reyneke, C.J., Aellen, J., Forster, A., Fouefack, J.R., Nbonsou Tegang, N.H., Vetter, T., Douglas, T.S. and Mutsvangwa, T.E., 2020. Uncertainty reduction in contour-based 3D/2D registration of bone surfaces. *International Workshop on Shape in Medical Imaging*. (pp. 18–29). Springer, Cham

Valera, M., Ibañez, N., Sancho, R. and Tey, M., 2016. Reliability of Tönnis classification in early hip arthritis: a useless reference for hip-preserving surgery. *Archives of Orthopaedic and Trauma Surgery*. 136(1), pp. 27–33.

van de Schoot, R., Depaoli, S., King, R., Kramer, B., Märtens, K., Tadesse, M.G., Vannucci, M., Gelman, A., et al., 2021. Bayesian statistics and modelling. *Nature reviews methods primers*. 1(1), pp. 1–26.

van der Merwe, J., 2018. Development of a patient-specific unicompartmental

knee replacement. (Doctoral dissertation, Stellenbosch: Stellenbosch University).

van der Merwe, J., van den Heever, D.J. and Erasmus, P.J., 2018. Estimating regions of interest on the distal femur. Medical Engineering and Physics, 60, pp.23-29.

Wagner, F. V., Negrão, J.R., Campos, J., Ward, S.R., Haghighi, P., Trudell, D.J. and Resnick, D., 2012. Capsular ligaments of the hip: anatomic, histologic, and positional study in cadaveric specimens with MR arthrography. *Radiology*. 263(1), pp. 189–198.

Wang, F., Davis, T.E. and Vemuri, B.C., 2002, September. Real-time DRR generation using cylindrical harmonics. In International Conference on Medical Image Computing and Computer-Assisted Intervention (pp. 671-678). Springer, Berlin, Heidelberg

Weiner, D., 1996. Pathogenesis of slipped capital femoral epiphysis. *Journal of Pediatric Orthopaedics Part B*. 5(2), pp. 67–73.

Xiao, K., Chen, D.Z., Hu, X.S. and Zhou, B. 2012. Efficient implementation of the 3D-DDA ray traversal algorithm on GPU and its application in radiation dose calculation. *Medical Physics*. 39(12), pp. 7619–7625.

Xu, Z., Baojie, X. and Guoxin, W., 2017. Canny edge detection based on Open CV. In IEEE *2017 13th IEEE International Conference on Electronic Measurement and Instruments (ICEMI)*. (pp. 53–56). IEEE.

Yao, J. and Taylor, R., 2003. Assessing accuracy factors in deformable 2D/3D medical image registration using a statistical pelvis model. In *Proceedings Proceedings Ninth IEEE International Conference on Computer Vision*. (pp. 1329–1334). IEEE

Yu, W., Chu, C., Tannast, M. and Zheng, G., 2016. Fully automatic reconstruction of personalized 3D volumes of the proximal femur from 2D x-ray images. *International Journal of Computer Assisted Radiology and Surgery*. 11(9), pp. 1673–1685.

Zheng, G., 2011. Personalized x-ray reconstruction of the proximal femur via a non-rigid 2D-3D registration. In *International Conference on Medical Image Computing and Computer-Assisted Intervention*. (pp. 598–606). Springer, Berlin, Heidelberg

Zheng, G., Gollmer, S., Schumann, S., Dong, X., Feilkas, T. and González Ballester, M.A., 2009. A 2D/3D correspondence building method for reconstruction of a patient-specific 3D bone surface model using point distribution models and calibrated X-ray images. *Medical Image Analysis*. 13(6), pp. 883–899.